



January 2017

Buckling Of Liquid-Filled Steel Storage Tanks Under Earthquake Loading

Wiriychai Roopkumdee

Follow this and additional works at: <https://commons.und.edu/theses>

Recommended Citation

Roopkumdee, Wiriychai, "Buckling Of Liquid-Filled Steel Storage Tanks Under Earthquake Loading" (2017). *Theses and Dissertations*. 2140.

<https://commons.und.edu/theses/2140>

This Thesis is brought to you for free and open access by the Theses, Dissertations, and Senior Projects at UND Scholarly Commons. It has been accepted for inclusion in Theses and Dissertations by an authorized administrator of UND Scholarly Commons. For more information, please contact zeinebyousif@library.und.edu.

BUCKLING OF LIQUID-FILLED STEEL STORAGE TANKS UNDER
EARTHQUAKE LOADING

by

Wiriyachai Roopkumdee

Bachelor of Engineering, King Mongkut's University of Technology Thonburi, 2010

Master of Arts, Western Kentucky University, 2014

A Thesis

Submitted to the Graduate Faculty

of the

University of North Dakota

In partial fulfillment of the requirements

for the degree of

Master of Science


Grand Forks, North Dakota

May


2017

Copyright 2017 Wiriyaichai Roopkumdee

This thesis, submitted by Wiriyachai Roopkumdee in partial fulfillment of the requirements for the Degree of Master of Science from the University of North Dakota, has been read by the Faculty Advisory Committee under whom the work has been done and is hereby approved.



Dr. Sukhvarsh Jerath (Chairperson)

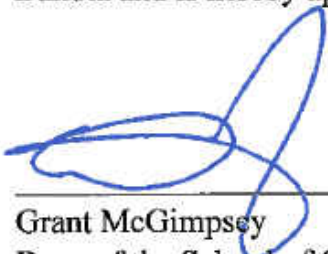


Dr. Iraj H.P. Mamaghani



Dr. Daba Gedafa

This thesis is being submitted by the appointed advisory committee as having met all of the requirements of the School of Graduate Studies at the University of North Dakota and is hereby approved.



Grant McGimpsey
Dean of the School of Graduate Studies

May 8, 2017

Date

PERMISSION

Title Buckling of Liquid-Filled Steel Storage Tanks under Earthquake Loading

Department Civil Engineering

Degree Master of Science

In presenting this thesis in partial fulfillment of the requirements for a graduate degree from the University of North Dakota, I agree that the library of this University shall make it freely available for inspection. I further agree that permission for extensive copying for scholarly purposes may be granted by the professor who supervised my thesis work or, in his absence, by the Chairperson of the department or the dean of the School of Graduate Studies. It is understood that any copying or publication or other use of this thesis or part thereof for financial gain shall not be allowed without my written permission. It is also understood that due recognition shall be given to me and to the University of North Dakota in any scholarly use which may be made of any material in my thesis.

Wiriyachai Roopkumdee

5/4/2017

TABLE OF CONTENT

LIST OF FIGURES	vii
LIST OF TABLES	xvii
ACKNOWLEDGEMENTS	xix
ABSTRACT	xx
CHAPTER	
I. INTRODUCTION	1
1.1 Introduction	1
1.2 Literature Review	2
II. REVIEW OF STRUCTURAL STABILITY	6
2.1 Definition of Buckling.....	6
2.2 Types of Stability	7
III. MODEL	10
3.1 Geometry and Material Description	10
3.2 Modeling in ANSYS	13
3.3 Verification of the Model	15
IV. STATIC BUCKLING ANALYSIS	18
4.1 Eigenvalue Buckling Analysis	18

4.2 Nonlinear Static Buckling Analysis	23
V. MODAL ANALYSIS	37
VI. TRANSIENT DYNAMIC ANALYSIS	52
6.1 Definition and Method	52
6.2 Rayleigh Damping.....	53
6.3 Earthquake Data	56
6.4 Results	57
6.4.1 Empty Cylindrical Tanks Subjected to the El Centro Earthquake	58
6.4.2 Cylindrical Tanks Filled with Water up to 90% of Height Subjected to the El Centro Earthquake	72
6.4.3 Empty Cylindrical Tanks Subjected to the Parkfield Earthquake	86
6.4.4 Cylindrical Tanks Filled with Water up to 90% of Height Subjected to the Parkfield Earthquake	100
6.4.5 Comparison of the Buckling Behaviors from El Centro and Parkfield Earthquakes for the Cylindrical Tanks Filled with Water up to 90% of the Heights	114
VII. CONCLUSIONS	115
REFERENCES	118

LIST OF FIGURES

Figure	Page
1. (a) Elephant foot buckling (b) diamond shape buckling.....	4
2. A ball curved surface	7
3. Post-buckling behavior for (a) stable symmetric bifurcation and (b) unstable symmetric bifurcation	8
4. Post-buckling behavior for (c) asymmetric bifurcation.....	9
5. The cylindrical tank dimensions	12
6. Shell 181	14
7. FLUID 80.....	15
8. Finite element model with shear load at the top	19
9. Lateral Eigenvalue Buckling Loads for Models with $D/t = 1000$	20
10. Lateral Eigenvalue Buckling Loads for Models with $D/t = 1500$	20
11. Lateral Eigenvalue Buckling Loads for Models with $D/t = 2000$	21
12. First buckling mode shape for Model 1	22
13. First buckling mode shape for Model 12	22
14. Load-Deflection curve of maximum deflection node for a half of Model 1	25
15. Post-buckling deflected shape of Model 1	25
16. Load-Deflection curve of maximum deflection node for a half of Model 2	26

17. Post-buckling deflected shape of Model 2.....	26
18. Load-Deflection curve of maximum deflection node for a half of Model 3	27
19. Post-buckling deflected shape of Model 3.....	27
20. Load-Deflection curve of maximum deflection node for a half of Model 4	28
21. Post-buckling deflected shape of Model 4.....	28
22. Load-Deflection curve of maximum deflection node for a half of Model 5	29
23. Post-buckling deflected shape of Model 5.....	29
24. Load-Deflection curve of maximum deflection node for a half of Model 6	30
25. Post-buckling deflected shape of Model 6.....	30
26. Load-Deflection curve of maximum deflection node for a half of Model 7	31
27. Post-buckling deflected shape of Model 7.....	31
28. Load-Deflection curve of maximum deflection node for a half of Model 8	32
29. Post-buckling deflected shape of Model 8.....	32
30. Load-Deflection curve of maximum deflection node for a half of Model 9	33
31. Post-buckling deflected shape of Model 9.....	33
32. Load-Deflection curve of maximum deflection node for a half of Model 10	34
33. Post-buckling deflected shape of Model 10.....	34
34. Load-Deflection curve of maximum deflection node for a half of Model 11	35

35. Post-buckling deflected shape of Model 11	35
36. Load-Deflection curve of maximum deflection node for a half of Model 12	36
37. Post-buckling deflected shape of Model.....	36
38. (a) First Shell Mode and (b) First Mode with 90% water depth of Model 1	40
39. (a) First Shell Mode and (b) First Mode with 90% water depth of Model 2	41
40. (a) First Shell Mode and (b) First Mode with 90% water depth of Model 3	42
41. (a) First Shell Mode and (b) First Mode with 90% water depth of Model 4	43
42. (a) First Shell Mode and (b) First Mode with 90% water depth of Model 5	44
43. (a) First Shell Mode and (b) First Mode with 90% water depth of Model 6	45
44. (a) First Shell Mode and (b) First Mode with 90% water depth of Model 7	46
45. (a) First Shell Mode and (b) First Mode with 90% water depth of Model 8	47
46. (a) First Shell Mode and (b) First Mode with 90% water depth of Model 9	48
47. (a) First Shell Mode and (b) First Mode with 90% water depth of Model 10	49
48. (a) First Shell Mode and (b) First Mode with 90% water depth of Model 11	50
49. (a) First Shell Mode and (b) First Mode with 90% water depth of Model 12	51
50. Accelerogram of North-South component of El Centro earthquake, 1940	56
51. Accelerogram of North-South component of Parkfield earthquake, 2004	57
52. Plots of dynamic buckling loads from transient analysis of empty tanks subjected to the El Centro earthquake, 1940.....	59

53. Pseudo equilibrium paths for the critical node of Model 1.....	60
54. Deformation shape of Model 1 for PGA = 55g	60
55. Pseudo equilibrium paths for the critical node of Model 2.....	61
56. Deformation shape of Model 2 for PGA = 33g	61
57. Pseudo equilibrium paths for the critical node of Model 3.....	62
58. Deformation shape of Model 3 for PGA = 24g	62
59. Pseudo equilibrium paths for the critical node of Model 4.....	63
60. Deformation shape of Model 4 for PGA = 38g	63
61. Pseudo equilibrium paths for the critical node of Model 5.....	64
62. Deformation shape of Model 5 for PGA = 25g	64
63. Pseudo equilibrium paths for the critical node of Model 6.....	65
64. Deformation shape of Model 6 for PGA = 17g	65
65. Pseudo equilibrium paths for the critical node of Model 7.....	66
66. Deformation shape of Model 7 for PGA = 33g	66
67. Pseudo equilibrium paths for the critical node of Model 8.....	67
68. Deformation shape of Model 8 for PGA = 20g	67
69. Pseudo equilibrium paths for the critical node of Model 9.....	68
70. Deformation shape of Model 9 for PGA = 15g	68

71. Pseudo equilibrium paths for the critical node of Model 10.....	69
72. Deformation shape of Model 10 for PGA = 30g	69
73. Pseudo equilibrium paths for the critical node of Model 11.....	70
74. Deformation shape of Model 11 for PGA = 18g	70
75. Pseudo equilibrium paths for the critical node of Model 12.....	71
76. Deformation shape of Model 12 for PGA = 12g	71
77. Plots of Nonlinear Transient Buckling Points of Tanks filled with water to 90% of their height subjected to the El Centro Earthquake, 1940	73
78. Pseudo equilibrium paths for the critical node of model 1 filled with water to 90% depth	74
79. (a) Undeformed shape and (b) Shell deformation of Model 1 filled with water to 90% depth	74
80. Pseudo equilibrium paths for the critical node of model 2 filled with water to 90% depth	75
81. (a) Undeformed shape and (b) Shell deformation of Model 2 filled with water to 90% depth	75
82. Pseudo equilibrium paths for the critical node of model 3 filled with water to 90% depth	76
83. (a) Undeformed shape and (b) Shell deformation of Model 3 filled with water to 90% depth	76
84. Pseudo equilibrium paths for the critical node of model 4 filled with water to 90% depth	77
85. (a) Undeformed shape and (b) Shell deformation of Model 4 filled with water to 90% depth	77

86. Pseudo equilibrium paths for the critical node of model 5 filled with water to 90% depth	78
87. (a) Undeformed shape and (b) Shell deformation of Model 5 filled with water to 90% depth	78
88. Pseudo equilibrium paths for the critical node of model 6 filled with water to 90% depth	79
89. (a) Undeformed shape and (b) Shell deformation of Model 6 filled with water to 90% depth	79
90. Pseudo equilibrium paths for the critical node of model 7 filled with water to 90% depth	80
91. (a) Undeformed shape and (b) Shell deformation of Model 7 filled with water to 90% depth	80
92. Pseudo equilibrium paths for the critical node of model 8 filled with water to 90% depth	81
93. (a) Undeformed shape and (b) Shell deformation of Model 8 filled with water to 90% depth	81
94. Pseudo equilibrium paths for the critical node of model 9 filled with water to 90% depth	82
95. (a) Undeformed shape and (b) Shell deformation of Model 9 filled with water to 90% depth	82
96. Pseudo equilibrium paths for the critical node of model 10 filled with water to 90% depth	83
97. (a) Undeformed shape and (b) Shell deformation of Model 10 filled with water to 90% depth	83
98. Pseudo equilibrium paths for the critical node of model 11 filled with water to 90% depth	84
99. (a) Undeformed shape and (b) Shell deformation of Model 11 filled with water to 90% depth	84

101. Pseudo equilibrium paths for the critical node of model 12 filled with water to 90% depth.....	85
101.(a) Undeformed shape and (b) Shell deformation of Model 12 filled with water to 90% depth	85
102. Plots of Dynamic Buckling Points of Empty Tanks subjected to the Parkfield Earthquake, 2004.....	87
103. Pseudo equilibrium paths for the critical node of Model 1.....	88
104. Deformation shape of Model 1 for PGA = 78g	88
105. Pseudo equilibrium paths for the critical node of Model 2.....	89
106. Deformation shape of Model 1 for PGA = 57g	89
107. Pseudo equilibrium paths for the critical node of Model 3.....	90
108. Deformation shape of Model 3 for PGA = 30g	90
109. Pseudo equilibrium paths for the critical node of Model 4.....	91
110. Deformation shape of Model 4 for PGA = 57g	91
111. Pseudo equilibrium paths for the critical node of Model 5.....	92
112. Deformation shape of Model 5 for PGA = 45g	92
113. Pseudo equilibrium paths for the critical node of Model 6.....	93
114. Deformation shape of Model 6 for PGA = 25g	93
115. Pseudo equilibrium paths for the critical node of Model 7.....	94
116. Deformation shape of Model 7 for PGA = 55g	94

117. Pseudo equilibrium paths for the critical node of Model 8.....	95
118. Deformation shape of Model 8 for PGA = 45g	95
119. Pseudo equilibrium paths for the critical node of Model 9.....	96
120. Deformation shape of Model 9 for PGA = 25g	96
121. Pseudo equilibrium paths for the critical node of Model 10.....	97
122. Deformation shape of Model 10 for PGA = 50g	97
123. Pseudo equilibrium paths for the critical node of Model 11	98
124. Deformation shape of Model 11 for PGA = 35g.....	98
125. Pseudo equilibrium paths for the critical node of Model 12.....	99
126. Deformation shape of Model 12 for PGA = 27g.....	99
127. Plots of Dynamic Buckling Points of Tanks filled with water to 90% depth subjected to the Parkfield earthquake, 2004.....	101
128. Pseudo equilibrium paths for the critical node of model 1 filled with water to 90% depth.....	102
129. (a) Undeformed shape and (b) Shell deformation of Model 1 filled with water to 90% depth.....	102
130. Pseudo equilibrium paths for the critical node of model 2 filled with water to 90% depth.....	103
131. (a) Undeformed shape and (b) Shell deformation of Model 2 filled with water to 90% depth.....	103
132. Pseudo equilibrium paths for the critical node of model 3 filled with water to 90% depth.....	104

133. (a) Undeformed shape and (b) Shell deformation of Model 3 filled with water to 90% depth	104
134. Pseudo equilibrium paths for the critical node of model 4 filled with water to 90% depth.....	105
135. (a) Undeformed shape and (b) Shell deformation of Model 4 filled with water to 90% depth.....	105
136. Pseudo equilibrium paths for the critical node of model 5 filled with water to 90% depth.....	106
137. (a) Undeformed shape and (b) Shell deformation of Model 5 filled with water to 90% depth.....	106
138. Pseudo equilibrium paths for the critical node of model 6 filled with water to 90% depth.....	107
139. (a) Undeformed shape and (b) Shell deformation of Model 6 filled with water to 90% depth	107
140. Pseudo equilibrium paths for the critical node of model 7 filled with water to 90% depth.....	108
141. (a) Undeformed shape and (b) Shell deformation of Model 7 filled with water to 90% depth.....	108
142. Pseudo equilibrium paths for the critical node of model 8 filled with water to 90% depth.....	109
143. (a) Undeformed shape and (b) Shell deformation of Model 8 filled with water to 90% depth.....	109
144. Pseudo equilibrium paths for the critical node of model 9 filled with water to 90% depth	110
145. (a) Undeformed shape and (b) Shell deformation of Model 9 filled with water to 90% depth.....	110

146. Pseudo equilibrium paths for the critical node of model 10 filled with water to 90% depth.....	111
147. (a) Undeformed shape and (b) Shell deformation of Model 10 filled with water to 90% depth.....	111
148. Pseudo equilibrium paths for the critical node of model 11 filled with water to 90% depth.....	112
149. (a) Undeformed shape and (b) Shell deformation of Model 11 filled with water to 90% depth.....	112
150. Pseudo equilibrium paths for the critical node of model 12 filled with water to 90% depth.....	113
151. (a) Undeformed shape and (b) Shell deformation of Model 12 filled with water to 90% depth.....	113

LIST OF TABLES

Table	Page
1. Summary of twelve different geometries of the cylindrical tanks.....	13
2. Comparison of FEA axial buckling loads with the theoretical buckling stress for the pin-pin ended cylindrical shells	16
3. Eigenvalue buckling for lateral loading.....	19
4. Summary results of eigenvalue and nonlinear buckling of lateral shear loads....	24
5. First natural frequencies.....	39
6. Natural Frequencies of Model 1	40
7. Natural Frequencies of Model 2	41
8. Natural Frequencies of Model 3	42
9. Natural Frequencies of Model 4	43
10. Natural Frequencies of Model 5	44
11. Natural Frequencies of Model 6	45
12. Natural Frequencies of Model 7	46
13. Natural Frequencies of Model 8	47

14. Natural Frequencies of Model 9	48
15. Natural Frequencies of Model 10	49
16. Natural Frequencies of Model 11	50
17. Natural Frequencies of Model 12	51
18. Mass and stiffness coefficients for the empty tanks models.....	55
19. Mass and stiffness coefficients for the 90% liquid filled tanks models.....	55
20. Dynamic Buckling Points of Empty Tanks subjected to the El Centro Earthquake, 1940.....	58
21. Dynamic buckling points of tanks filled with water to 90% of their height subjected to the El Centro earthquake, 1940	73
22. Dynamic Buckling Points of Empty Tanks subjected to the Parkfield earthquake	86
23. Dynamic Buckling Points of Tanks filled with water to 90% depth subjected to the Parkfield earthquake, 2004	100
24. Dynamic buckling loads for the cylindrical tanks filled with water up to 90% of the heights in PGA (g)	114

ACKNOWLEDGEMENTS

I wish to express my sincere appreciation and gratitude to Dr. Sukhvarsh Jerath, my advisor and the chair of Civil Engineering Department, for his guidance and support throughout my graduate academic career. My sincere thanks also extended to my committee members, Dr. Iraj Mamaghani and Dr. Daba Gedafa, for their valuable support and advice to complete this thesis.

ABSTRACT

The static and dynamic buckling loads of cylindrical liquid storage tanks were studied in this thesis. Finite element analysis was performed using ANSYS computer program. Twelve different geometries of the cylindrical tanks were analyzed with height to diameter (H/D) ratios of 0.5, 1.0, 1.5, and 2.0 and the diameter to thickness (D/t) ratios of 1000, 1500, and 2000 to cover tall and short cylindrical tanks. The transient dynamic analysis was performed to find the dynamic buckling loads. Applied dynamic loads in this study are horizontal earthquake excitations in terms of acceleration (g) due to gravity. Budiansky and Roth procedure was used to find the dynamic buckling load for both empty and tanks filled with water up to 90% of their height. Analysis results show that the dynamic buckling loads in terms of peak ground accelerations (PGA) are very high which are unrealistic for any recorded earthquake. For the cylindrical tanks filled with water up to 90% of their height; on the other hand, the dynamics buckling loads are small, and these dynamic loads are less than some recorded real world earthquakes. The H/D and D/t ratios have the important roles in the design of earthquake stability for the cylindrical liquid storage tanks. Results from the transient dynamic analysis represent that the dynamic buckling loads decrease when the H/D ratios increase, and the dynamic buckling loads decrease when the D/t ratios increase. Furthermore, with different characteristics of the earthquakes, the dynamic buckling behaviors of the cylindrical tank are dissimilar. Design curves for the cylindrical tanks of various geometries subjected to different earthquakes were generated in this thesis.

CHAPTER I

INTRODUCTION

1.1 Introduction

Liquid storage tanks are subjected to the horizontal and vertical ground accelerations during the earthquakes. These earthquake ground accelerations may cause damages to the liquid storage tanks. Spillage of toxic liquid from the liquid storage tanks could cause a serious threat to human health and the environment. Additionally, failure of tanks which contain an inflammable substance such as petroleum has frequently led to an uncontrolled fire which occurred during Niigata and Alaska earthquakes in 1964 [1].

The damages of petroleum storage tanks were reported due to earthquakes of 1933 Long Beach, 1952 Kern County, 1964 Alaska, 1971 San Fernando, 1979 Imperial Valley, 1983 Coalinga, 1989 Loma Prieta, 1992 Landers, 1994 Northridge, and 1995 Kobe [2]. Damages of cylindrical tanks due to earthquake loading can occur in several forms. The American Lifelines Alliance (ALA) [3] reported the failure modes that have occurred to steel storage tanks. These failure modes are shell buckling mode, roof and miscellaneous steel damage, anchorage failure, tank support system failure, foundation failure, hydrodynamic pressure failure, connecting pipe failure, and manhole failure. This study is interested in the shell buckling mode subjected to the horizontal earthquake accelerations.

The dynamic buckling analyses of liquid storage tanks subjected to different earthquake loads were analyzed using Finite Element Analysis (FEA). ANSYS workbench computer program was used for all FEA computations. There are twelve different geometries of the cylindrical liquid storage tanks with height to diameter (H/D) ratios of 0.5, 1.0, 1.5, and 2.0 and diameter to thickness (D/t) ratios of 1000, 1500, and 2000. These liquid storage tanks are subjected to two different earthquakes which are El Centro (1940) and Parkfield (2004). These earthquakes were chosen because they have different characteristics. Primarily, the theory of shell structure buckling, verification of FEA models, and static buckling analysis were discussed and investigated before the nonlinear dynamic buckling analyses of liquid storage tanks were intensely analyzed.

Chapter 2 presents the theory and definition of buckling. Chapter 3 introduces FEA models, material properties, and model verification. Chapter 4 presents static buckling analysis to find the eigenvalue buckling load and nonlinear static buckling of each FEA model. Chapter 5 presents natural frequencies, mode shapes, analysis of each FEA model. Chapter 6 presents dynamic buckling from the transient buckling analysis. Chapter 7 discusses and concludes the results that were found in this study.

1.2 Literature Review

Failures of liquid cylindrical storage tanks have become more susceptible to the buckling because of the improvement of high strength materials. A lot of research has been conducted to investigate the buckling behavior of cylindrical tanks for both empty and liquid filled tanks. However, based on previous research, there is no practical design curve for the buckling loads of tanks of various sizes and thicknesses subjected to different earthquakes.

In the early years of shell buckling theory, Timoshenko [4] presented the symmetrical buckling of a cylindrical shell under uniform axial compressive pressure by using the energy method. The energy of axial compression is equal to the total strain energy if the shell remains cylindrical. An increase of energy is equal to the work done by the critical compressive load when the cylindrical shell is shortened due to buckling. Brazier [5] studied the instability of a thin cylindrical shell in bending. By comparing to the theory of curved bars, Brazier presented that the thin curved tubes are more flexible in bending than the curved bars. The circular cross-section becomes more even oval during bending until the load that makes the bending resistance starts to decrease is reached.

After that, many research was done in the area of dynamic loading of liquid-filled cylindrical tanks. Housner [6] reported that the hydrodynamic behavior between water and the storage tanks which are subjected to horizontal accelerations can be distinguished into two kinds. First, impulsive mass, a mass of water is rigidly attached to the tank at the proper height. Second, convective mass, the horizontal accelerations from the tank excites a mass of water into oscillations. Veletsos and Auyang [7] reported that cylindrical tanks containing liquid have a cantilever beam mode when the tanks are subjected to horizontal excitation. Malhotra [8] presented that the design of fixed-based cylindrical tank is a simple and efficient way to design for the convective component, compulsive component, and shell deformation due to interaction effects from the impulsive component. The buckling behavior of steel tanks subjected to seismic excitation from experiments and computations can be classified as elasto-plastic buckling and elastic buckling. The elephant foot buckling, an outward bulge above the base of the tank, usually occurs with the elasto-plastic buckling, and diamond shape buckling is

associated with elastic buckling [9]. Figure 1 illustrates the failures of cylindrical tanks due to elephant foot and diamond shape buckling which located above the supports.

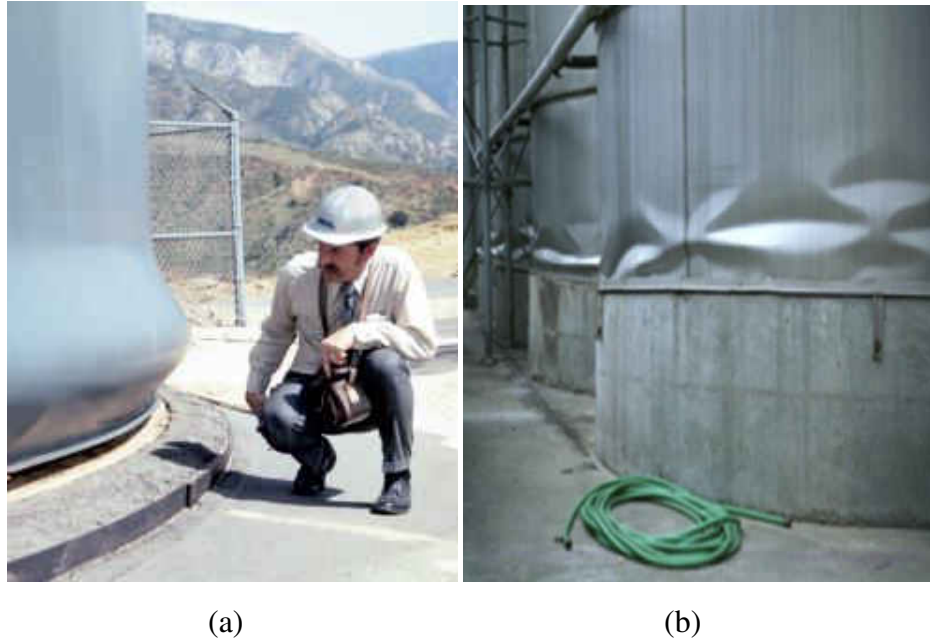


Figure 1. (a) Elephant foot buckling (b) diamond shape buckling (courtesy of University of California at Berkeley)

Sezen et al. [9] used ANSYS computer program to study liquefied gas-structure interaction and a simplified model of three tanks in Turkey that experienced an earthquake on August 17, 1999, and they reported that shear and bending moments are overestimated if the fluid is modeled as a single rigid mass. In terms of inertia force, the inertia forces of the shell for steel tanks can be neglected because the mass of the shell is small compared to the hydrodynamic forces [10]. However, according to Hamdan [11], the neglect of the inertia forces of the shell for steel tanks is not always correct. The inertia forces due to the tanks may be necessary to be included if a roof of the tank accounts for the snow loading [12]. Virella et al. [13] presented the critical value of peak ground acceleration (PGA) for conical roof tanks subject to horizontal acceleration. The critical values of PGA for cylindrical tanks filled with liquid up to 90% of the height of

the tanks were found to be between 0.25g and 0.35g using ABAQUS finite element software ($1g = 32.17405 \text{ ft/s}^2 = 9.807 \text{ m/s}^2$).

Jerath and Qiao [14] presented that the critical PGA of cylindrical steel tanks increases with increase in natural frequencies, and they also found that the cylindrical steel tank is unstable due to resonance when the frequency of dynamic loading is equal to the structure natural frequency. Jerath and Lee [15] present the buckling load from nonlinear transient analysis of cylindrical water storage tanks using ANSYS computer program. For the empty cylindrical tanks, their results agree with the study of Qiao and Jerath as discussed above. They found that a decrease of height to diameter ratio (H/D) has a significant improvement for earthquake stability design of over ground cylindrical steel tanks.

CHAPTER II

REVIEW OF STRUCTURAL STABILITY

2.1 Definition of Buckling

Buckling occurs when a structure is under compressive loading, and this loading leads to change in geometry due to instability. To resist the loading, the structure finds new equilibrium configuration. According to Chen and Lui [16], for the structural design, there are two types of limit states. The first type is strength limit states which considers the maximum load capacity of the structure or structural member. The second type is serviceability limit states which are concerned with serviceability performance of the structure under normal service conditions. Large deformation of the structure or structure member may occur when the loading is under the maximum load capacity due to the instability. The nature of structural stability can be grouped into three situations: stable equilibrium, unstable equilibrium, and neutral equilibrium. The concept of the structural stability can be well explained by using the illustration of a ball on a curved surface. In the case of the stable equilibrium, with a slight disturbing force, the ball on a concave surface will slightly displace and return to the initial position if the ball is no longer being disturbed. For the unstable equilibrium, if the disturbing force is applied to the ball on a convex surface, the ball will be displaced and will never return to the initial position even if there is no longer load distribution. For the neutral equilibrium, if the distributing

force is applied to the ball on a flat surface, the ball will displace to another location to find a new equilibrium position. The ball will remain at the new equilibrium position even if there is no longer load distribution. The examples of the ball on a curved surface are illustrated in Figure 2.

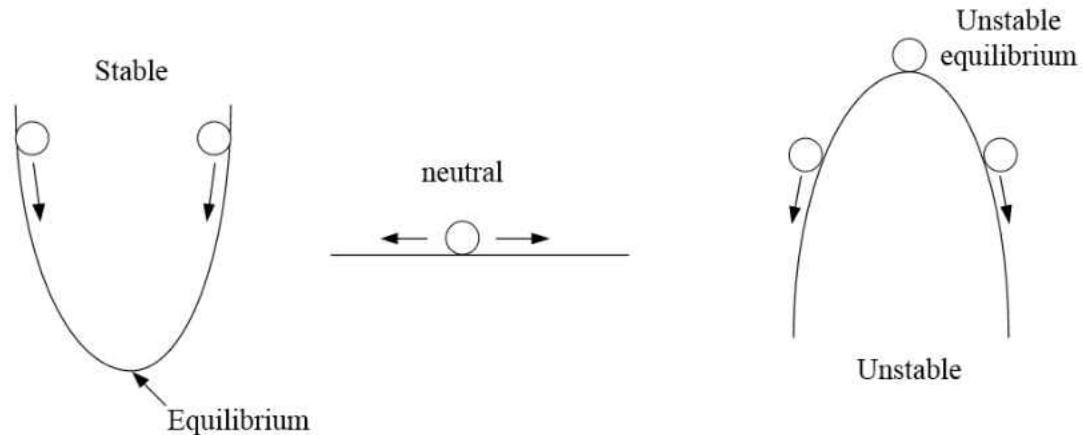


Figure 2. A ball curved surface [16]

2.2 Types of Stability

The stability of a structure can be classified into two categories which are bifurcation instability and limit-load instability [16]. For the bifurcation instability, as the compressive load increases, the structure or structural member deforms in the direction of applied load then suddenly deflects in a different normal direction from the applied load. The point of this deflection is called the point of bifurcation, and the load at the point of bifurcation is called the critical load. The primary or fundamental path is the deflection path before the structures or structural members reach the point of bifurcation. The secondary or post-buckling path is the deflection path that exists after the structures or structural members reach the point of bifurcation. There are two types of bifurcations,

symmetric bifurcation and asymmetric bifurcation depending on the post-buckling behavior.

In the case of symmetric bifurcation, the post-buckling paths are symmetrical about the load axis. The post-buckling paths rise above the critical load for the stable symmetric bifurcation. On the other hand, the post-buckling paths drop below the critical load for the unstable symmetric bifurcation as shown in Figure 3.

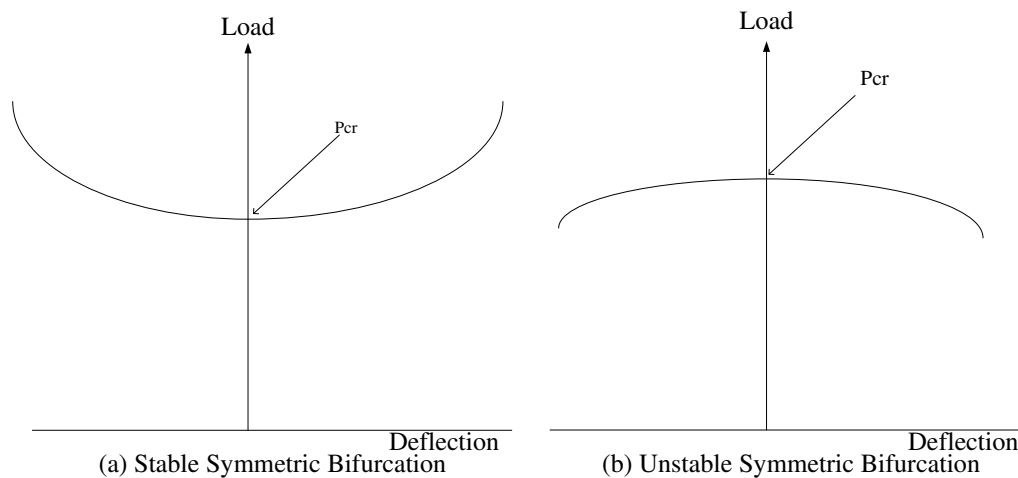


Figure 3. Post-buckling behavior for (a) stable symmetric bifurcation and (b) unstable symmetric bifurcation [16]

In the case of asymmetric bifurcation, the load which maintains the equilibrium to buckling load may increase or decrease depending on the direction that the structure deflects after the buckling as shown in Figure 4.

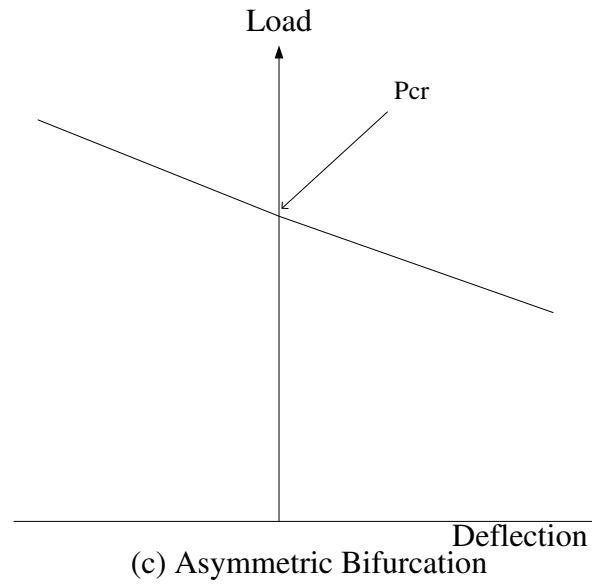


Figure 4. Post-buckling behavior for (c) asymmetric bifurcation [16]

CHAPTER III

MODEL

3.1 Geometry and Material Description

Twelve different geometries of the tanks are analyzed with height to diameter (H/D) ratios of 0.5, 1.0, 1.5, and 2.0 and the diameter to thickness (D/t) ratios of 1000, 1500, and 2000 to investigate the buckling behavior of various sizes of the cylindrical tanks. These twelve cylindrical tanks are modeled as above ground storage tanks (AST) that are open at the top. The cylindrical tanks are considered fixed at the bottom and free on the top as shown in Figure 5.

- Model 1: The geometric parameters are height, $H = 180$ in. (4.572 m), diameter, $D = 360$ in. (9.144 m.), and thickness = 0.36 in. (9.144 mm), ($H/D = 0.5$ and $D/t = 1000$).
- Model 2: The geometric parameters are height, $H = 180$ in. (4.572 m), diameter, $D = 360$ in. (9.144 m), and thickness = 0.24 in. (6.096 mm), ($H/D = 0.5$ and $D/t = 1500$).
- Model 3: The geometric parameters are height, $H = 180$ in. (4.572 m), diameter, $D = 360$ in. (9.144 m), and thickness = 0.18 in. (4.572 mm), ($H/D = 0.5$ and $D/t = 2000$)

- Model 4: The geometric parameters are height, $H = 360$ in. (9.144 m), diameter, $D = 360$ in. (9.144 m), and thickness = 0.36 in. (9.144 mm), ($H/D = 1.0$ and $D/t = 1000$).
- Model 5: The geometric parameters are height, $H = 360$ in. (9.144 m), diameter, $D = 360$ in. (9.144 m), and thickness = 0.24 in. (6.096 mm), ($H/D = 1.0$ and $D/t = 1500$).
- Model 6: The geometric parameters are height, $H = 360$ in. (9.144 m), diameter, $D = 360$ in. (9.144 m), and thickness = 0.18 in. (4.572 mm), ($H/D = 1.0$ and $D/t = 2000$).
- Model 7: The geometric parameters are height, $H = 540$ in. (13.716 m), diameter, $D = 360$ in. (9.144 m), and thickness = 0.36 in. (9.144 mm), ($H/D = 1.5$ and $D/t = 1000$).
- Model 8: The geometric parameters are height, $H = 540$ in. (13.716 m), diameter, $D = 360$ in. (9.144 m), and thickness = 0.24 in. (6.096 mm), ($H/D = 1.5$ and $D/t = 1500$).
- Model 9: The geometric parameters are height, $H = 540$ in. (13.716 m), diameter, $D = 360$ in. (9.144 m), and thickness = 0.18 in. (4.572 mm), ($H/D = 1.5$ and $D/t = 2000$).
- Model 10: The geometric parameters are height, $H = 720$ in. (18.288 m), diameter, $D = 360$ in. (9.144 m), and thickness = 0.36 in. (9.144 mm), ($H/D = 2.0$ and $D/t = 1000$).

- Model 11: The geometric parameters are height, $H = 720$ in. (18.288 m), diameter, $D = 360$ in. (9.144 m), and thickness = 0.24 in. (6.096 mm), ($H/D = 2.0$ and $D/t = 1500$).
- Model 12: The geometric parameters are height, $H = 720$ in. (18.288 m), diameter, $D = 360$ in. (9.144 m), and thickness = 0.18 in. (4.572 mm), ($H/D = 2.0$ and $D/t = 2000$).

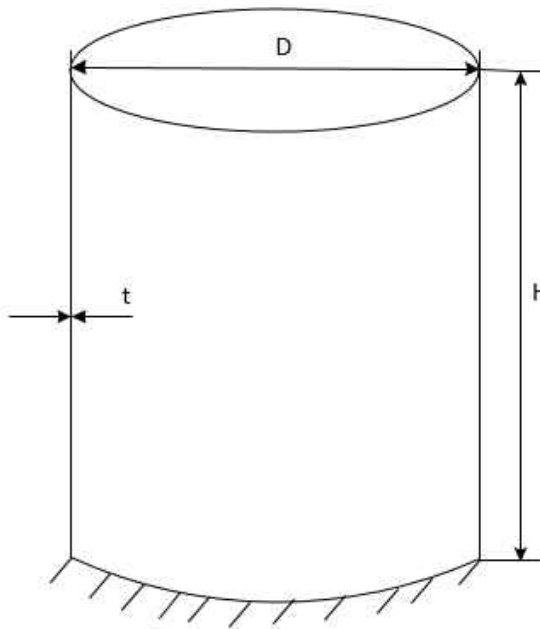


Figure 5. The cylindrical tank dimension

Summary of twelve different geometries of the cylindrical tanks adopted in this study is listed in Table 1.

Table 1. Summary of twelve different geometries of the cylindrical tanks

Model	H	D	t	H/D	D/t
1	180 in. (4.573 m)	360 in. (9.144 m)	0.360 in. (9.144 mm)	0.5	1,000
2	180 in. (4.573 m)	360 in. (9.144 m)	0.240 in. (6.096 mm)	0.5	1,500
3	180 in. (4.573 m)	360 in. (9.144 m)	0.180 in. (4.572 mm)	0.5	2,000
4	360 in. (9.144 m)	360 in. (9.144 m)	0.360 in. (9.144 mm)	1.0	1,000
5	360 in. (9.144 m)	360 in. (9.144 m)	0.240 in. (6.096 mm)	1.0	1,500
6	360 in. (9.144 m)	360 in. (9.144 m)	0.180 in. (4.572 mm)	1.0	2,000
7	540 in. (13.716 m)	360 in. (9.144 m)	0.360 in. (9.144 mm)	1.5	1,000
8	540 in. (13.716 m)	360 in. (9.144 m)	0.240 in. (6.096 mm)	1.5	1,500
9	540 in. (13.716 m)	360 in. (9.144 m)	0.180 in. (4.572 mm)	1.5	2,000
10	720 in. (18.288 m)	360 in. (9.144 m)	0.360 in. (9.144 mm)	2.0	1,000
11	720 in. (18.288 m)	360 in. (9.144 m)	0.240 in. (6.096 mm)	2.0	1,500
12	720 in. (18.288 m)	360 in. (9.144 m)	0.180 in. (4.572 mm)	2.0	2,000

The material for all cylindrical storage tanks is steel with a modulus of elasticity, $E = 29(10^6)$ psi (200,000 MPa), Poisson's ratio, $\nu = 0.3$, and the mass density, $\rho = 15.232$ slugs/ft³ (7,850 kg/m³). Bilinear isotropic hardening of the steel is included with the yield stress of 50,000 psi (344.74 MPa) and the tangent modulus of 2,000 ksi (13,790 MPa). The liquid filled inside the cylindrical tanks is water with the bulk modulus of 300,000 psi (2,068.4 MPa), and the mass density of 1.9403 slugs/ft³ (1,000 kg/m³).

3.2 Modeling in ANSYS

The finite element analysis (FEA) computer program, ANSYS, is used to carry all computations. Due to the symmetric geometries, all FEA models were modeled with only half of cylinder to reduce the computation time. From the element types in ANSYS, SHELL181 element was used to be the element for the steel cylindrical tanks. FLUID80 element was used to be the element for water filled inside the cylindrical tanks.

According to ANSYS, Inc. [17], SHELL181 is a four-node element with six degrees of freedom at each node (translation in x, y, and z directions, and rotation about x, y, and z axes). SHELL181 element is suitable for linear, large rotation, and large strain nonlinear applications. In term of elasticity, SHELL181 can be associated with linear elastic, elastoplastic, creep, or hyper-elastic material properties. Only isotropic, anisotropic, and orthotropic linear elastic properties can be input for elasticity. Node locations and element coordinate system of SHELL181 are illustrated in Figure 6.

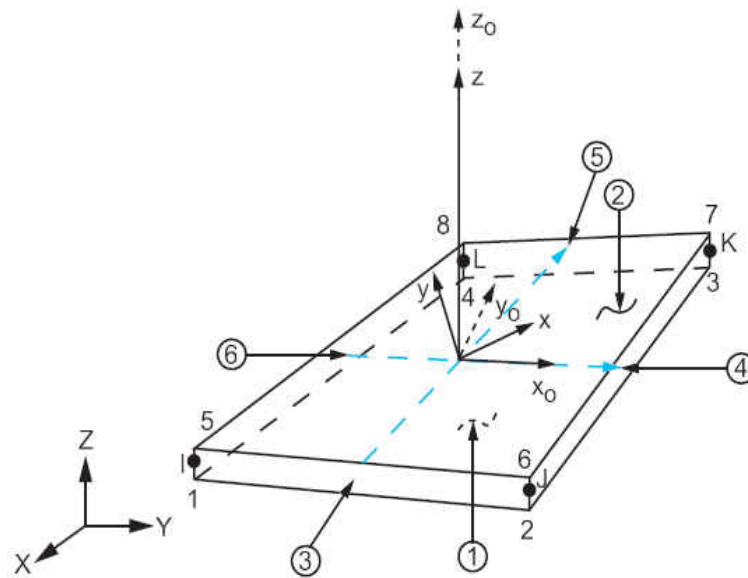


Figure 6. Shell 181 [18]

According to ANSYS, Inc., [18], FLUID80 is used to model fluids contained within the vessel which have no net flow rate. FLUID80 is an eight-node element with three degrees of freedom at each node (translation in x, y, and z directions). The fluid element is particularly well suited for calculating hydrostatic pressure and fluid/solid interaction. Additionally, acceleration effects and temperature effects can be included. The fluid element at a boundary should not be attached directly to structural elements but should have separate, coincident nodes that are coupled only in the direction normal to

the interface [18]. Node locations and element coordinate system of FLUID80 are illustrated in Figure 7.

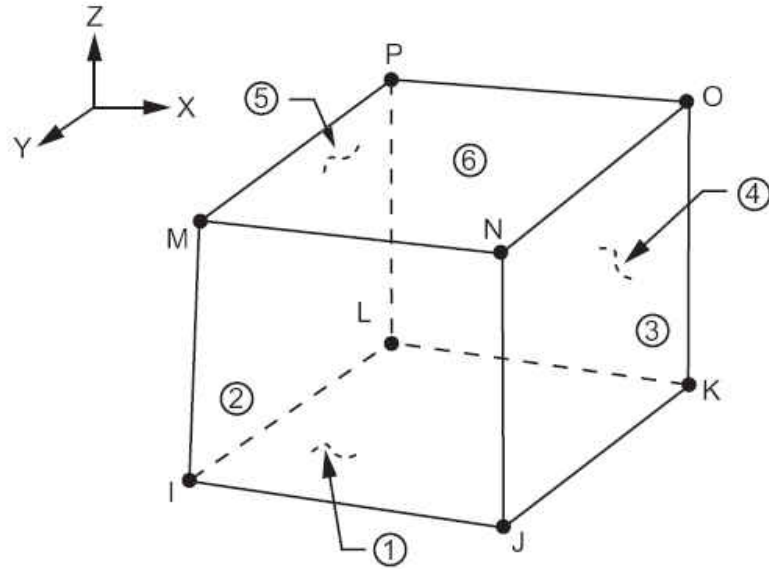


Figure 7. FLUID 80 [18]

3.3 Verification of the Model

The accuracy of finite element model using ANSYS computer program is verified by using the theoretical buckling stress for the pin-pin ended cylindrical shells. The axial compressive load is applied at the top of the cylindrical tank. Eigenvalue buckling load (linear buckling load) for each model was calculated by eigenvalue analysis from ANSYS computer program to compare with the theoretical critical stress (σ_{cr}) for static axial buckling for the pin-pin ended cylindrical shells. The theoretical static buckling stress for the pin-pin ended cylindrical shells using English unit is given by [4]:

$$\sigma_{cr} = \frac{E}{\sqrt{3(1-\nu^2)}} \left(\frac{t}{R} \right) \quad (1)$$

Where: R is the radius of the cylindrical shell.
 E is the modulus of elasticity.
 t is the thickness of the cylindrical shell.
 v is the Poisson's ratio of the steel.

For FEA buckling stress, the compressive pressure line of 1 N/mm was applied at the top to be a unit load in ANSYS. Thus, from ANSYS, the compressive pressure line of 1 N/mm multiplied by the multiplier is the values of the critical uniform distributed load from finite element analysis. Table 2 present the summary of model verification.

Table 2. Comparison of FEA axial buckling stresses with the theoretical buckling stresses for the pin-pin ended cylindrical shells

Model	Multiplier (N/mm)	t (mm)	Buckling Stress (MPa)		% error
			Theoretical	FEA	
1	2,423	9.144	242.03	264.98	9.48
2	1,078	6.096	161.37	176.84	9.58
3	604	4.572	121.02	132.11	9.16
4	2,427	9.144	242.02	265.42	9.67
5	1,079	6.096	161.35	177.00	9.70
6	605	4.572	121.02	132.33	9.34
7	2,280	9.144	242.03	249.34	3.02
8	1,061	6.096	161.35	174.05	7.87
9	605	4.572	121.03	132.33	9.33
10	2,270	9.144	242.03	248.25	2.57
11	1,050	6.096	161.35	172.24	6.75
12	605	4.572	121.03	132.33	9.33

Since the applied load is the compressive pressure of 1 lb/in, the unit of the multiplier is also lb/in. The buckling stress from FEA can be calculated as equation (2).

$$\sigma_{cr(FEA)} = \frac{\text{Multiplier}}{t} \quad (2)$$

For example, in the case of model 1, the theoretical critical stress (σ_{cr}):

$$\sigma_{cr} = \frac{29,000,000 \text{ psi}}{\sqrt{3(1-0.3^2)}} \left(\frac{0.36 \text{ in.}}{180 \text{ in.}} \right) = 35,103 \text{ psi} = 242.03 \text{ MPa}$$

And, the buckling stress from FEA:

$$\sigma_{cr(FEA)} = \frac{2,423 \text{ N/mm}}{9.144 \text{ mm}} = 264.98 \text{ MPa}$$

The error is $\frac{264.98 - 242.03}{242.03} \times 100 \% = 9.48\%$

The errors of the models are between 2.57% to 9.70%. These results show that the FEA models are quite adequate in predicting static critical load.

CHAPTER IV

STATIC BUCKLING ANALYSIS

4.1 Eigenvalue Buckling Analysis

Eigenvalue or linear buckling load analysis was performed to study the bifurcation point of the ideal linear elastic structure. The results from eigenvalue buckling are overestimated because nonlinearity due to large deflection, contact, and imperfections are neglected. However, the eigenvalue buckling load can be used to obtain the upper limit for nonlinear analysis and determine the possible buckling mode shapes. The eigenvalue problem is solved to get the buckling load multiplier (λ_i) and buckling modes (ψ_i) as shown in equation (3) [19].

$$([K] + \lambda_i[S])\{\psi_i\} = 0 \quad (3)$$

Where: [K] is the stiffness matrix
[S] is the stress stiffness matrix

For the eigenvalue buckling analysis, the linear elastic behavior is assumed for the material. In this study, the unit force was applied at the top of the half cylindrical tank in the Y direction of the Cartesian coordinate system which is normal to the cylinder longitudinal axis as shown in Figure 8. The multiplier for lateral linear buckling load is obtained as the result after the simulation is completed. Since the multiplier is the total

load for half of the cylindrical tanks, the eigenvalue buckling load is equal to the multiplier multiplies by two. Table 3 represents the eigenvalue buckling load of the analyzed twelve cylindrical tanks.

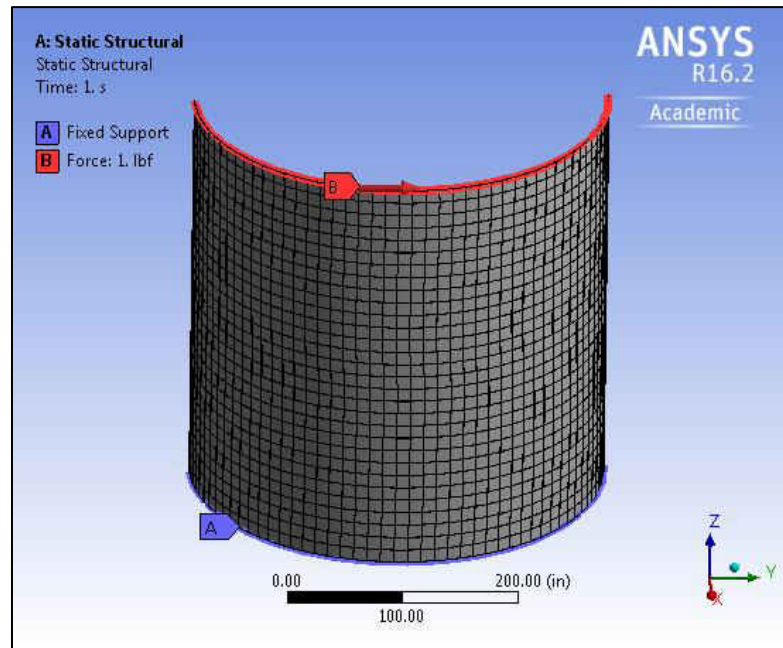


Figure 8. Finite element model with shear load at the top

Table 3. Eigenvalue buckling loads

Model	H/D	D/t	Multiplier (N)	Eigenvalue Buckling Load (N)
1	0.5	1,000	333,830	667,660
2	0.5	1,500	122,388	244,777
3	0.5	2,000	60,398	120,796
4	1.0	1,000	318,235	636,469
5	1.0	1,500	116,183	232,366
6	1.0	2,000	57,084	114,168
7	1.5	1,000	314,734	629,468
8	1.5	1,500	114,608	229,217
9	1.5	2,000	56,230	112,460
10	2.0	1,000	313,439	626,879
11	2.0	1,500	114,052	228,105
12	2.0	2,000	55,776	111,553

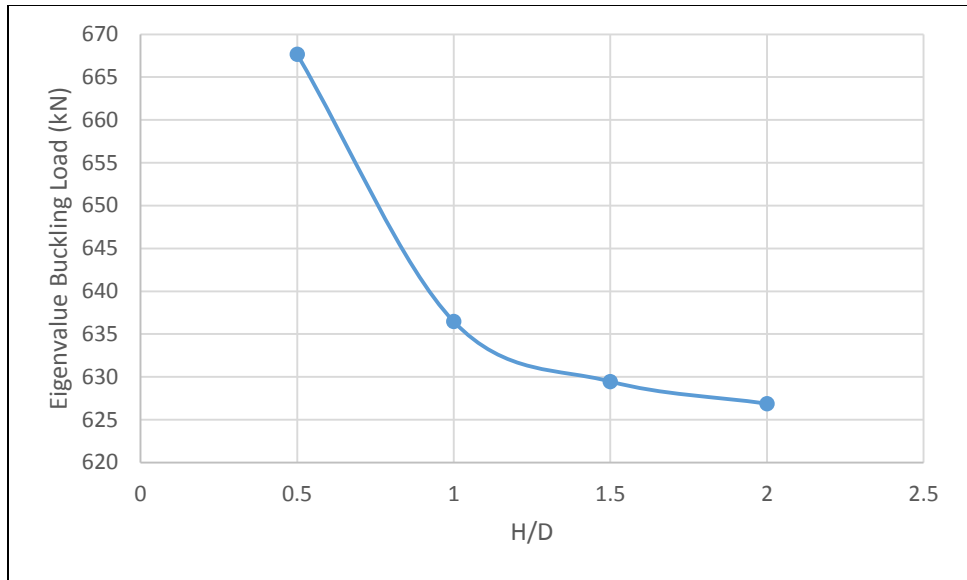


Figure 9. Lateral Eigenvalue Buckling Loads for Models with $D/t = 1,000$

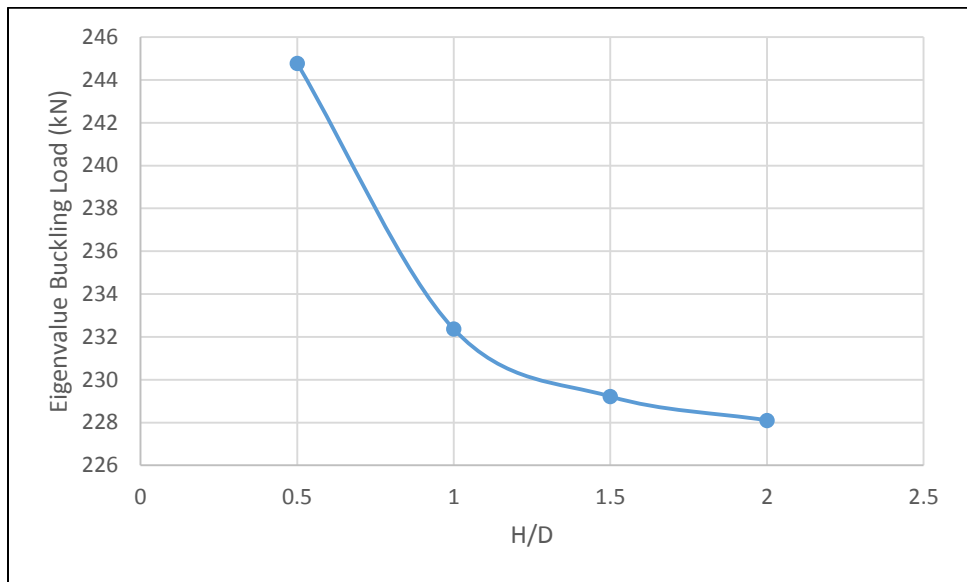


Figure 10. Lateral Eigenvalue Buckling Loads for Models with $D/t = 1,500$

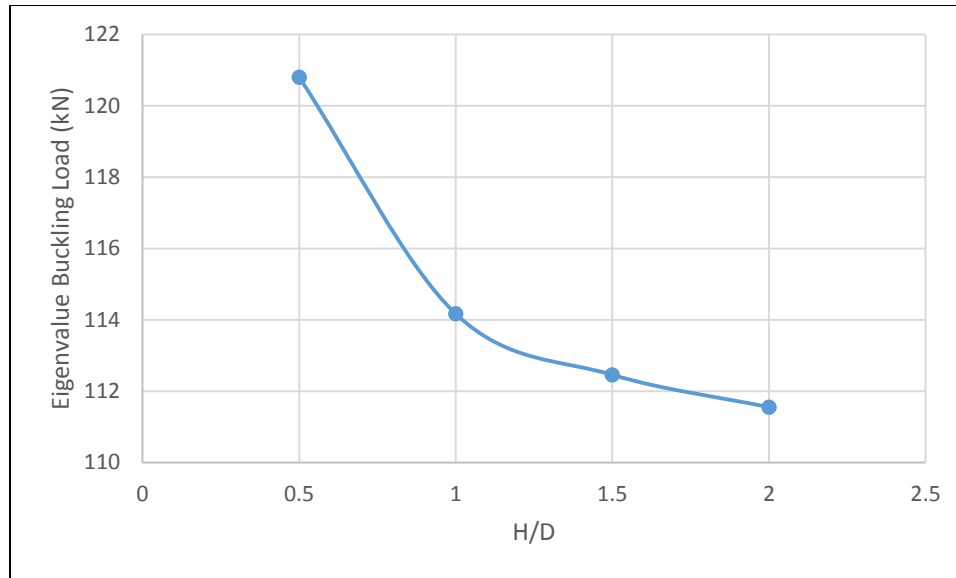


Figure 11. Lateral Eigenvalue Buckling Loads for Models with $D/t = 2,000$

The eigenvalue buckling loads for the cylindrical tanks with D/t ratios of 1000, 1500, and 2000 are shown in Figures 9, 10, and 11.

These results show that the eigenvalue buckling loads decrease as the H/D ratios increase if the D/t ratios are kept constant. Correspondingly, the eigenvalue buckling loads decrease as the D/t ratios increase. These eigenvalue bucklings are used to indicate the upper limit for nonlinear static buckling analysis. For the buckling mode shape, model 1 and model 12 which have the highest and lowest eigenvalue buckling loads are presented as Figures 12 and 13:

Model 1

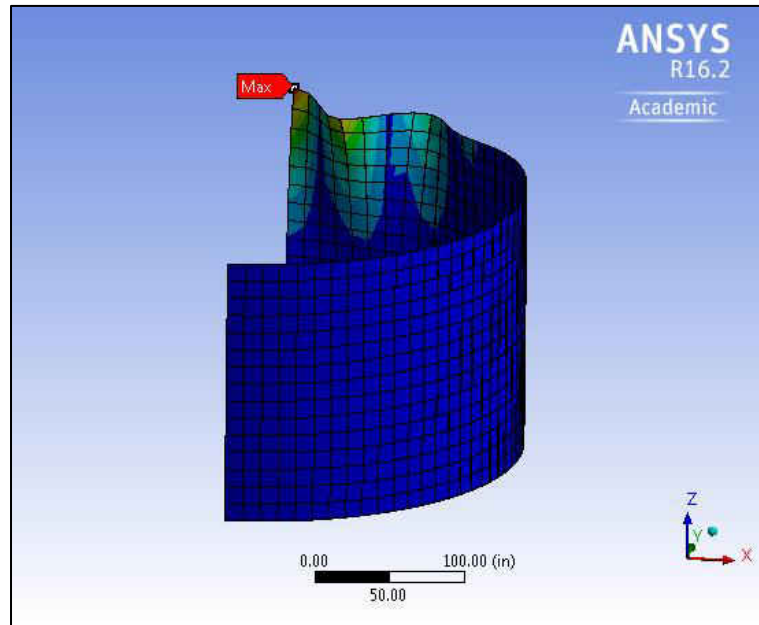


Figure 12. First buckling mode shape for Model 1

Model 12

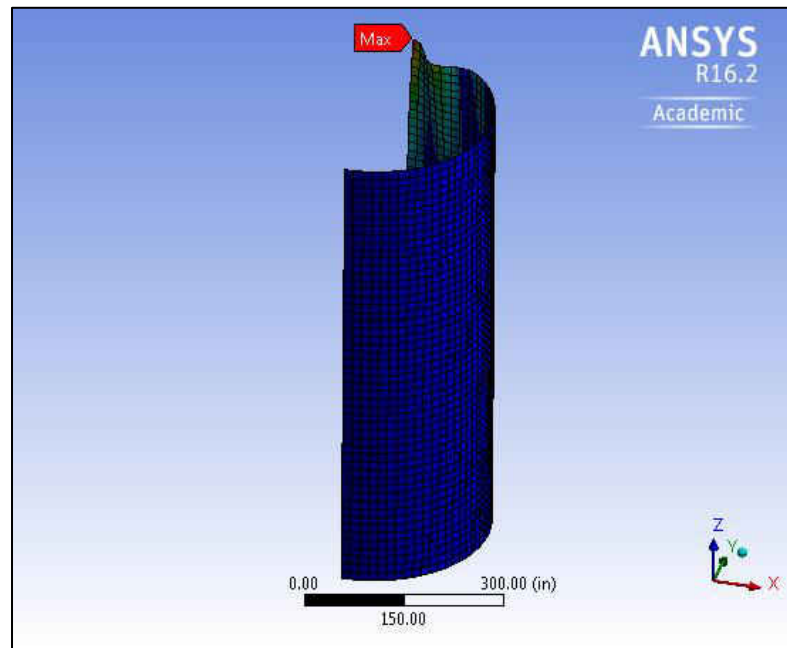


Figure 13. First buckling mode shape for Model 12

4.2 Nonlinear Static Buckling Analysis

Nonlinear buckling analysis is more accurate than the eigenvalue buckling analysis for the structures. Nonlinearity and large-deflection are employed in nonlinear buckling analysis. The approach of nonlinear buckling analysis is to continuously increase the applied load until the unstable point is reached. To study the post-buckling paths of the cylindrical tanks, the arc-length method is included within the nonlinear buckling analysis. Since the upper limit of buckling load was estimated by using eigenvalue buckling analysis in the previous section, the series of lateral load between zero to upper limit buckling load are applied to find the nonlinear buckling load for each model.

First, the nonlinear buckling analysis was started with the lateral load of approximately 90% of eigenvalue buckling load to investigate a maximum displacement at the top of cylindrical tanks. However, the lateral load had to be reduced if the simulation was unconverged. The maximum displacement node is tracked to plot the load-deflection curve. The radial displacements in the Y direction of the maximum displacement node were directly given in ANSYS.

The nonlinear buckling loads are less than the eigenvalue buckling loads for all models, and the nonlinear buckling loads range approximately 86% to 90% of the eigenvalue buckling loads as presented in Table 4.

Table 4. Summary results of eigenvalue and nonlinear buckling of lateral shear loads.

Model	H/D	D/t	Buckling Loads (N)		% Difference
			Eigenvalue	Nonlinear	
1	0.5	1,000	667,660	583,607	14.40
2	0.5	1,500	244,777	214,404	14.17
3	0.5	2,000	120,796	104,088	16.05
4	1	1,000	636,469	568,127	12.03
5	1	1,500	232,366	204,618	13.56
6	1	2,000	114,168	101,242	12.77
7	1.5	1,000	629,468	558,697	12.67
8	1.5	1,500	229,217	199,725	14.77
9	1.5	2,000	112,460	100,085	12.36
10	2	1,000	626,879	556,917	12.56
11	2	1,500	228,105	204,618	11.48
12	2	2,000	111,553	100,352	11.16

Importantly, in this study, all FEA models were modeled to be one-half models, so the lateral buckling loads that were found with nonlinear buckling analysis had to be multiplied by two to satisfy to real geometries. The applied lateral load cannot be directly observed, so the reaction forces were used to indicate the applied lateral loads. The load-deflection curves and post-buckling deflected shapes are presented in Figure 14 to Figure 37. The locations of buckling occur at the top of the cylindrical tanks for all models. For each cylindrical tank, the node which has maximum deflection in Y direction was tracked to plot the load-deflection curve.

Model 1

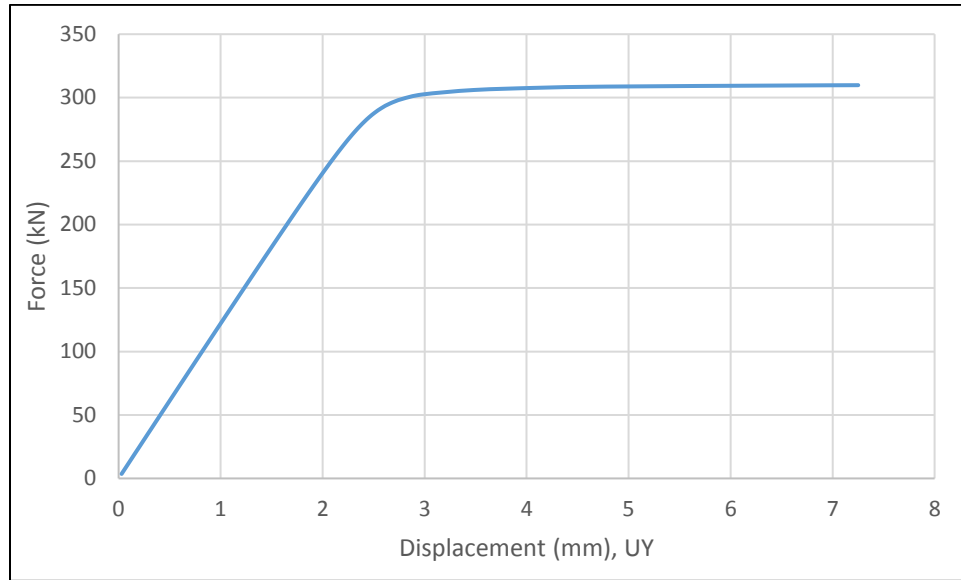


Figure 14. Load-Deflection curve of maximum deflection node for a half of Model 1

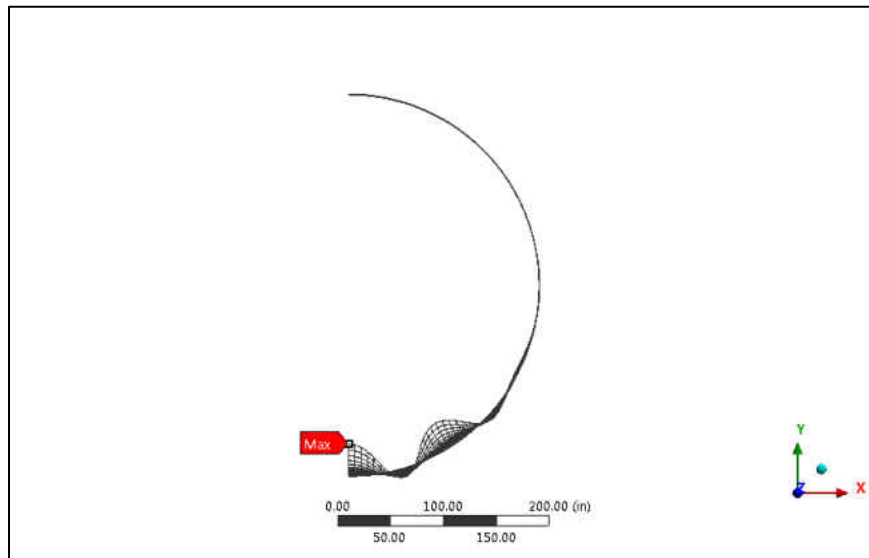


Figure 15. Post-buckling deflected shape of Model 1

Model 2

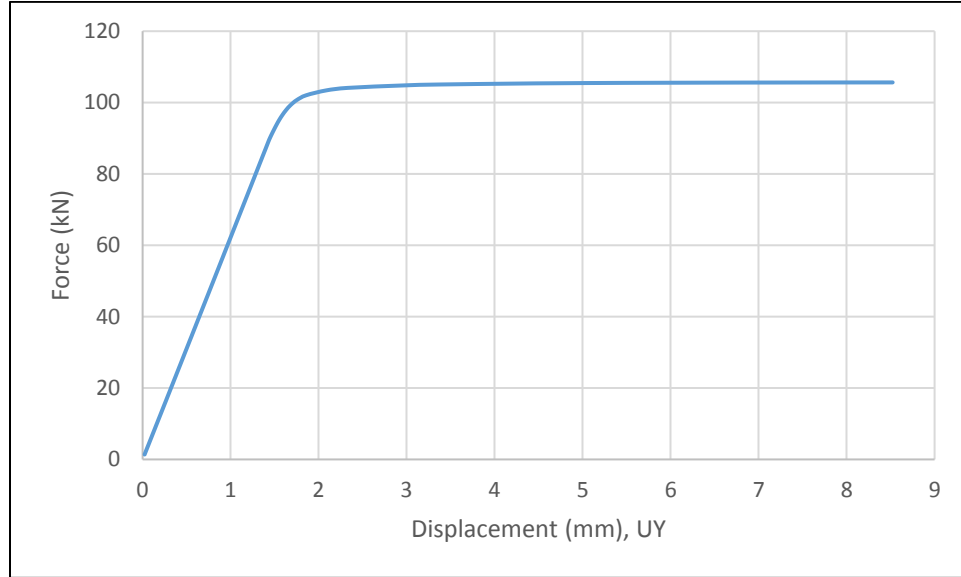


Figure 16. Load-Deflection curve of maximum deflection node for a half of Model 2

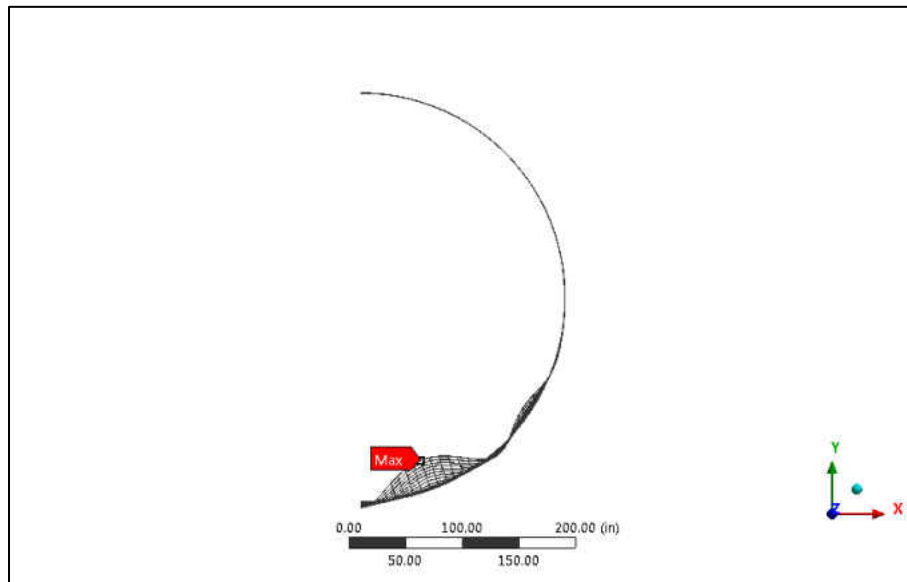


Figure 17. Post-buckling deflected shape of Model 2

Model 3

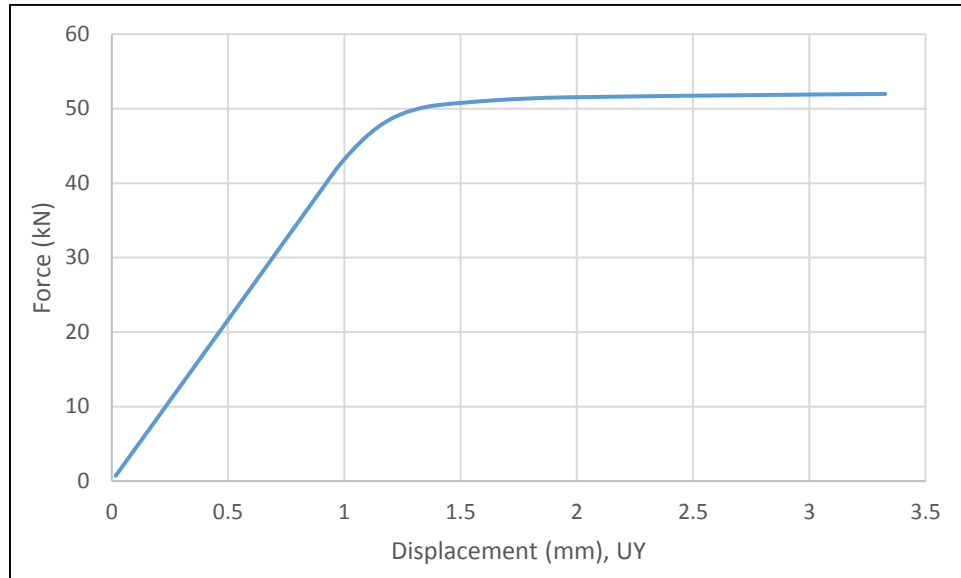


Figure 18. Load-Deflection curve of maximum deflection node for a half of Model 3

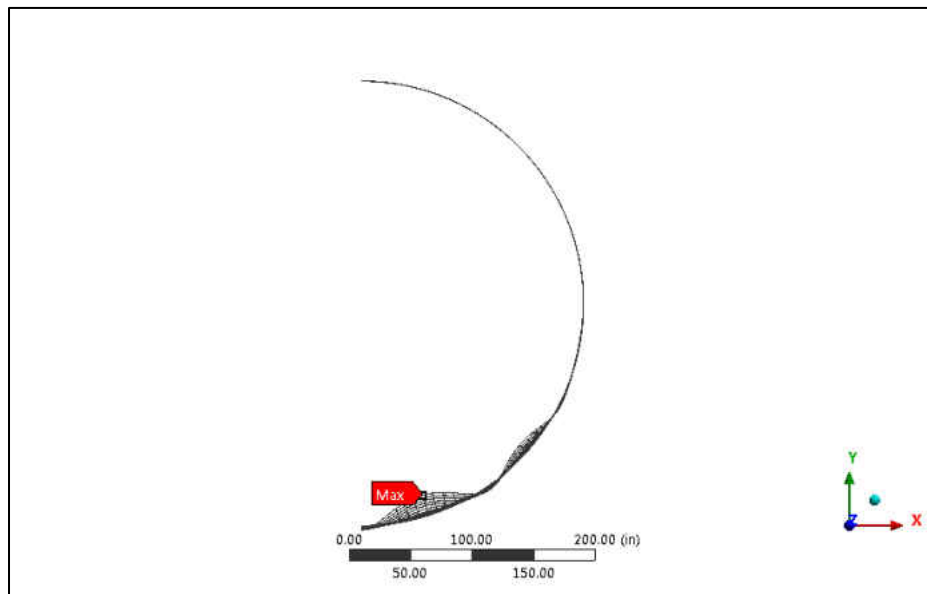


Figure 19. Post-buckling deflected shape of Model 3

Model 4

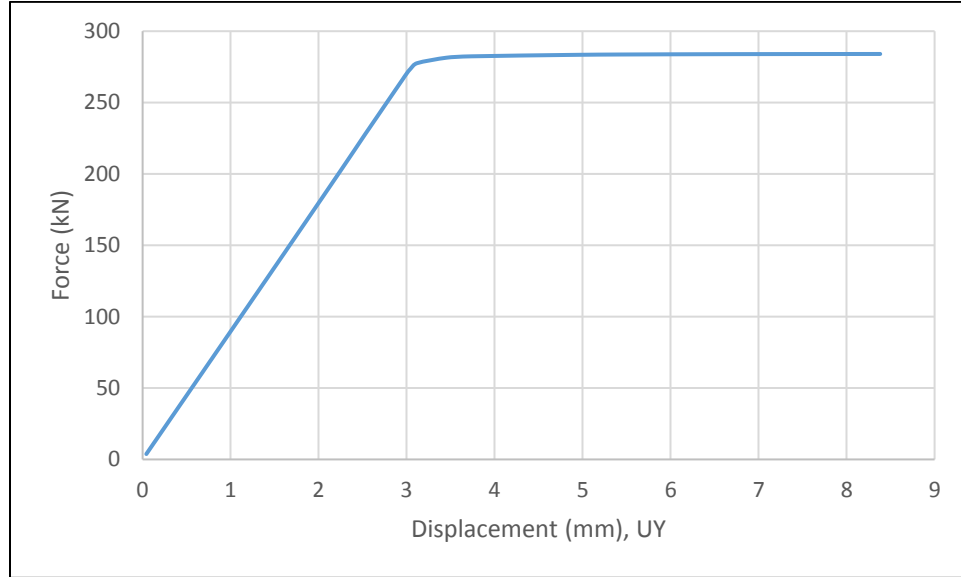


Figure 20. Load-Deflection curve of maximum deflection node for a half of Model 4

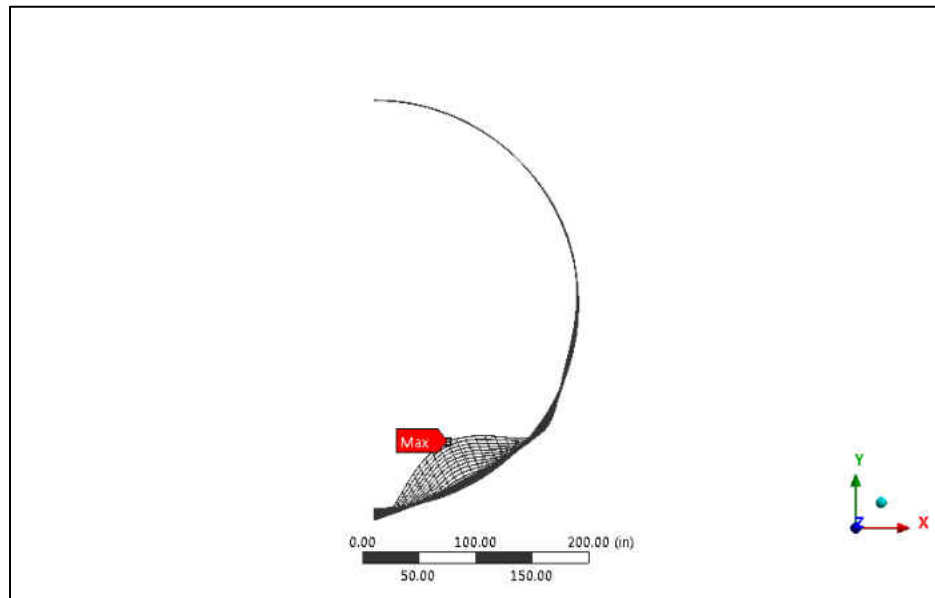


Figure 21. Post-buckling deflected shape of Model 4

Model 5

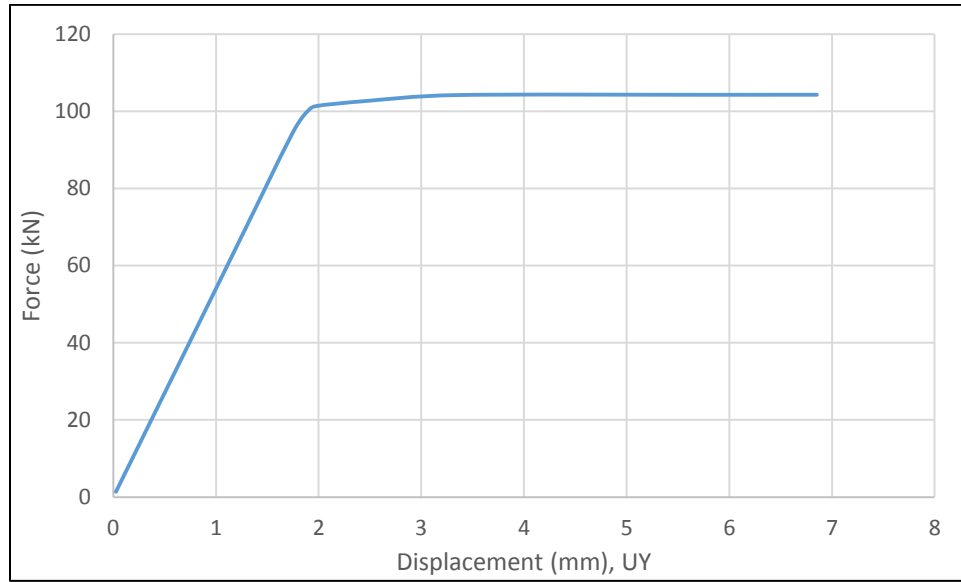


Figure 22. Load-Deflection curve of maximum deflection node for a half of Model 5

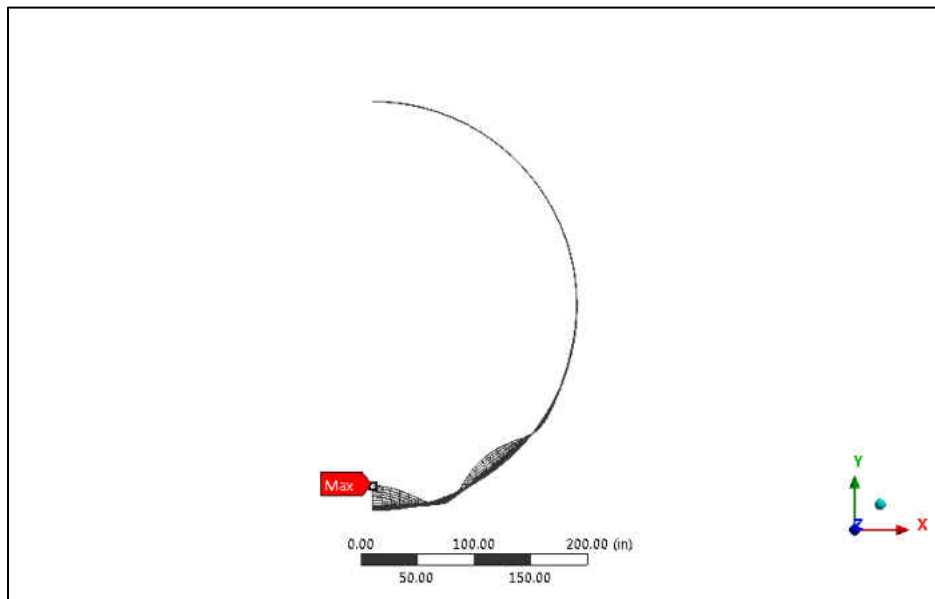


Figure 23. Post-buckling deflected shape of Model 5

Model 6

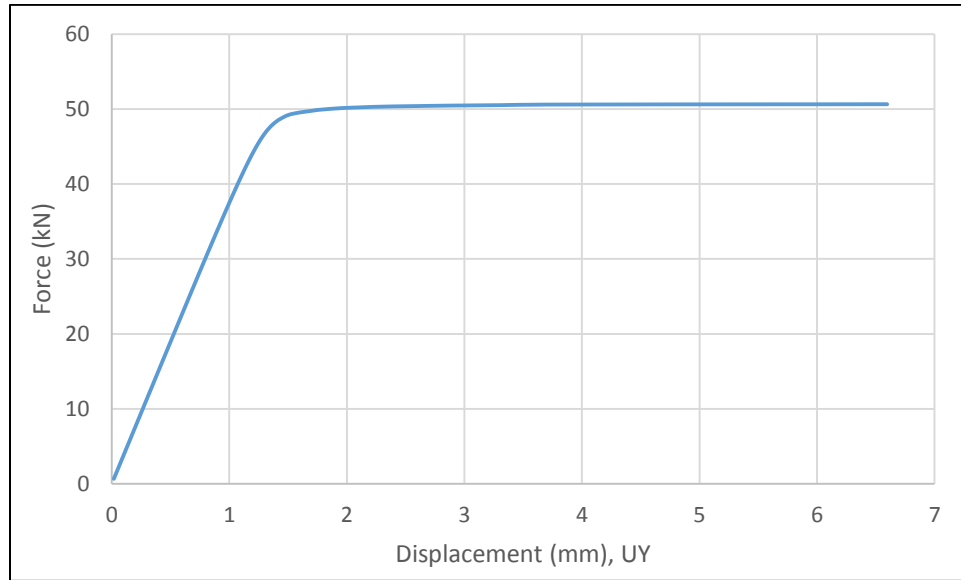


Figure 24. Load-Deflection curve of maximum deflection node for a half of Model 6

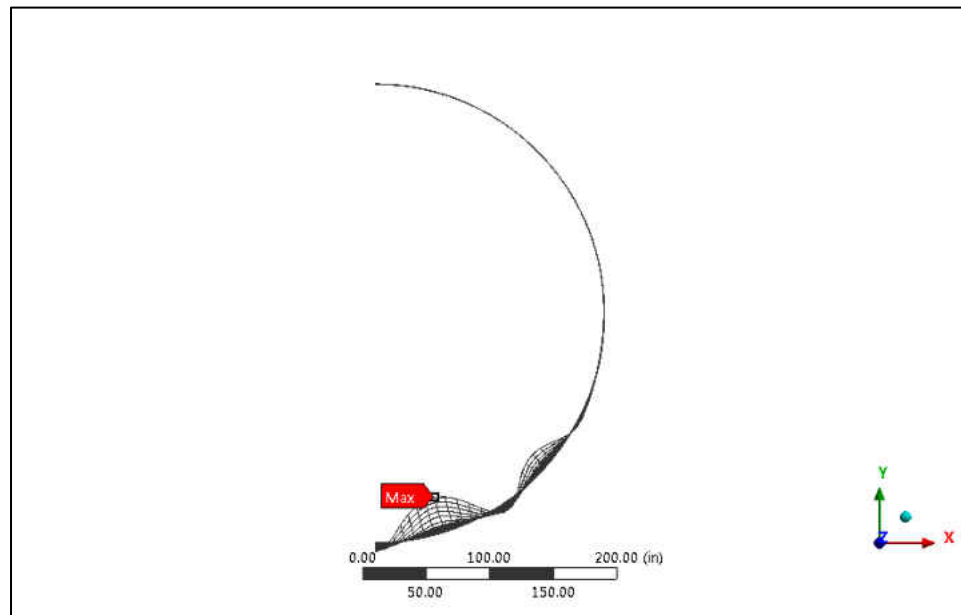


Figure 25. Post-buckling deflected shape of Model 6

Model 7

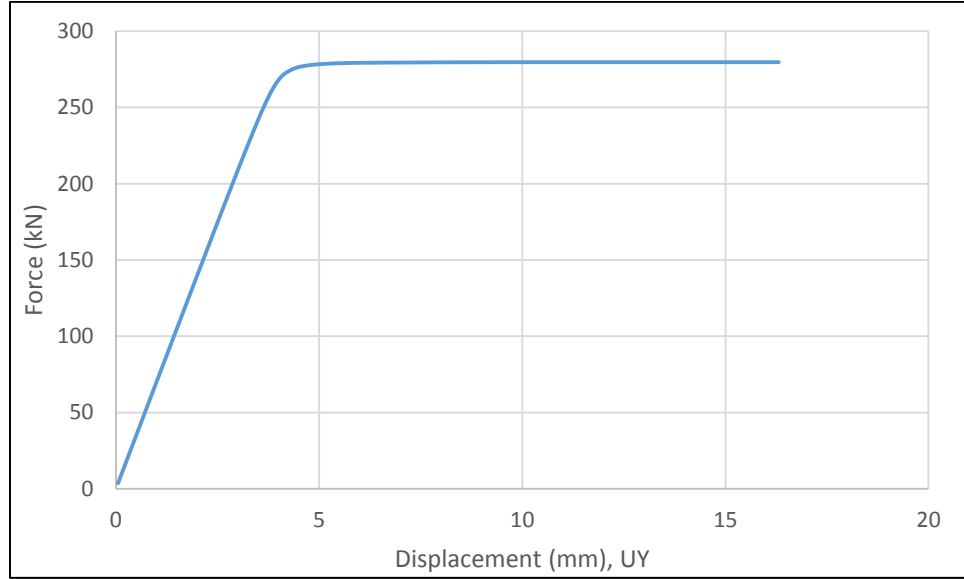


Figure 26. Load-Deflection curve of maximum deflection node for a half of Model 7

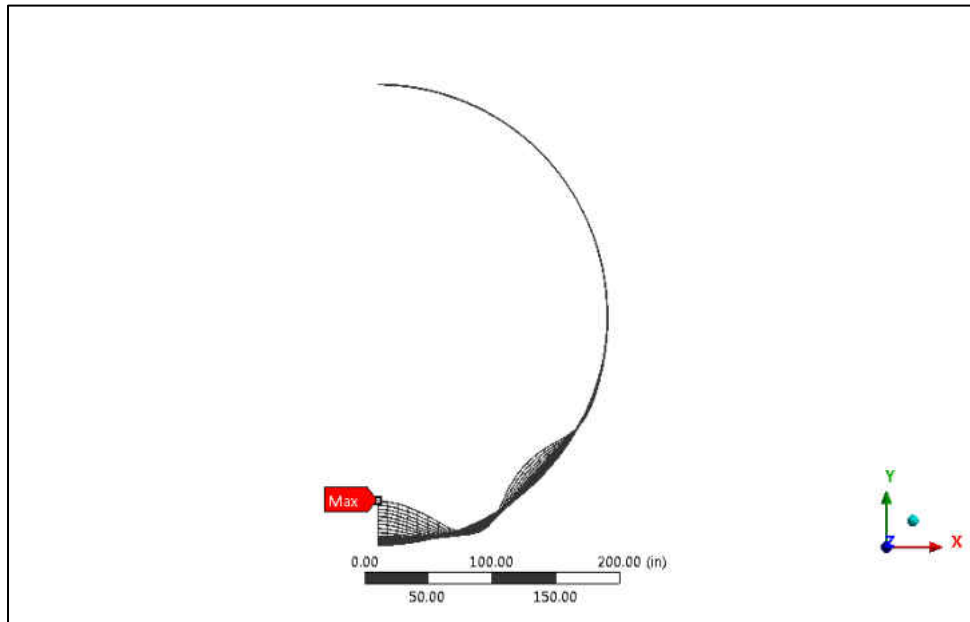


Figure 27. Post-buckling deflected shape of Model 7

Model 8

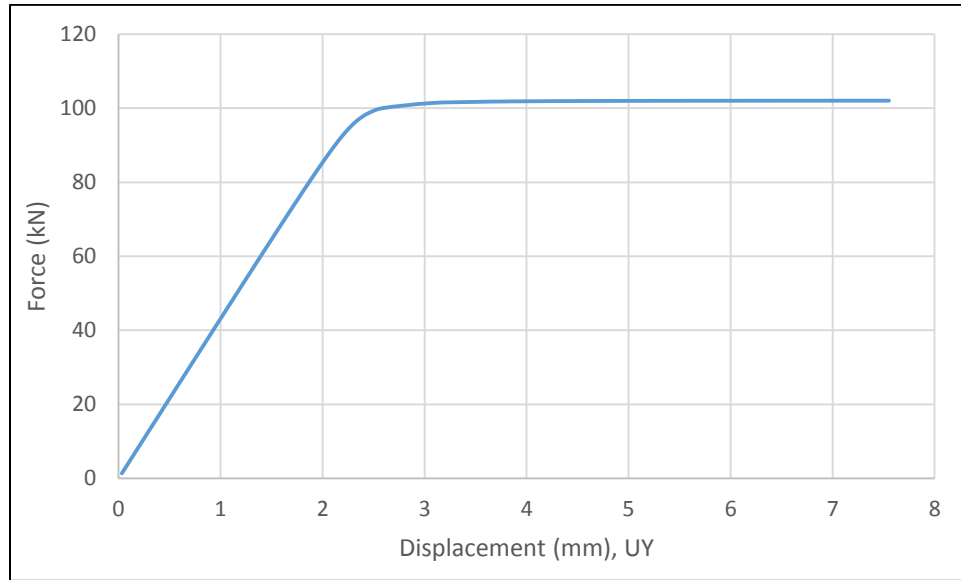


Figure 28. Load-Deflection curve of maximum deflection node for a half of Model 8

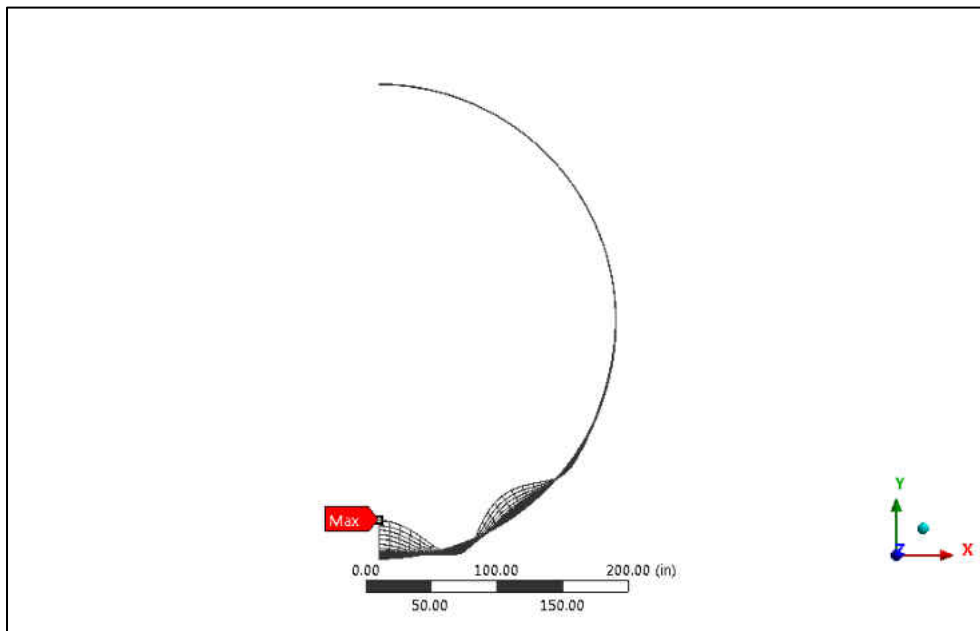


Figure 29. Post-buckling deflected shape of Model 8

Model 9

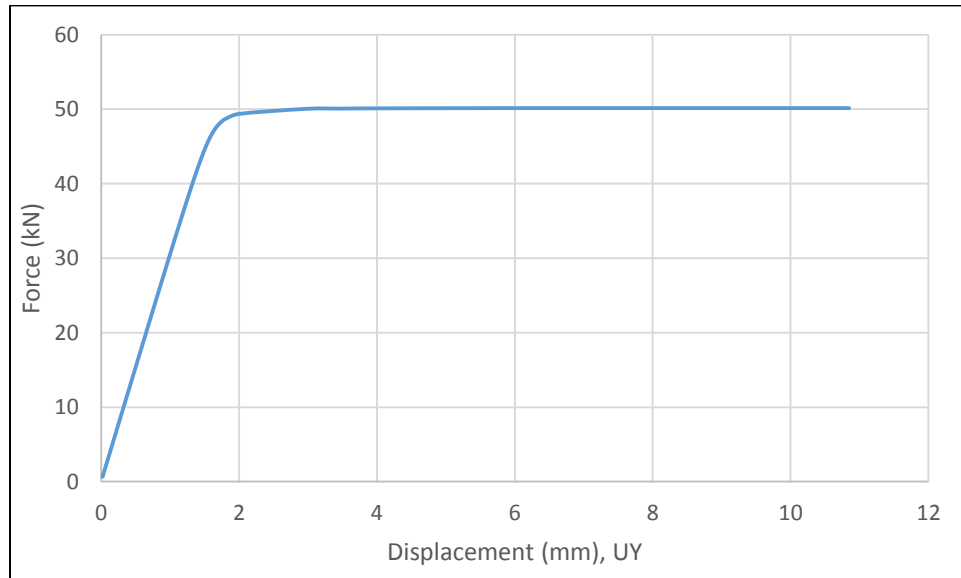


Figure 30. Load-Deflection curve of maximum deflection node for a half of Model 9

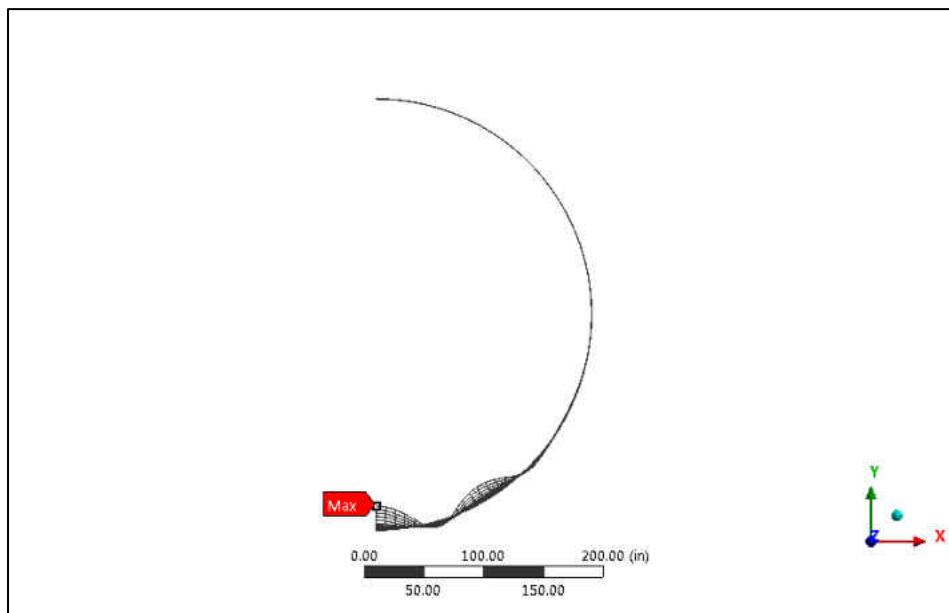


Figure 31. Post-buckling deflected shape of Model 9

Model 10

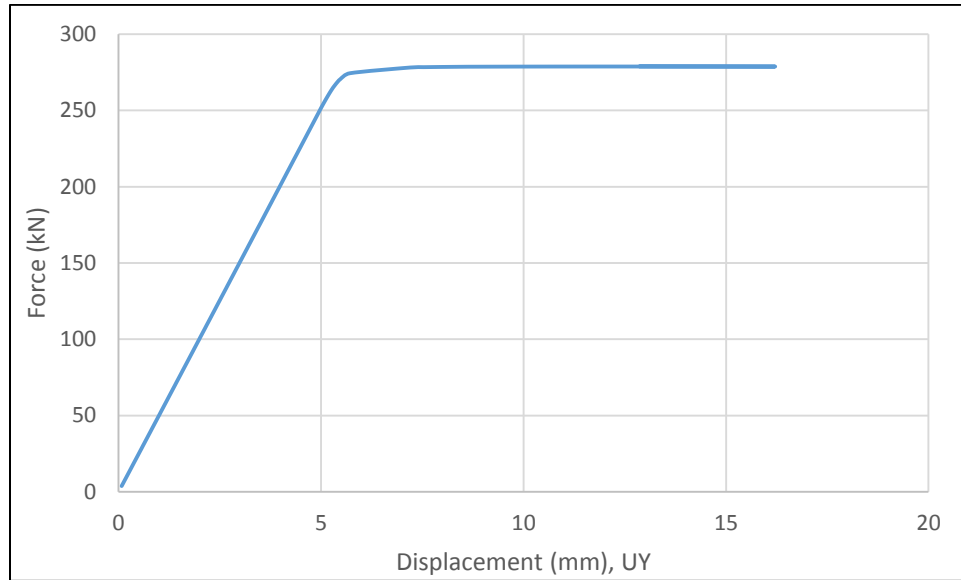


Figure 32. Load-Deflection curve of maximum deflection node for a half of Model 10

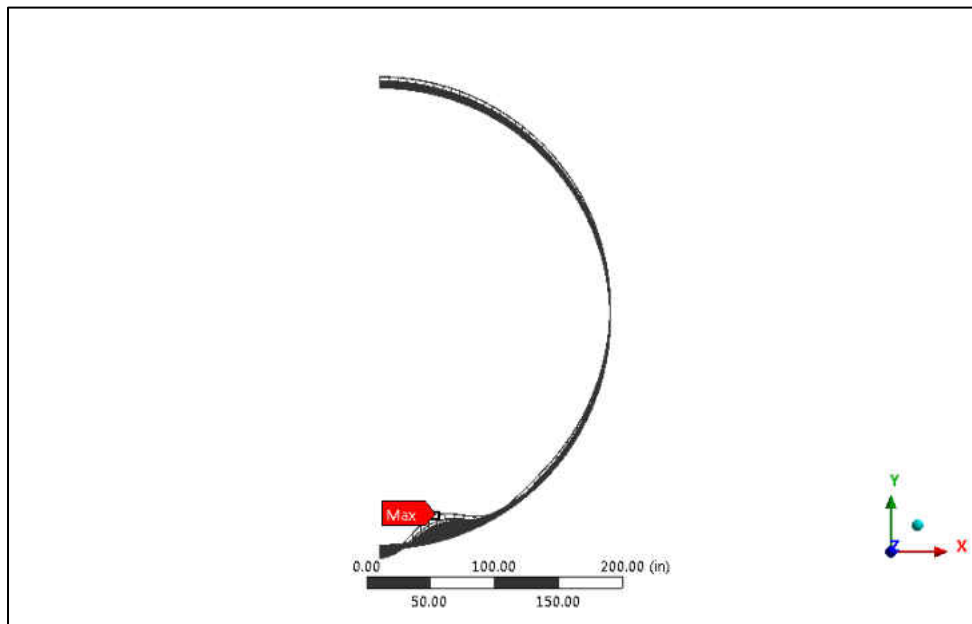


Figure 33. Post-buckling deflected shape of Model 10

Model 11

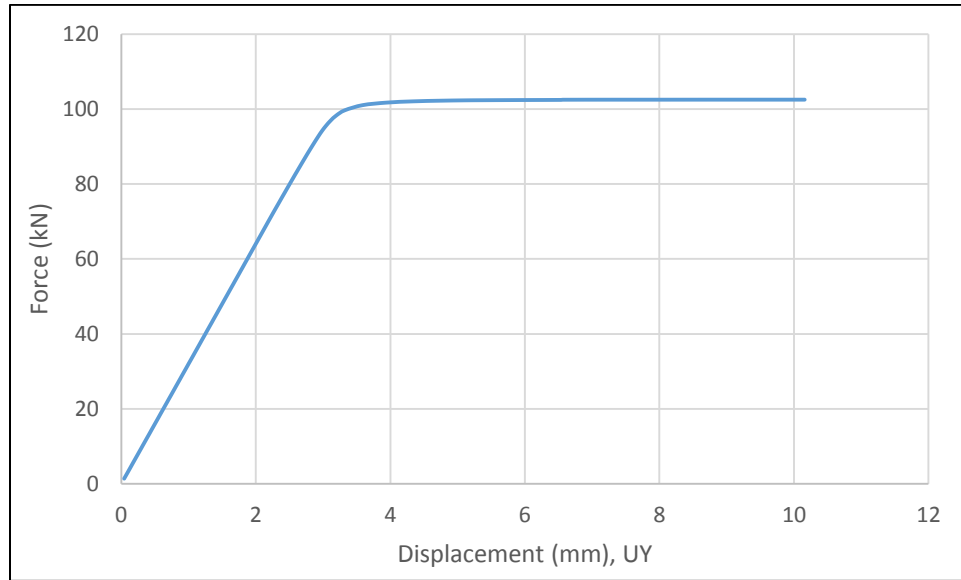


Figure 34. Load-Deflection curve of maximum deflection node for a half of Model 11

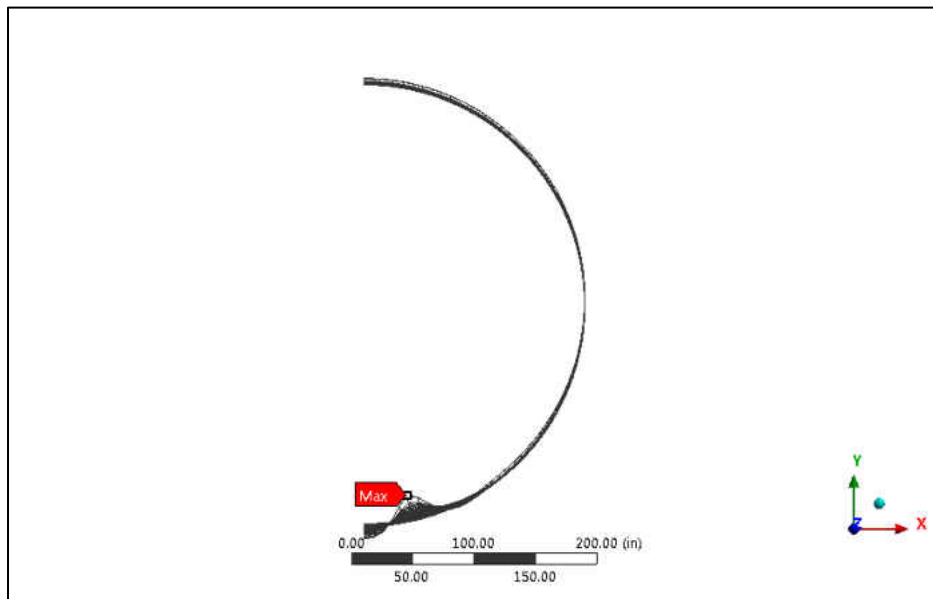


Figure 35. Post-buckling deflected shape of Model 11

Model 12

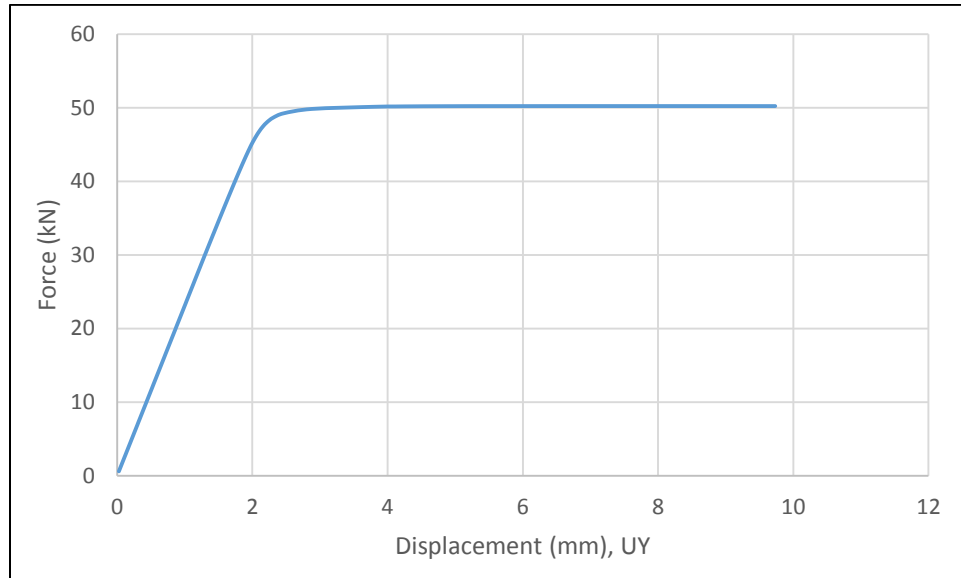


Figure 36. Load-Deflection curve of maximum deflection node for a half of Model 12

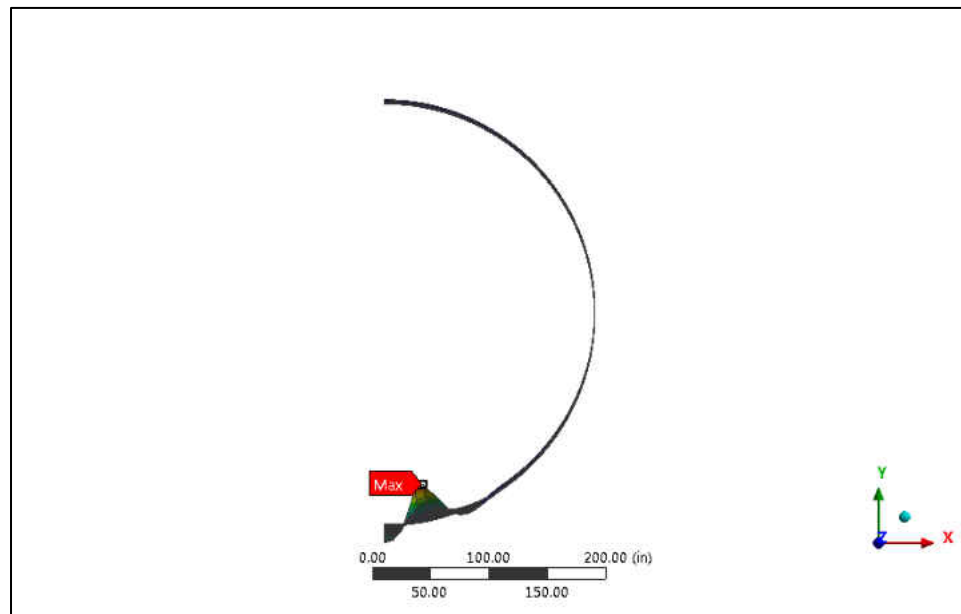


Figure 37. Post-buckling deflected shape of Model 12

CHAPTER V

MODAL ANALYSIS

Modal analysis is the method to investigate the vibration characteristics in terms of natural frequencies and mode shapes of the cylindrical tanks in ANSYS computer program. The natural frequencies and mode shapes are the parameters that are used to find mass and stiffness coefficients for Rayleigh damping method in the transient analysis in chapter 6. In the modal analysis, a structure is assumed to be a free vibration system, so the external force and damping do not exist in the model analysis. The equation of motion for an undamped system vibrating freely is expressed in matrix notation as in Equation 4.

$$[M]\{\ddot{u}\} + [K]\{u\} = \{0\} \quad (4)$$

Where: $[M]$ = structural mass matrix
 $[K]$ = structural stiffness matrix
 $\{\ddot{u}\}$ = nodal acceleration vector
 $\{u\}$ = nodal displacement vector

For a linear system, free vibration will be harmonic of the form in Equation 5:

$$\{u\} = \{\phi_i\} \cos \omega_i t \quad (5)$$

Where: $\{\phi_i\}$ = eigenvector representing the mode shape of the i^{th} natural frequency
 $\omega_i = i^{th}$ natural circular frequency in term of radians per unit time
 t = time

Substituting Equation (5) in Equation (4):

$$(-\omega^2[M] + [K])\{\phi_i\} = \{0\} \quad (6)$$

Equation (6) is satisfied if $(-\omega^2[M] + [K])$ or $\{\phi_i\}$ is equal to zero. However, the condition that the eigenvector is zero, $\{\phi_i\} = 0$, is trivial; therefore, this condition is not of interest. The condition of interest becomes,

$$|[K] - \omega^2[M]| = 0 \quad (7)$$

The finite element simulation may solve up to n values of ω^2 and $\{\phi_i\}$ to satisfy the equation (6) where n is the number of degree of freedoms (DOFs). In the modal analysis, in ANSYS, the output are the natural frequencies (f) instead of the natural circular frequencies (ω) which are related by in Equation (8).

$$f_i = \frac{\omega}{2\pi} \quad (8)$$

Where: $f_i = i^{th}$ natural frequency in term of cycles per unit time

The first natural frequencies for both empty and tanks filled with water up to 90% of their height are presented in Table 5. The first natural frequencies decrease when the H/D ratios increase, and the natural frequencies decrease when the D/t ratios increase. The first natural frequencies of the cylindrical tanks filled with water up to 90% of their height are significantly smaller than the empty cylindrical tanks.

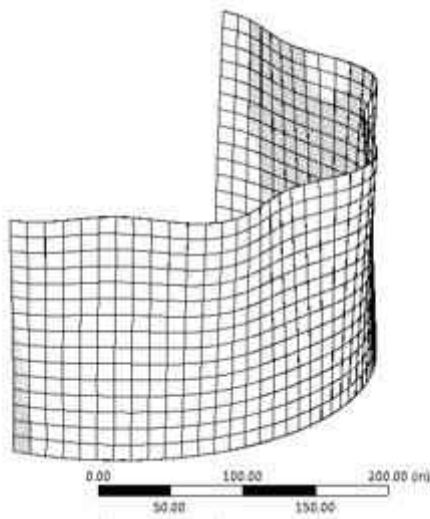
Table 5. First natural frequencies

Model	H/D	D/t	Natural Frequencies (Hz)	
			Depth of Water to Height of the Tank	
			0%	90%
1	0.5	1,000	11.495	2.207
2	0.5	1,500	9.391	2.204
3	0.5	2,000	8.169	2.201
4	1.0	1,000	4.718	1.703
5	1.0	1,500	3.858	1.701
6	1.0	2,000	3.444	1.698
7	1.5	1,000	3.685	1.188
8	1.5	1,500	3.134	1.186
9	1.5	2,000	2.657	1.185
10	2.0	1,000	2.788	0.845
11	2.0	1,500	2.272	0.828
12	2.0	2,000	1.973	0.811

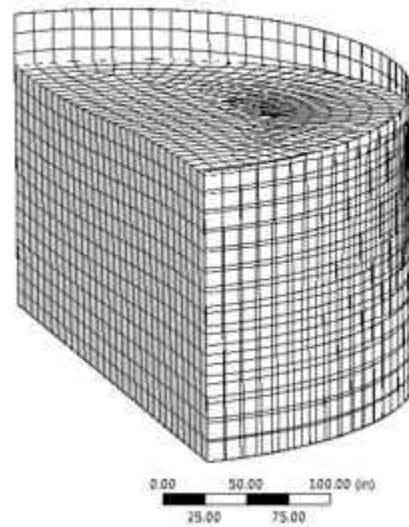
Model 1

Table 6. Natural Frequencies of Model 1

Mode	Natural Frequencies (Hz)	
	Depth of Water to Height of the Tank	
	0%	90%
1	11.495	2.207
2	11.663	3.290
3	12.61	3.308
4	12.826	4.119
5	14.728	4.229
6	15.301	4.299
7	17.193	4.815
8	20.027	5.039
9	20.128	5.310
10	23.493	5.467



(a) Scale 20:1



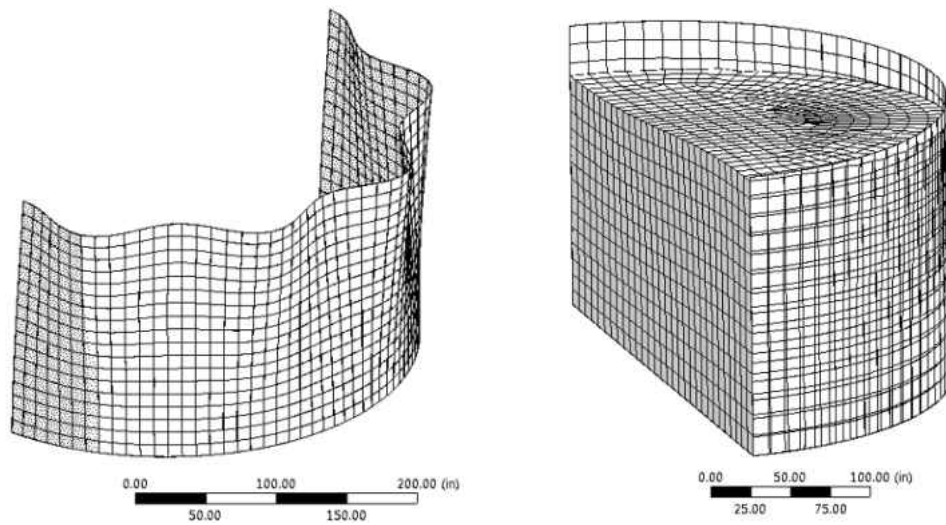
(b) Scale 250:1

Figure 38. (a) First Shell Mode and (b) First Mode with 90% water depth of Model 1

Model 2

Table 7. Natural Frequencies of Model 2

Mode	Natural Frequencies (Hz)	
	Depth of Water to Height of the Tank	
	0%	90%
1	9.391	2.204
2	9.5338	3.286
3	10.102	3.307
4	10.345	4.115
5	11.659	4.215
6	11.857	4.286
7	13.359	4.810
8	14.925	5.032
9	15.375	5.274
10	17.673	5.463



(a) Scale 20:1

(b) Scale 250:1

Figure 39. (a) First Shell Mode and (b) First Mode with 90% water depth of Model 2

Model 3

Table 8. Natural Frequencies of Model 3

Mode	Natural Frequencies (Hz)	
	Depth of Water to Height of the Tank	
	0%	90%
1	8.169	2.201
2	8.440	3.283
3	8.512	3.306
4	9.194	4.112
5	9.603	4.200
6	10.317	4.274
7	11.607	4.803
8	11.733	5.026
9	13.395	5.238
10	14.811	5.459

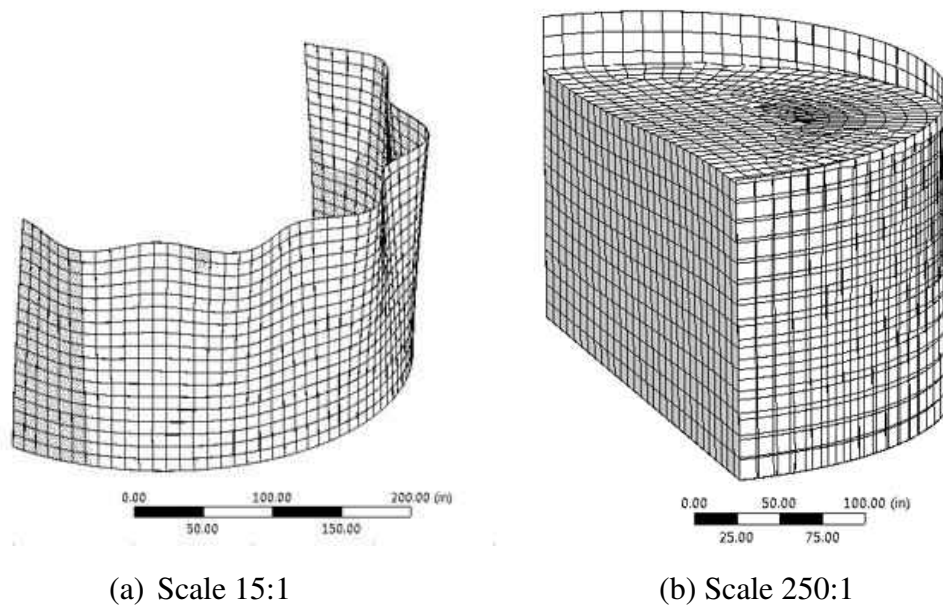


Figure 40. (a) First Shell Mode and (b) First Mode with 90% water depth of Model 3

Model 4

Table 9. Natural Frequencies of Model 4

Mode	Natural Frequencies (Hz)	
	Depth of Water to Height of the Tank	
	0%	90%
1	4.718	1.703
2	4.782	2.592
3	5.676	2.863
4	5.842	3.139
5	7.098	3.612
6	8.689	3.682
7	8.893	3.700
8	10.998	3.878
9	13.361	3.914
10	13.394	4.511

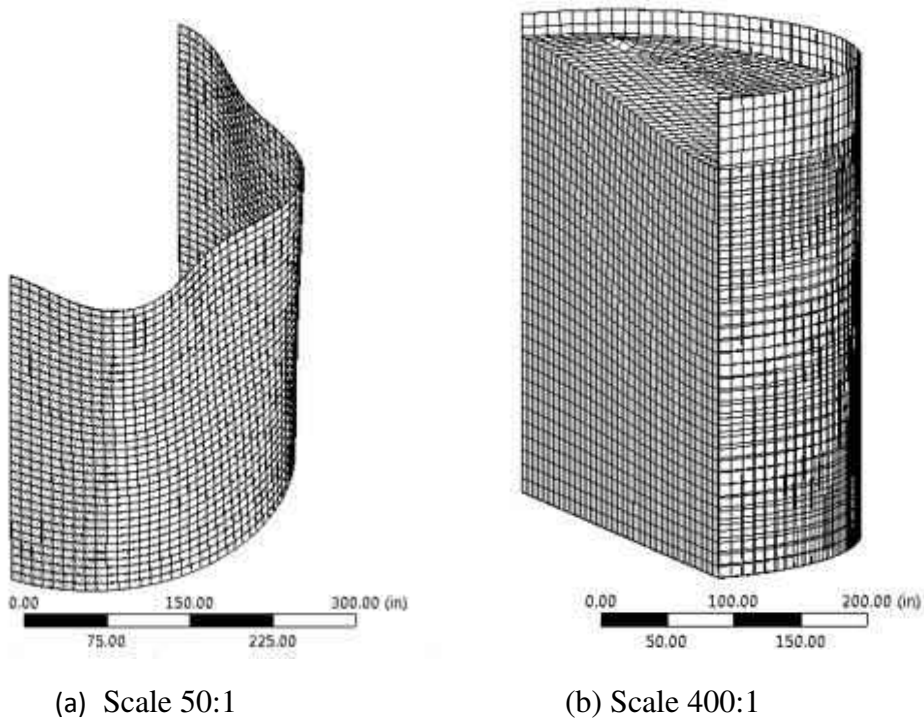


Figure 41. (a) First Shell Mode and (b) First Mode with 90% water depth of Model 4

Model 5

Table 10. Natural Frequencies of Model 5

Mode	Natural Frequencies (Hz)	
	Depth of Water to Height of the Tank	
	0%	90%
1	3.858	1.701
2	4.142	2.582
3	4.294	2.851
4	4.921	3.137
5	5.698	3.611
6	6.033	3.677
7	7.393	3.679
8	8.636	3.824
9	8.968	3.891
10	10.745	4.407

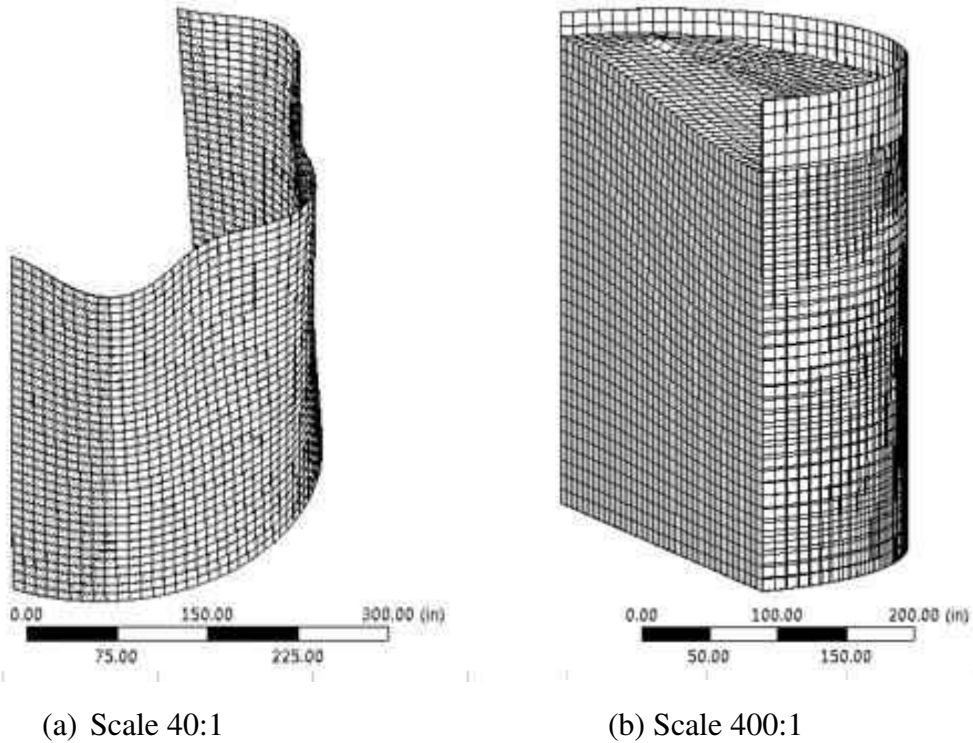


Figure 42. (a) First Shell Mode and (b) First Mode with 90% water depth of Model 5

Model 6

Table 11. Natural Frequencies of Model 6

Mode	Natural Frequencies (Hz)	
	Depth of Water to Height of the Tank	
	0%	90%
1	3.444	1.698
2	3.472	2.571
3	3.877	2.838
4	4.128	3.134
5	4.629	3.609
6	5.605	3.647
7	5.635	3.677
8	6.763	3.776
9	8.083	3.866
10	8.599	4.277

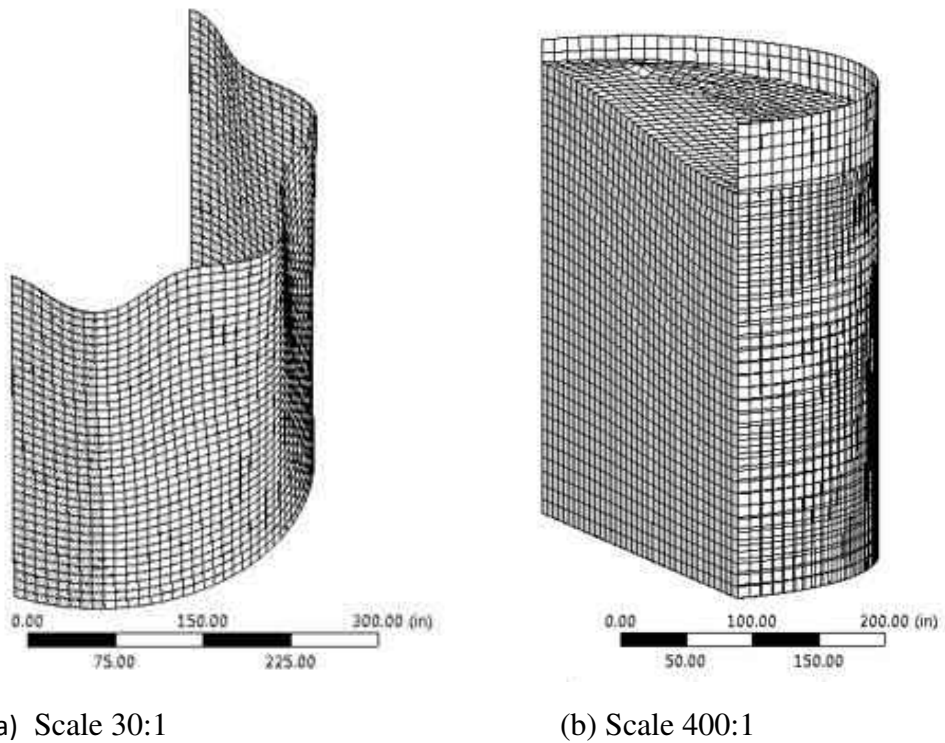


Figure 43. (a) First Shell Mode and (b) First Mode with 90% water depth of Model 6

Model 7

Table 12. Natural Frequencies of Model 7

Mode	Natural Frequencies (Hz)	
	Depth of Water to Height of the Tank	
	0%	90%
1	3.685	1.188
2	4.209	1.512
3	4.318	1.994
4	5.397	2.018
5	6.792	2.208
6	6.989	2.315
7	8.897	2.401
8	9.623	2.593
9	9.838	2.663
10	10.486	2.709

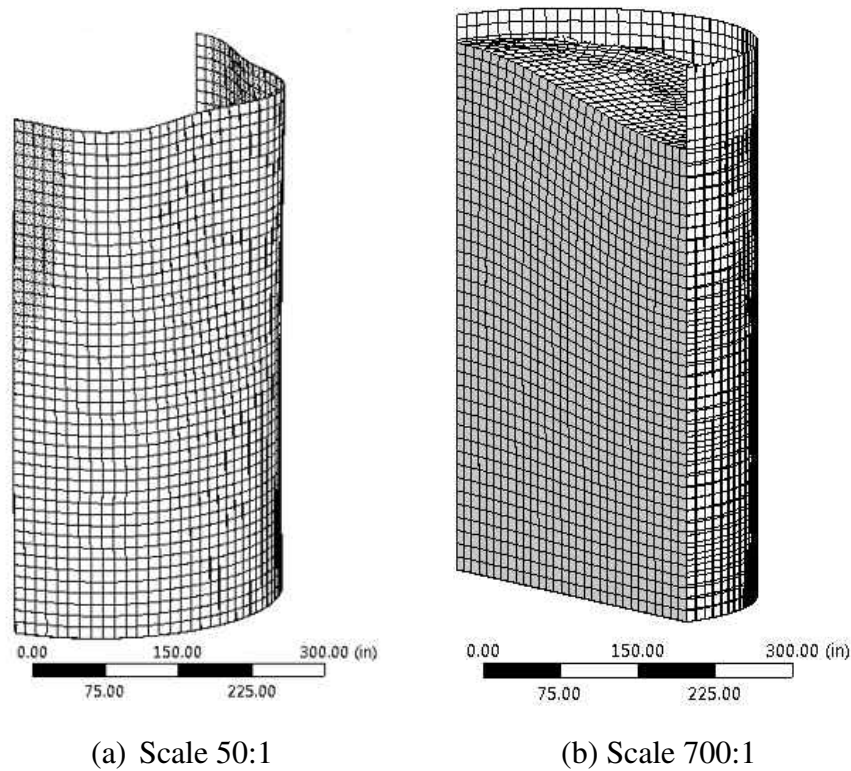


Figure 44. (a) First Shell Mode and (b) First Mode with 90% water depth of Model 7

Model 8

Table 13. Natural Frequencies of Model 8

Mode	Natural Frequencies (Hz)	
	Depth of Water to Height of the Tank	
	0%	90%
1	3.134	1.186
2	3.150	1.507
3	3.746	1.990
4	4.152	2.008
5	4.730	2.207
6	5.968	2.300
7	6.761	2.398
8	7.422	2.592
9	7.988	2.653
10	8.006	2.661

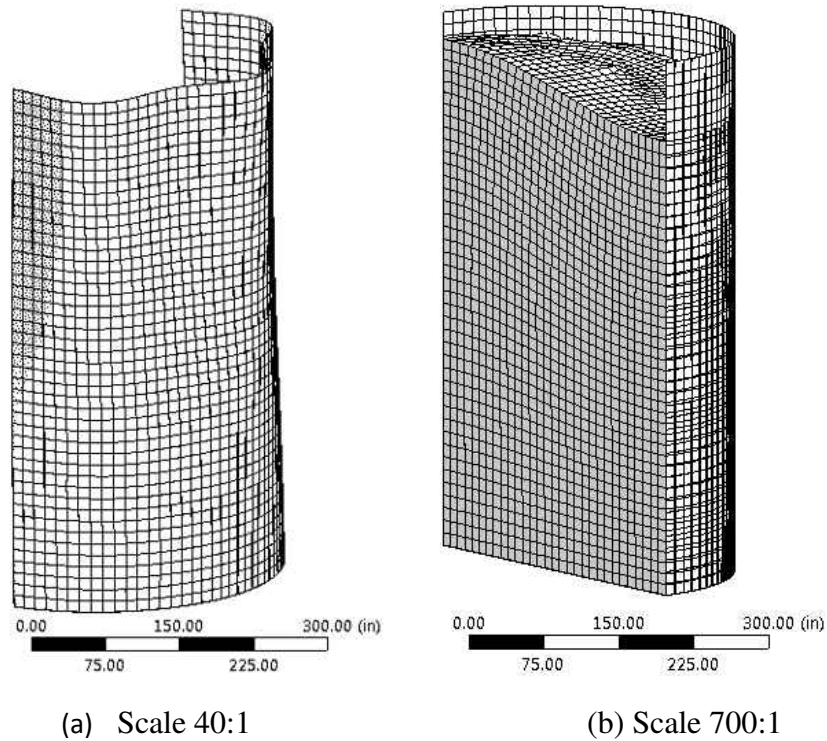


Figure 45. (a) First Shell Mode and (b) First Mode with 90% water depth of Model 8

Model 9

Table 14. Natural Frequencies of Model 9

Mode	Natural Frequencies (Hz)	
	Depth of Water to Height of the Tank	
	0%	90%
1	2.657	1.185
2	2.940	1.503
3	2.957	1.987
4	3.619	1.997
5	4.091	2.206
6	4.513	2.282
7	5.587	2.394
8	6.750	2.591
9	6.824	2.625
10	6.903	2.638

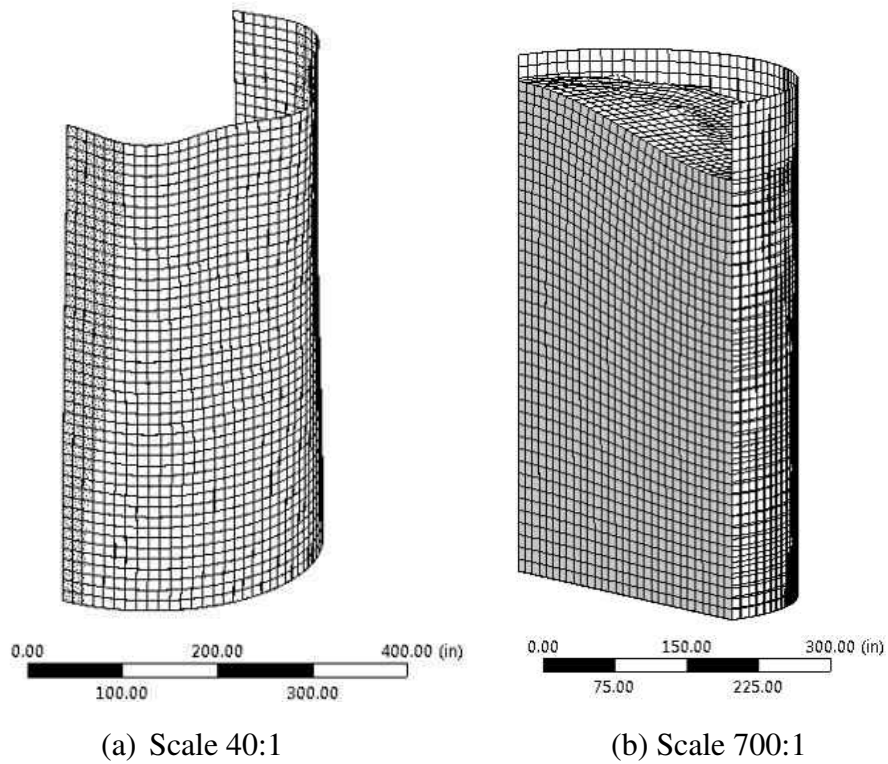


Figure 46. (a) First Shell Mode and (b) First Mode with 90% water depth of Model 9

Model 10

Table 15. Natural Frequencies of Model 10

Mode	Natural Frequencies (Hz)	
	Depth of Water to Height of the Tank	
	0%	90%
1	2.788	0.845
2	2.963	0.967
3	3.904	1.203
4	3.998	1.417
5	5.261	1.473
6	6.920	1.546
7	7.155	1.555
8	7.420	1.649
9	7.865	1.719
10	7.957	1.792

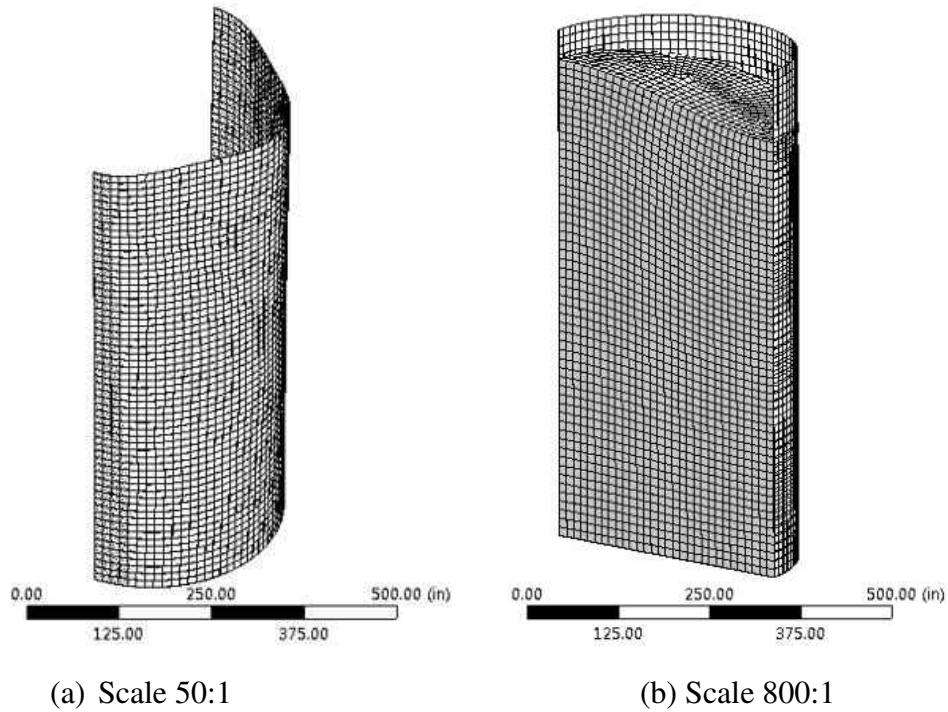


Figure 47. (a) First Shell Mode and (b) First Mode with 90% water depth of Model 10

Model 11

Table 16. Natural Frequencies of Model 11

Mode	Natural Frequencies (Hz)	
	Depth of Water to height of the Tank	
	0%	90%
1	2.272	0.828
2	2.528	0.950
3	2.721	1.181
4	3.557	1.397
5	3.950	1.444
6	4.637	1.525
7	5.918	1.531
8	5.942	1.619
9	5.982	1.706
10	6.694	1.772

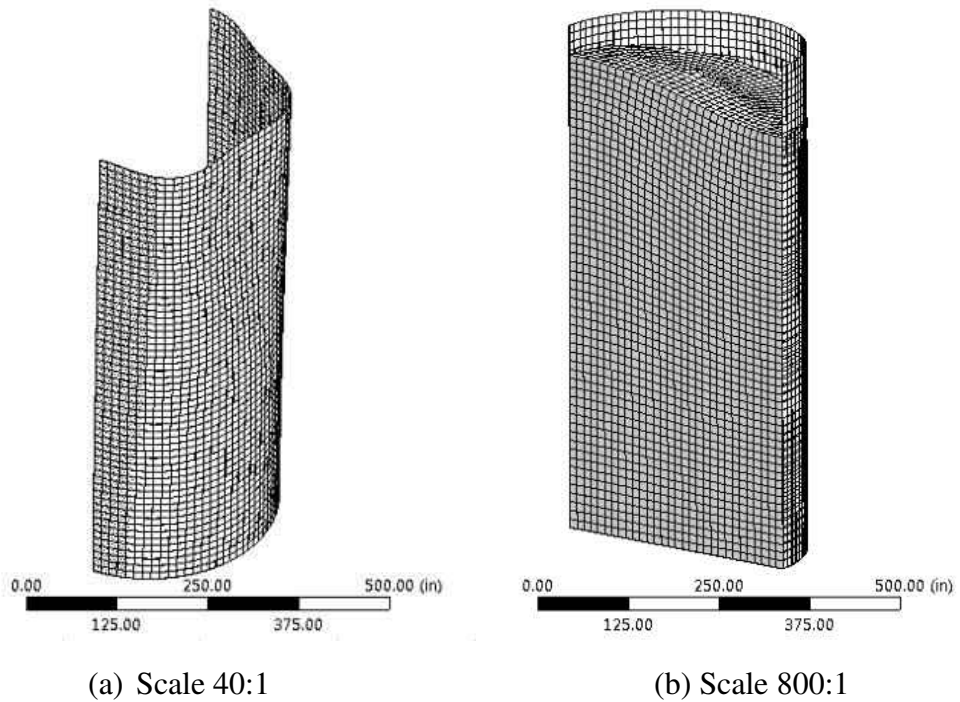


Figure 48. (a) First Shell Mode and (b) First Mode with 90% water depth of Model 11

Model 12

Table 17. Natural Frequencies of Model 12

Mode	Natural Frequencies (Hz)	
	Depth of Water to Height of the Tank	
	0%	90%
1	1.973	0.811
2	2.158	0.928
3	2.430	1.154
4	2.719	1.362
5	3.501	1.413
6	3.932	1.488
7	4.451	1.492
8	5.113	1.583
9	5.393	1.657
10	5.454	1.734

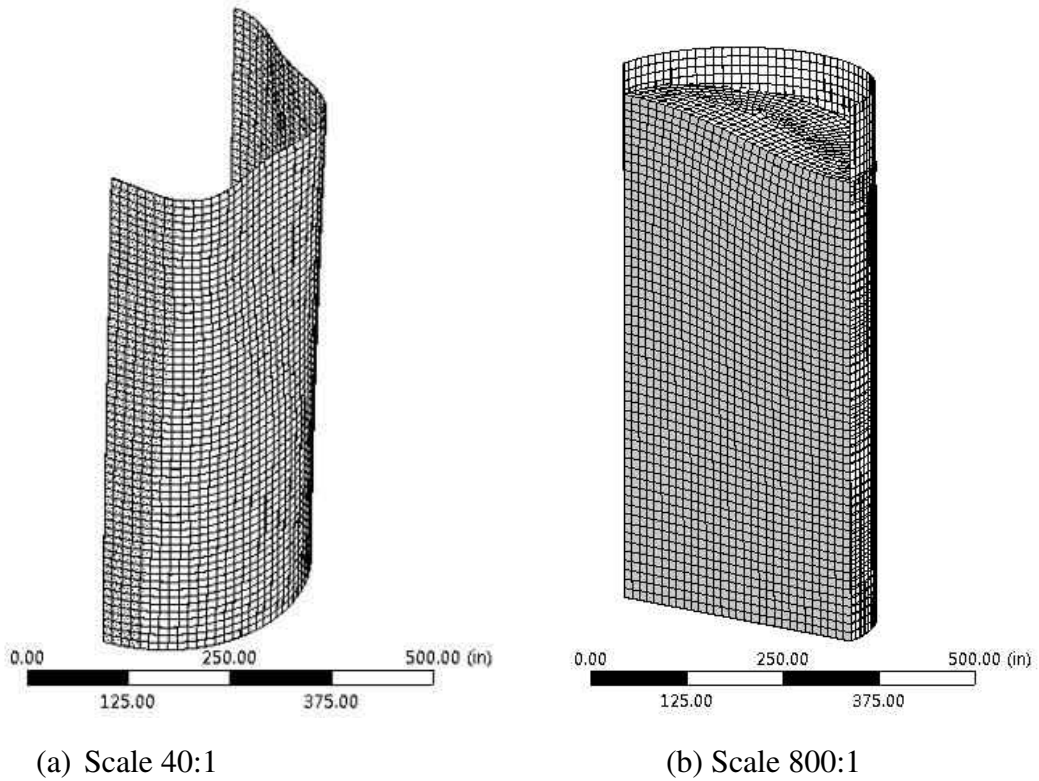


Figure 49. (a) First Shell Mode and (b) First Mode with 90% water depth of Model 12

CHAPTER VI

TRANSIENT DYNAMIC ANALYSIS

6.1 Definition and Method

The transient dynamic analysis is the technique for the response of a structure subjected to a time-dependent loading. In addition, inertia and damping effects are considered for the transient dynamic analysis. The equation of motion, equation (9), is solved by the transient structure simulation in ANSYS [19].

$$[M]\{\ddot{u}\} + [C]\{\dot{u}\} + [K]\{u\} = \{F_{(t)}\} \quad (9)$$

Where:

- $[M]$ = mass matrix
- $[C]$ = damping matrix
- $[K]$ = stiffness matrix
- $\{\ddot{u}\}$ = nodal acceleration vector
- $\{\dot{u}\}$ = nodal velocity vector
- $\{u\}$ = nodal displacement
- $\{F_{(t)}\}$ = load vector
- t = time

In this study, the transient dynamic analysis is to investigate the dynamic buckling capacity of twelve different geometries of the cylindrical tanks. These cylindrical tanks are subjected to two different earthquake accelerations, and the pseudo-paths for these earthquakes are generated. All twelve cylindrical tank models are modeled to be fixed-free support. First, the empty cylindrical tanks were analyzed, so the interaction

between the water and cylindrical tanks was excluded. The cylindrical tanks filled with 90% of liquid to the height are analyzed to investigate the effects of the interaction between the liquid and cylindrical tanks in terms of buckling loads. One-half of the cylindrical tank was modeled due to the symmetrical geometry. Large deformations and elastoplastic stress-strain properties were assumed for the cylindrical tanks. Bilinear isotropic hardening is included with the yield stress of 50,000 psi (344.74 MPa) and the tangent modulus of 2,000 ksi (13,790 MPa). The earthquake excitations were applied to the models in terms of accelerations in the Y direction.

The Budiansky and Roth criterion [20] was employed to find the buckling loads in nonlinear transient analyses for both the empty and liquid filled tanks. Different peak ground accelerations (PGA) were plotted against the radial displacements in Y direction for the maximum radial displacement node.

6.2 Rayleigh Damping

Rayleigh Damping is a procedure of classical damping, which is used in ANSYS computer program. Rayleigh damping is an appropriate idealization if similar damping mechanisms are distributed throughout the structure.

From on the equation of motion:

$$[M]\{\ddot{u}\} + [C]\{\dot{u}\} + [K]\{u\} = \{F_{(t)}\} \quad (9)$$

and, Rayleigh damping:

$$[C] = \alpha [M] + \beta [K] \quad (10)$$

Where: α = mass coefficient
 β = stiffness coefficient

$$\alpha = \frac{2\omega_i\omega_j(\omega_i\zeta_j - \omega_j\zeta_i)}{\omega_i^2 - \omega_j^2} \quad (11)$$

$$\beta = \frac{2(\omega_i\zeta_i - \omega_j\zeta_j)}{\omega_i^2 - \omega_j^2} \quad (12)$$

Since damping ratio is assumed to be constant in this study:

$$\zeta_i = \zeta_j = \zeta \quad (13)$$

$$\alpha = \frac{2\omega_i\omega_j\zeta}{\omega_i + \omega_j} \quad (14)$$

$$\beta = \frac{2\zeta}{\omega_i + \omega_j} \quad (15)$$

Where: ζ = damping ratio

First five modes of the natural frequencies were used for the computations of the mass and stiffness coefficients using equation (14) and (15). The damping ratio for modes higher than the fifth will increase monotonically with frequency and corresponding model responses will be essentially eliminated because of their high damping [21]. The damping ratios were assumed to be 5% and 2% for the empty and liquid filled tanks respectively, which are based on the recommended damping values [22].

Example calculation for Model 1 empty tank:

$$\alpha = \frac{2\omega_i\omega_j\zeta}{\omega_i + \omega_j} = \frac{2(11.495)(14.728)(0.05)}{11.495 + 14.728} = 0.6456$$

$$\beta = \frac{2\zeta}{\omega_i + \omega_j} \frac{(2)(0.05)}{11.495 + 14.728} = 3.81344\text{E-}03$$

Table 18. Mass and stiffness coefficients for the empty tanks models

Model	Mass Coefficient (α)	Stiffness Coefficient (β)
1	6.456E-01	3.813E-03
2	5.201E-01	4.751E-03
3	4.414E-01	5.627E-03
4	2.834E-01	8.463E-03
5	2.300E-01	1.405E-02
6	1.975E-01	1.239E-02
7	2.389E-01	9.544E-03
8	1.885E-01	1.272E-02
9	1.611E-01	1.782E-02
10	1.822E-01	1.242E-02
11	1.442E-01	1.607E-02
12	1.262E-01	1.827E-02

Table 19. Mass and stiffness coefficients for the 90% liquid filled tanks models

Model	Mass Coefficient (α)	Stiffness Coefficient (β)
1	6.215E-03	5.800E-02
2	6.232E-03	5.789E-02
3	6.249E-03	5.777E-02
4	7.525E-03	4.630E-02
5	7.531E-03	4.625E-02
6	7.537E-03	4.619E-02
7	1.178E-02	3.090E-02
8	1.179E-02	3.086E-02
9	1.180E-02	3.084E-02
10	1.726E-02	2.147E-02
11	1.760E-02	2.106E-02
12	1.799E-02	2.060E-02

6.3 Earthquake Data

Two different earthquake data were used in this study which are El Centro of May 18, 1940 and Parkfield of September 27, 2004. These earthquakes were chosen because they have different characteristics. The data of El Centro earthquake are from the National Information Service for Earthquake Engineering (NISEE), University of California at Berkeley, and the data of Parkfield earthquake are from the Center for Engineering Strong Motion Data, produced by the USGS and cooperating networks. Numerical values of these earthquakes are in units of g, the acceleration due to gravity are presented in Figure 49 and Figure 50.

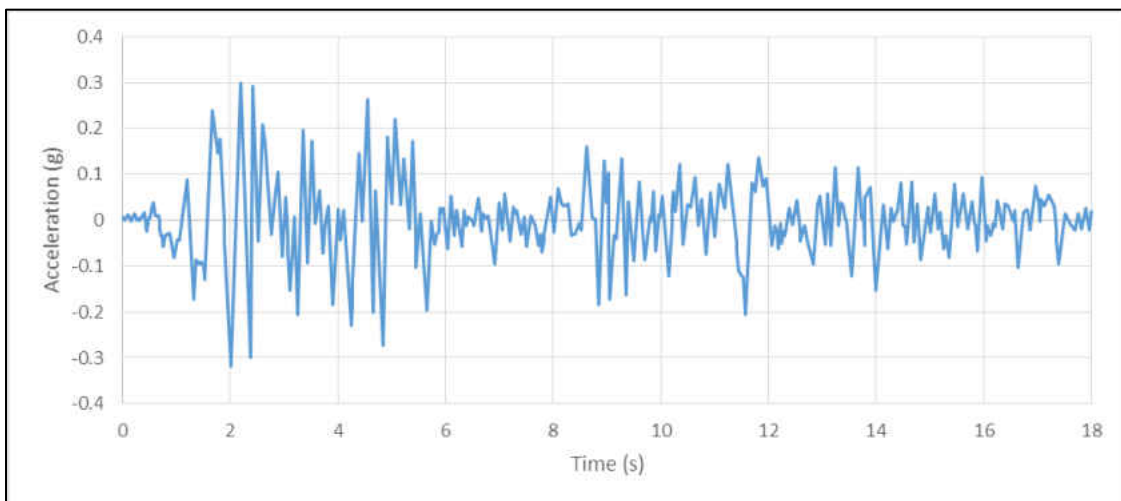


Figure 50. Accelerogram of North-South component of El Centro earthquake, 1940

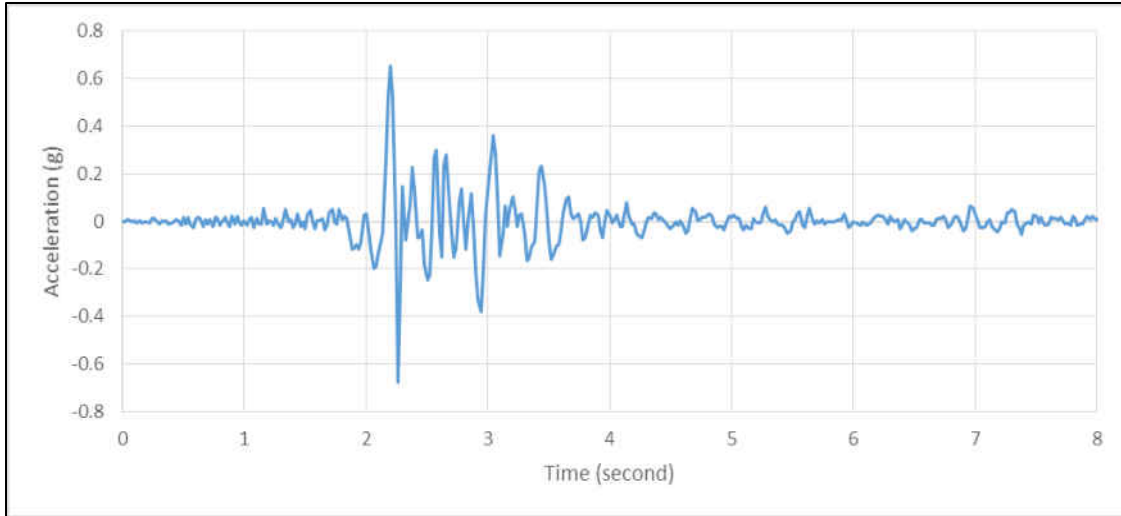


Figure 51. Accelerogram of North-South component of Parkfield earthquake, 2004

Base excitation cannot be directly included in the transient analysis with ANSYS computer program. To apply earthquake loads in terms of acceleration at the base, the elements at base of the cylindrical tanks has to be selected to create a selection component, and the earthquake loads are created in text file. The accelerations from the created text file can be applied to the elements using commands (APDL). The commands (APDL) that are used for the based excitations are “*dim”, “*tread”, and “cmacel”. These commands are used to create the table name, to read the table from a text file, and to apply tabular acceleration, respectively.

6.4 Results

Budiansky and Roth procedure [20] was used to find the dynamic buckling load for both empty and tanks filled with water up to 90% of their height. Both El Centro and Parkfield earthquakes were applied to each model. The maximum displacements were plotted in as function of PGA level. These curves have been identified as a pseudo

equilibrium paths. The pseudo equilibrium path is suitable to investigate the dynamic buckling along the path of transient displacements.

6.4.1 Empty Cylindrical Tanks Subjected to the El Centro Earthquake

The first 8.00 seconds of the El Centro earthquake record were used. As shown in Figure 50, the maximum amplitude of the El Centro earthquake is within the first eight seconds. As results of the empty cylindrical tanks subjected to the El Centro Earthquake show in Table 20, it was found that the critical PGA values for the empty cylindrical tanks are very high. These PGA values are unrealistic for the past real world earthquakes.

It was found that von-Mises stresses for all models are less than the yield stress of the steel which is 50,000 psi (344.74 MPa). The highest von-Mises stress at the critical PGA value occurred with Model 1 at 12,050 psi (83.08 MPa). Thus, for the empty cylindrical tanks subjected to the El Centro earthquake, the buckling that occurred in all models is elastic buckling. The maximum Von-Mises stresses occurred just above the support for every model; however, the maximum displacement occurred at the top of the cylindrical tanks.

Table 20. Dynamic Buckling Points of Empty Tanks subjected to the El Centro Earthquake, 1940

H/D	PGA (g)		
	D/t=1000	D/t=1500	D/t=2000
0.5	42	28	20
1.0	35	22	15
1.5	32	18	12
2.0	29	17	11

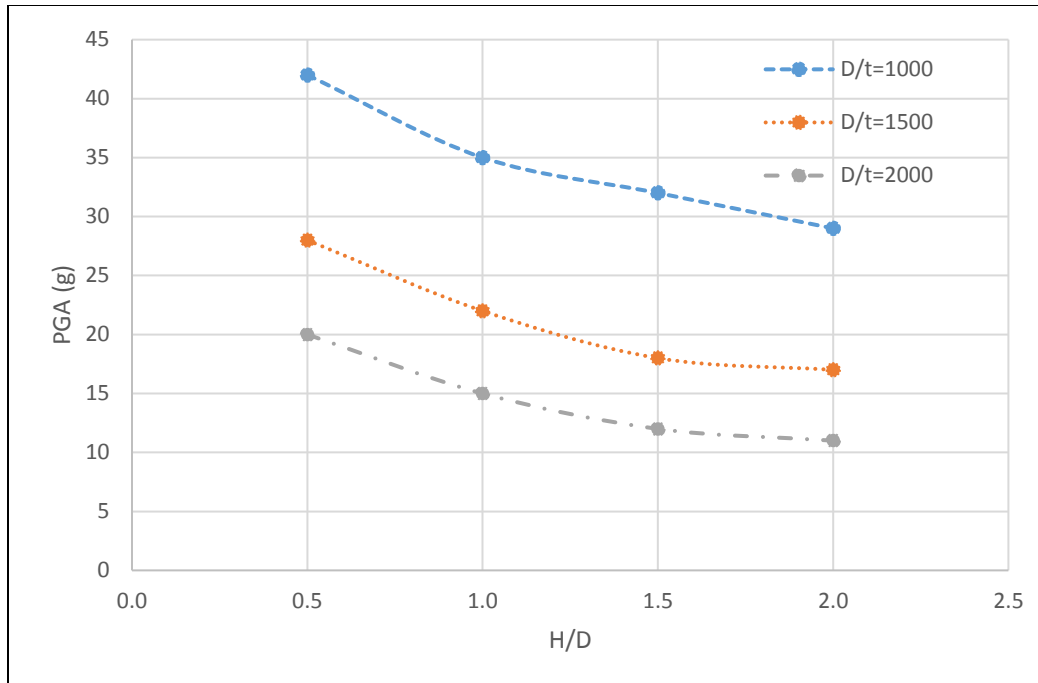


Figure 52. Plots of dynamic buckling capacities in terms of acceleration from transient analysis of empty tanks subjected to the El Centro earthquake, 1940

Model 1

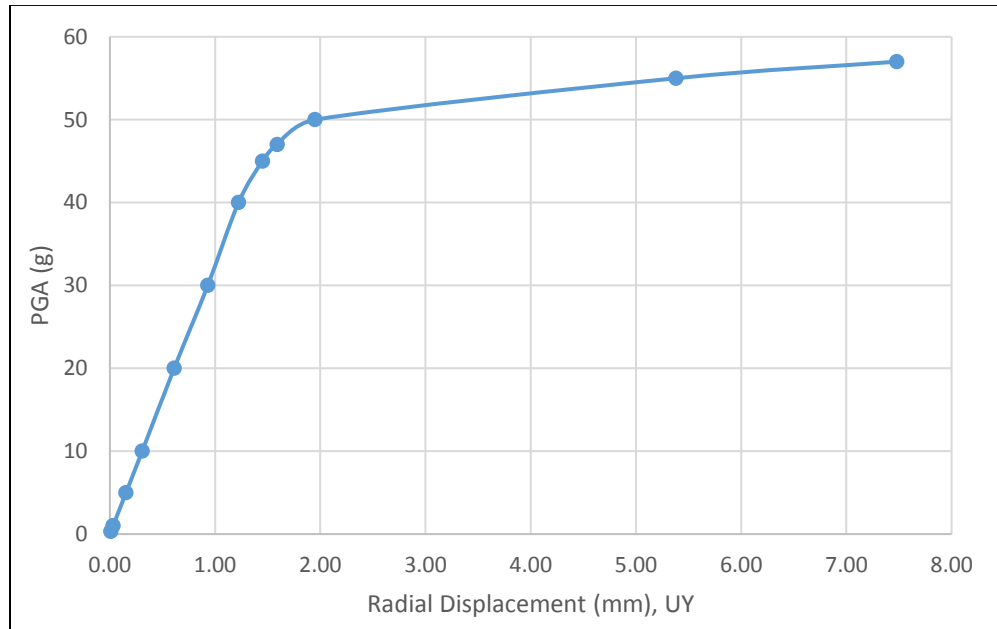


Figure 53. Pseudo equilibrium paths for the critical node of Model 1

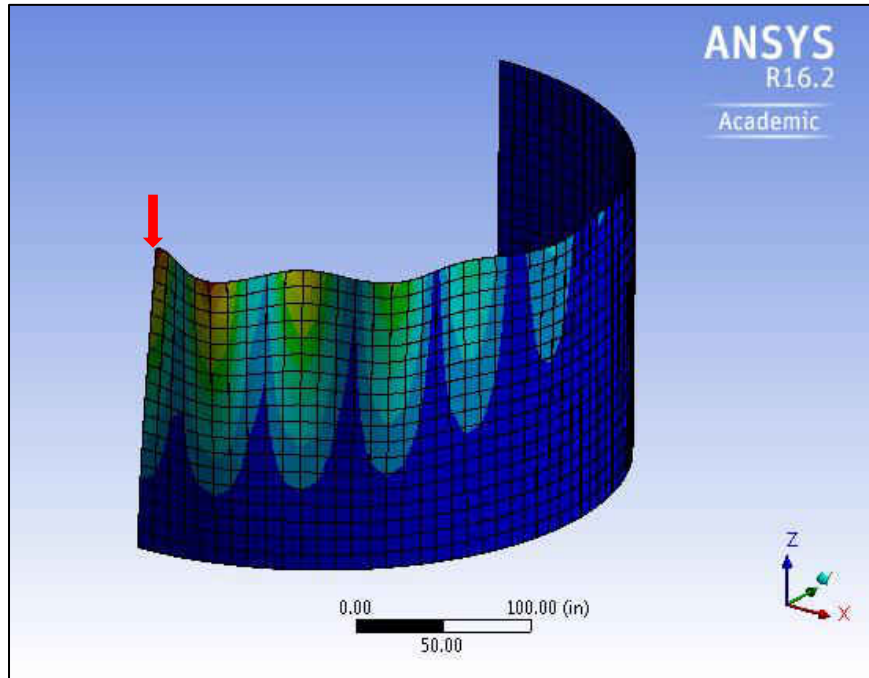


Figure 54. Deformation shape of Model 1 for PGA = 55g

Model 2

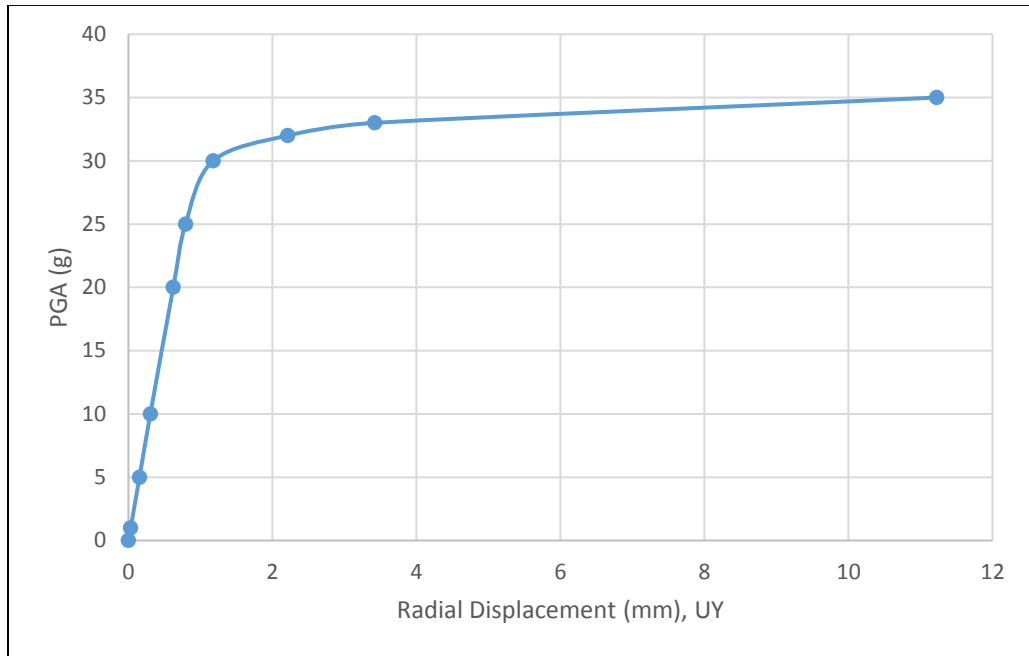


Figure 55. Pseudo equilibrium paths for the critical node of Model 2

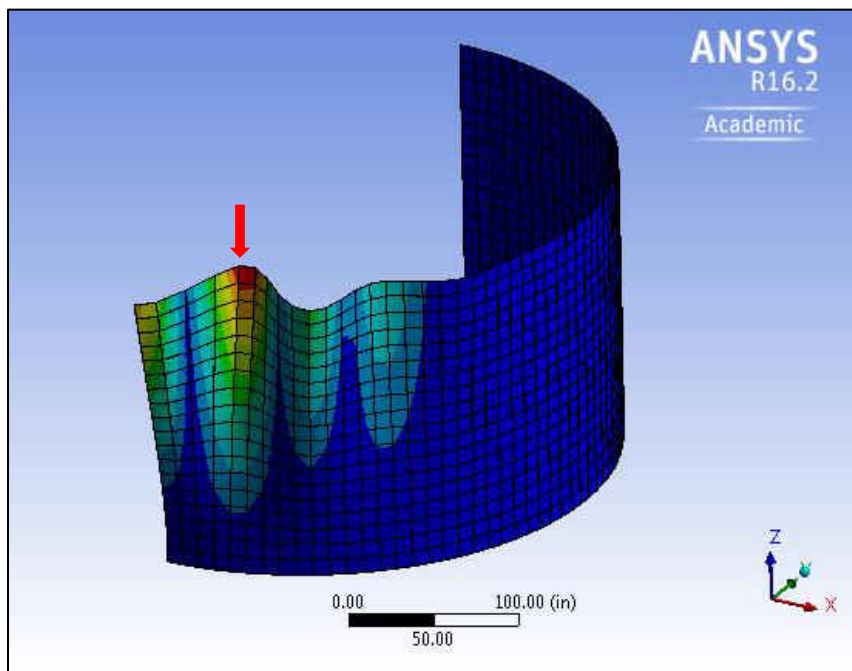


Figure 56. Deformation shape of Model 2 for PGA = 33g

Model 3

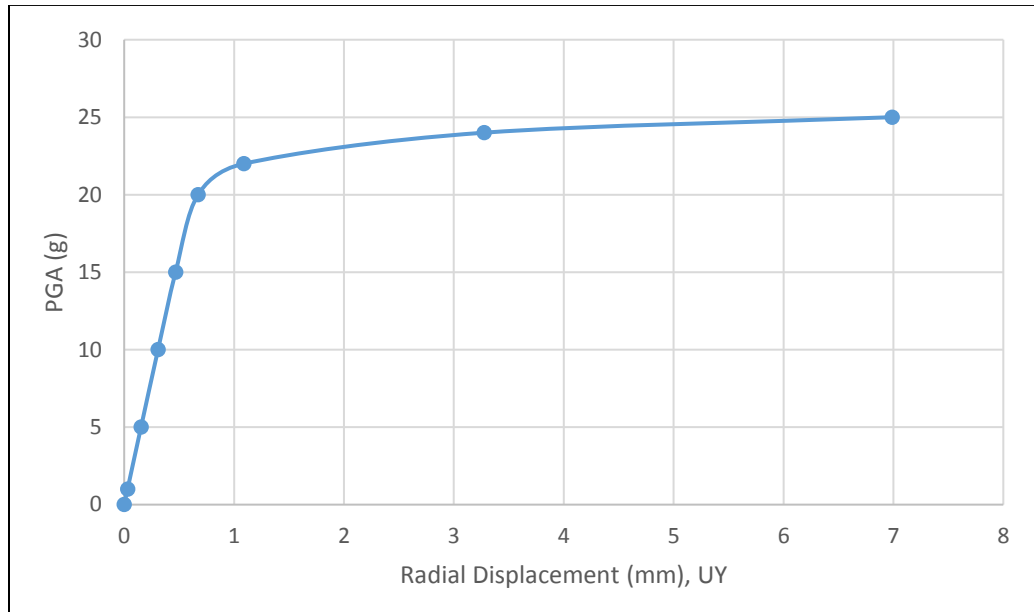


Figure 57. Pseudo equilibrium paths for the critical node of Model 3

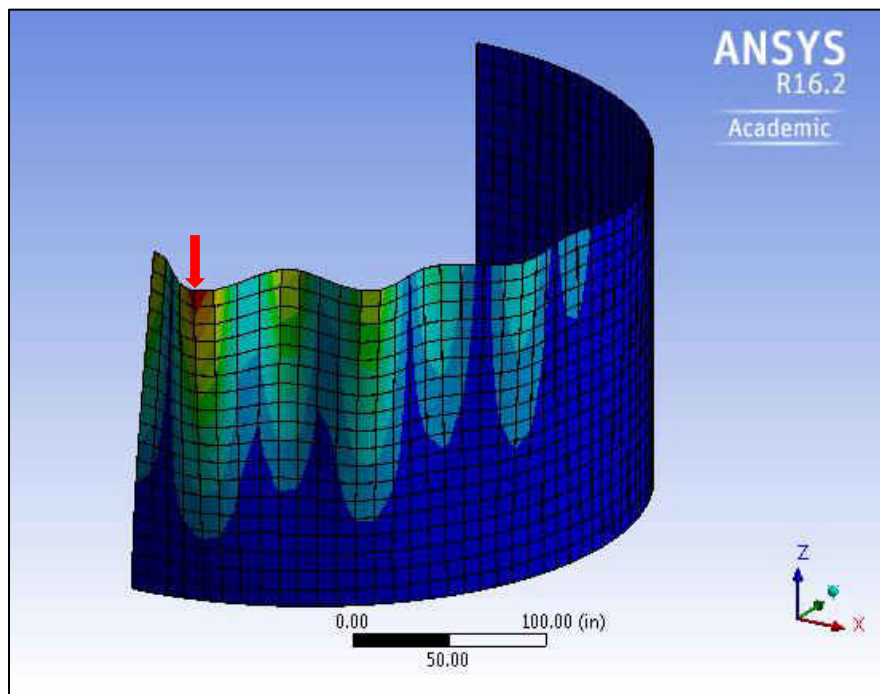


Figure 58. Deformation shape of Model 3 for PGA = 24g

Model 4

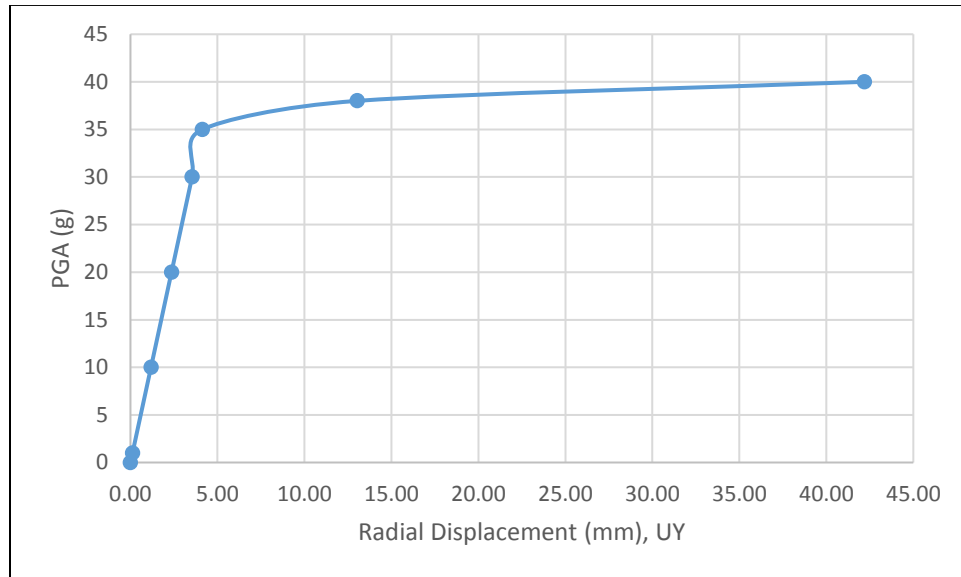


Figure 59. Pseudo equilibrium paths for the critical node of Model 4

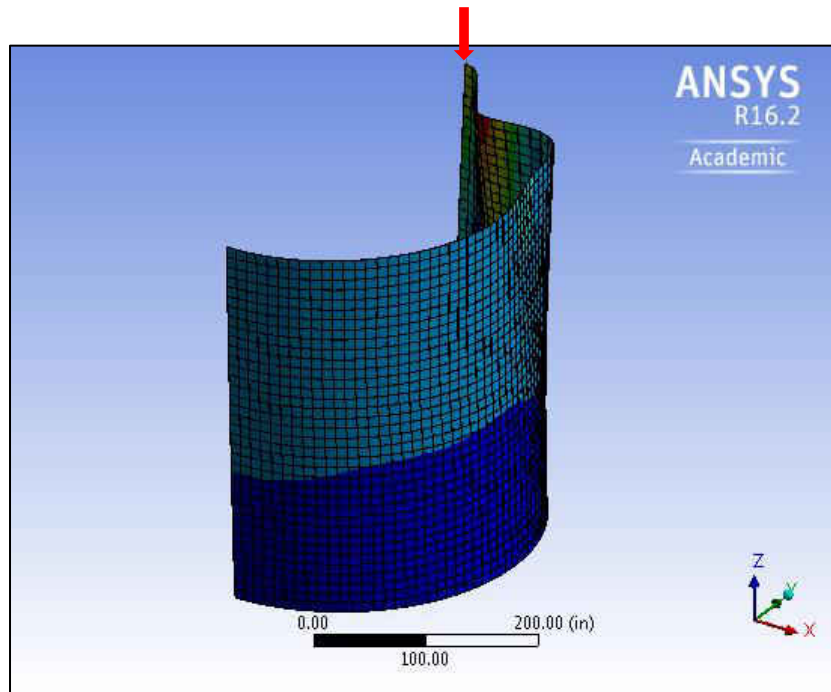


Figure 60. Deformation shape of Model 4 for PGA = 38g

Model 5

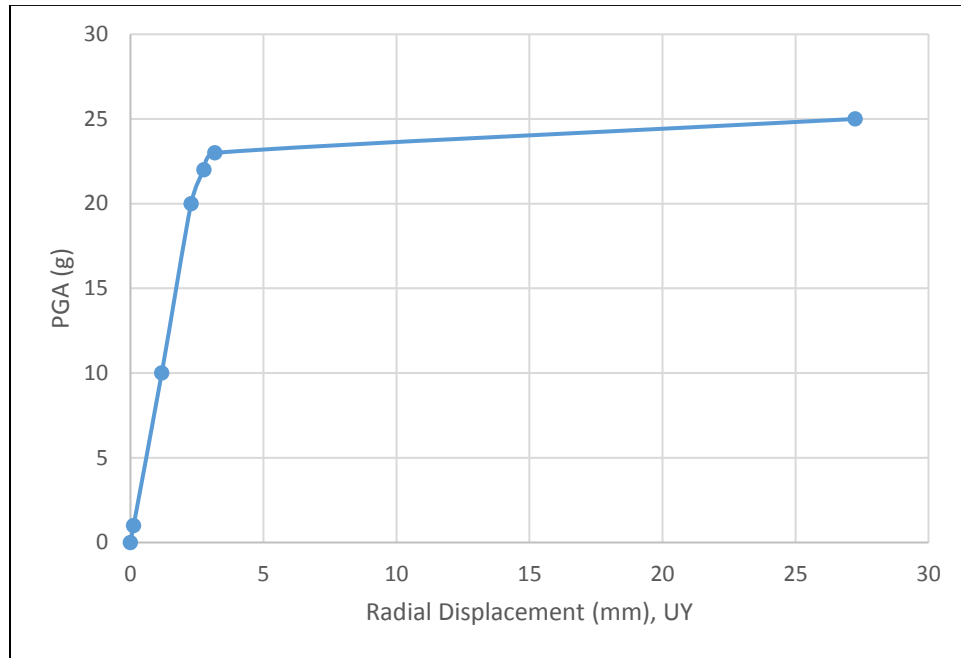


Figure 61. Pseudo equilibrium paths for the critical node of Model 5

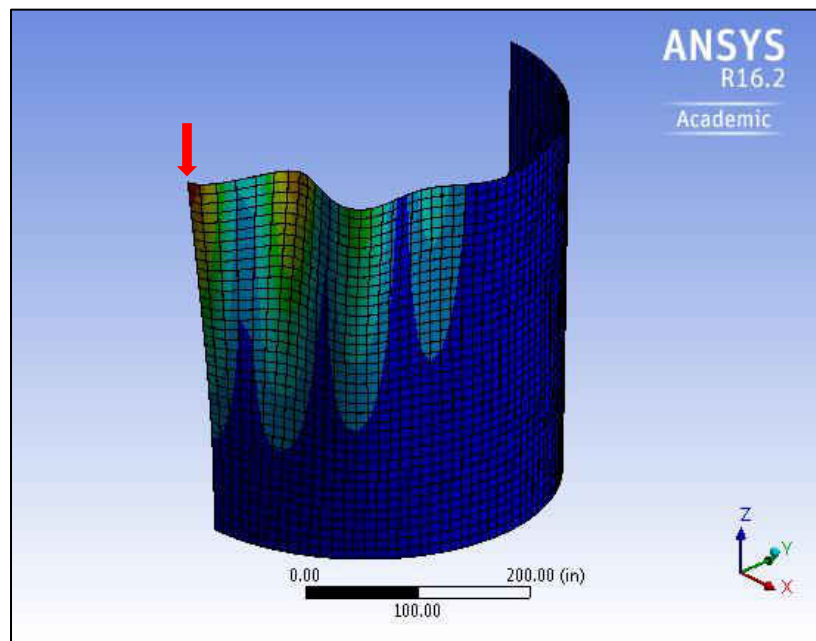


Figure 62. Deformation shape of Model 5 for PGA = 25g

Model 6

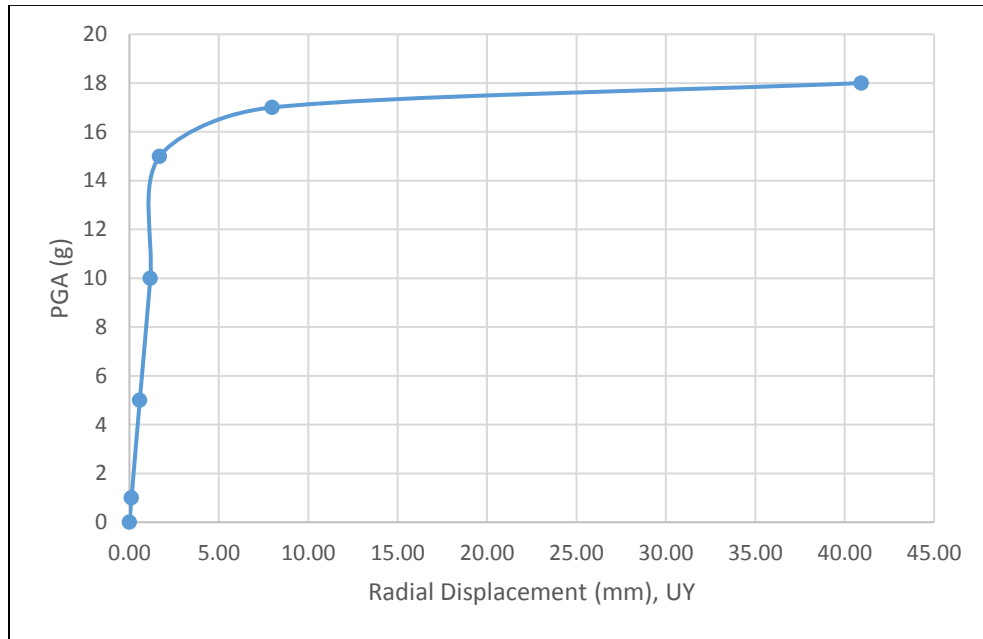


Figure 63. Pseudo equilibrium paths for the critical node of Model 6

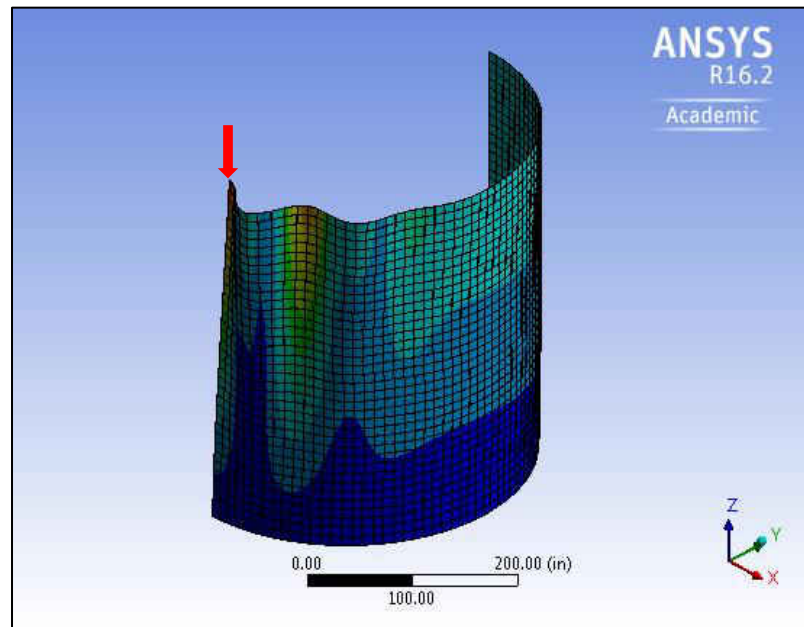


Figure 64. Deformation shape of Model 6 for PGA = 17g

Model 7

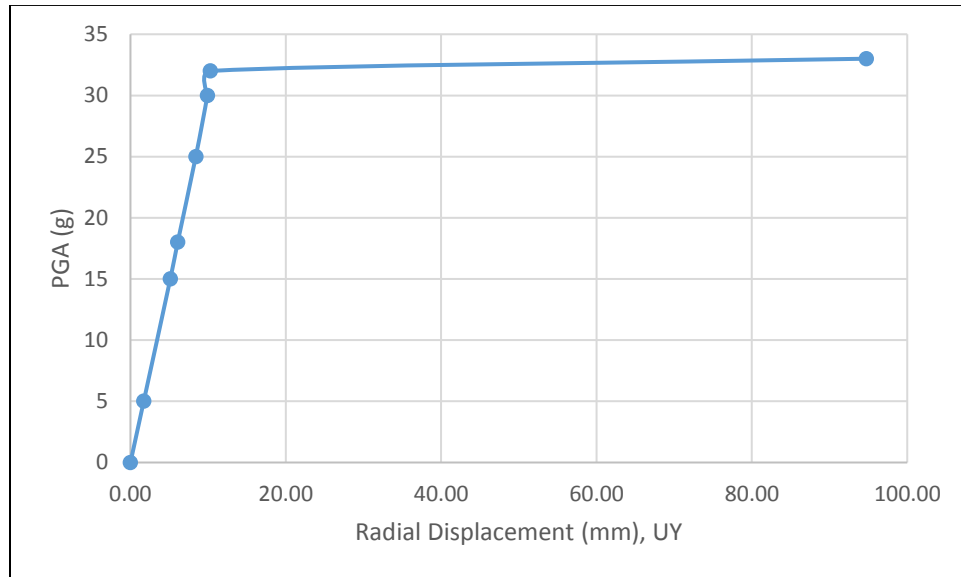


Figure 65. Pseudo equilibrium paths for the critical node of Model 7

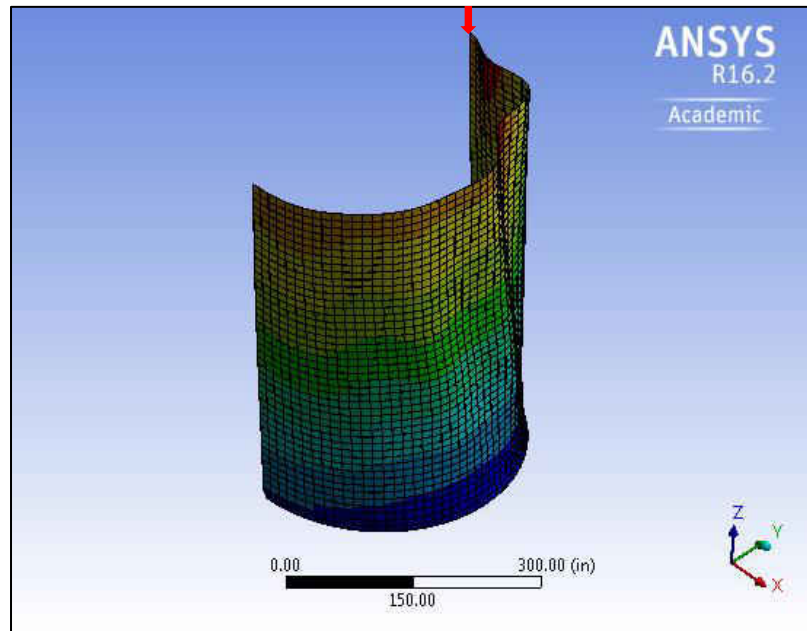


Figure 66. Deformation shape of Model 7 for PGA = 33g

Model 8

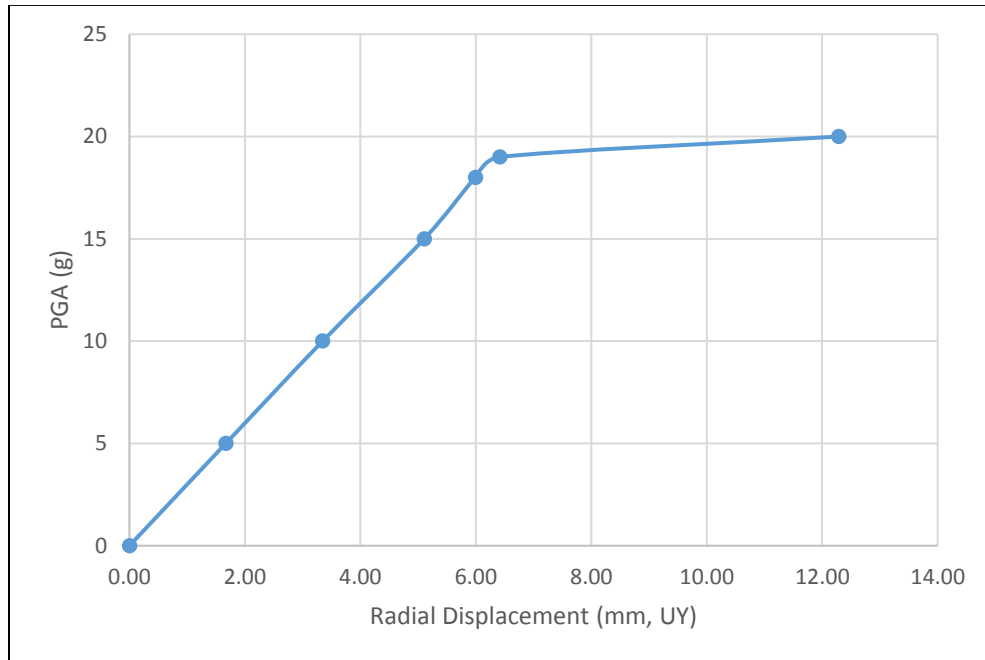


Figure 67. Pseudo equilibrium paths for the critical node of Model 8

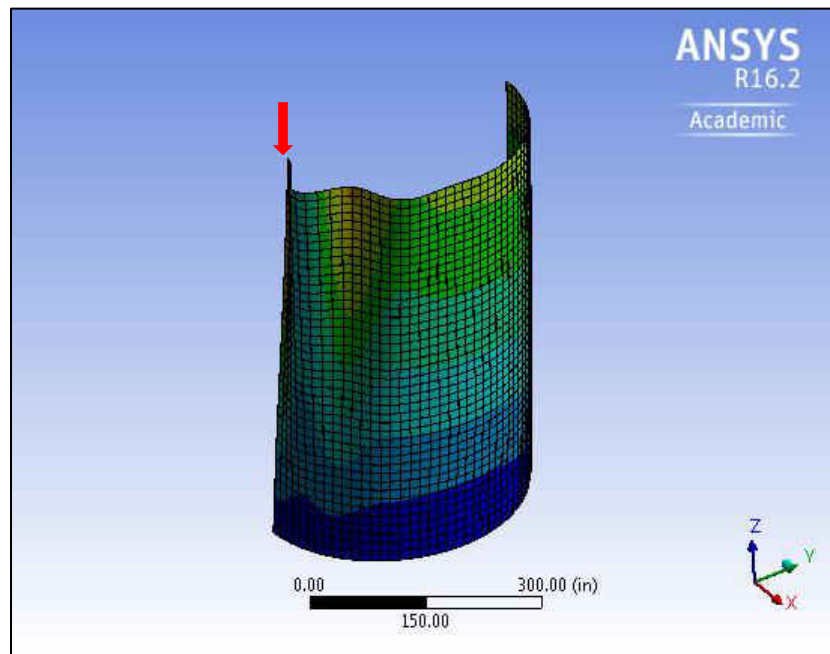


Figure 68. Deformation shape of Model 8 for PGA = 20g

Model 9

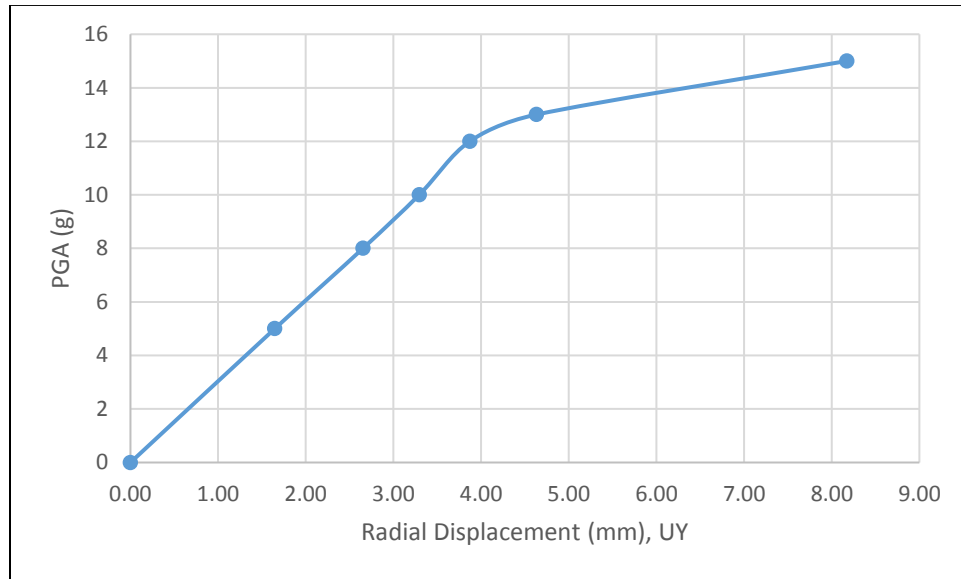


Figure 69. Pseudo equilibrium paths for the critical node of Model 9

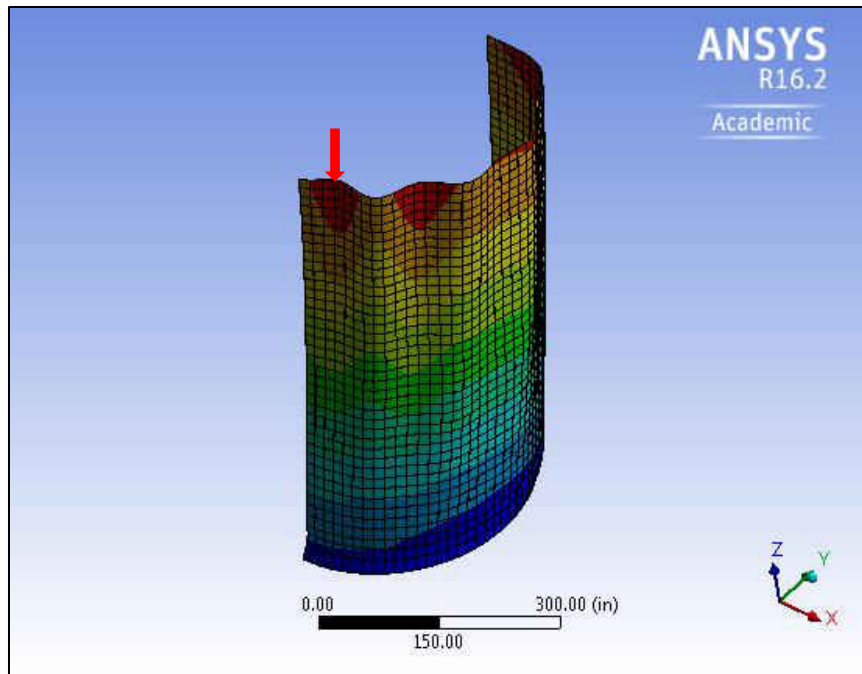


Figure 70. Deformation shape of Model 9 for PGA = 15g

Model 10

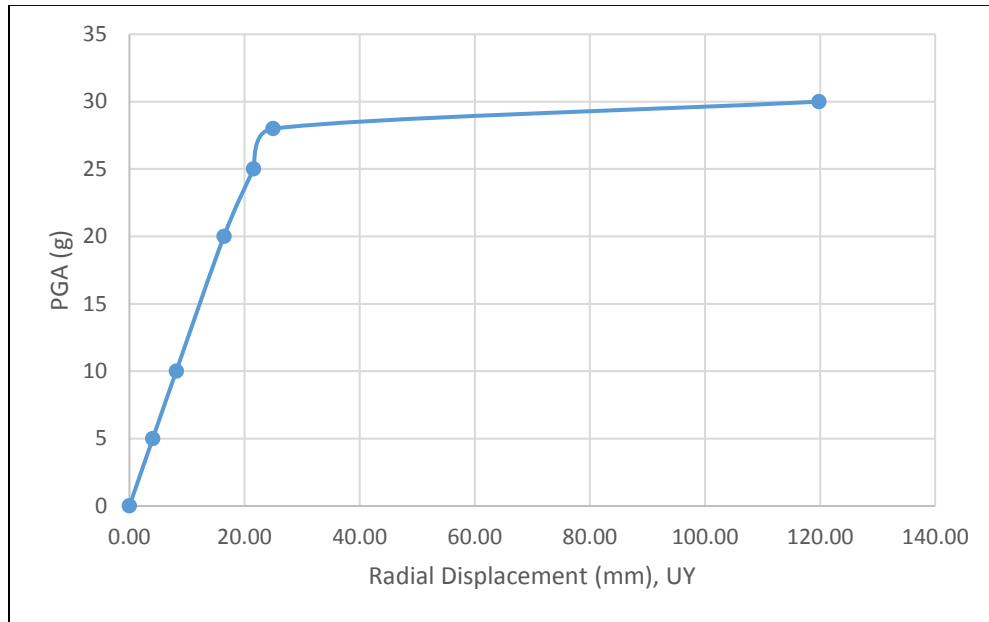


Figure 71. Pseudo equilibrium paths for the critical node of Model 10

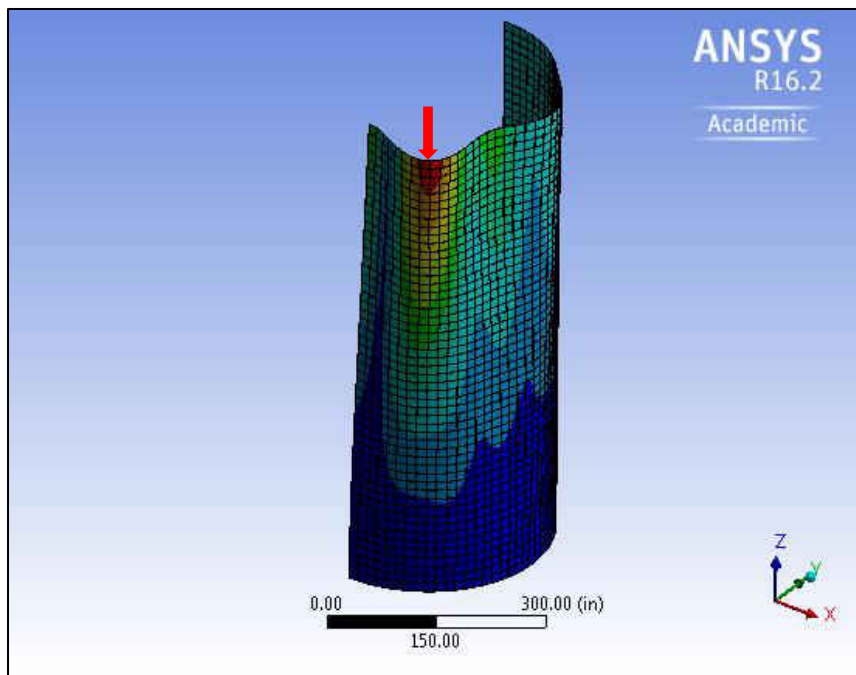


Figure 72. Deformation shape of Model 10 for PGA = 30g

Model 11

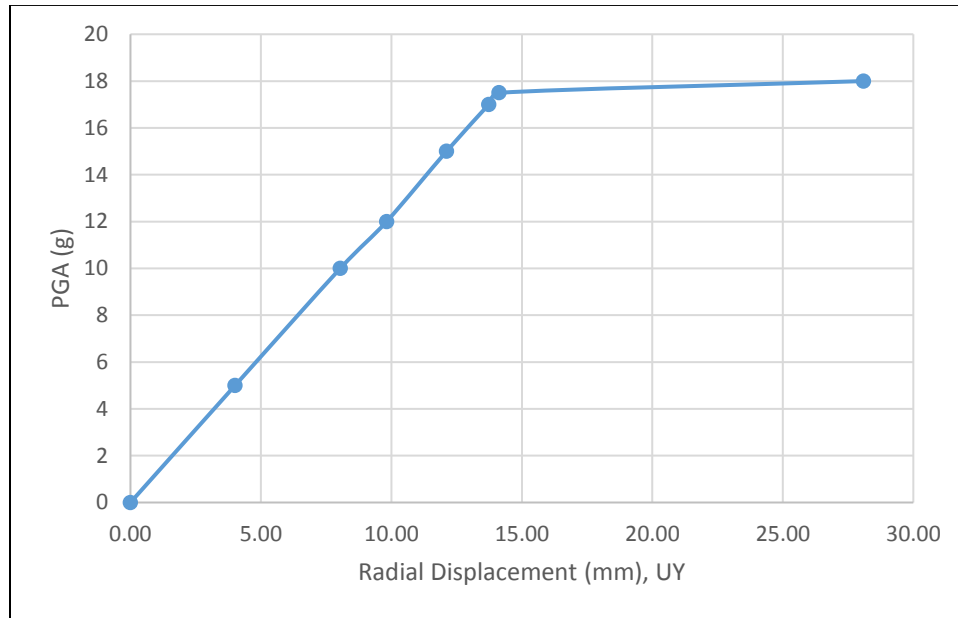


Figure 73. Pseudo equilibrium paths for the critical node of Model 11

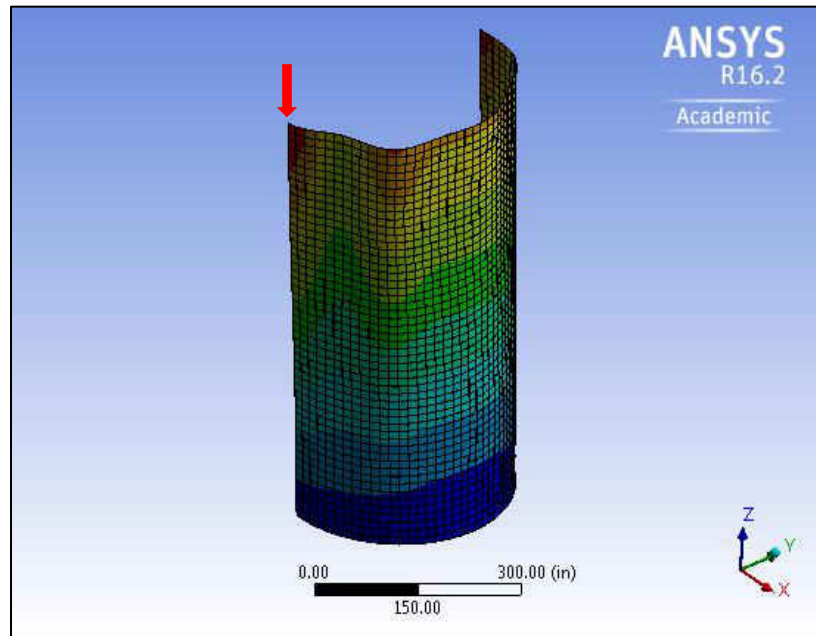


Figure 74. Deformation shape of Model 11 for PGA = 18g

Model 12

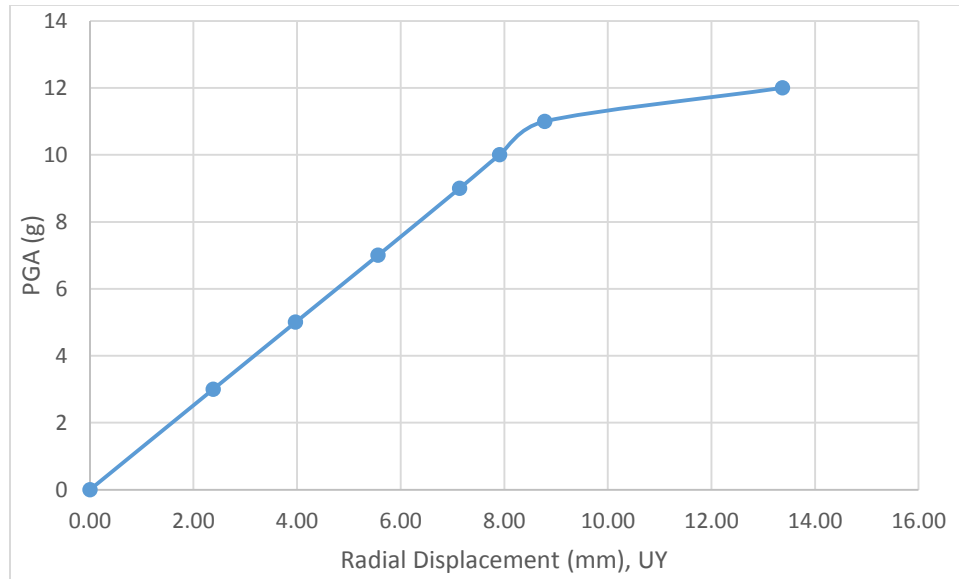


Figure 75. Pseudo equilibrium paths for the critical node of Model 12

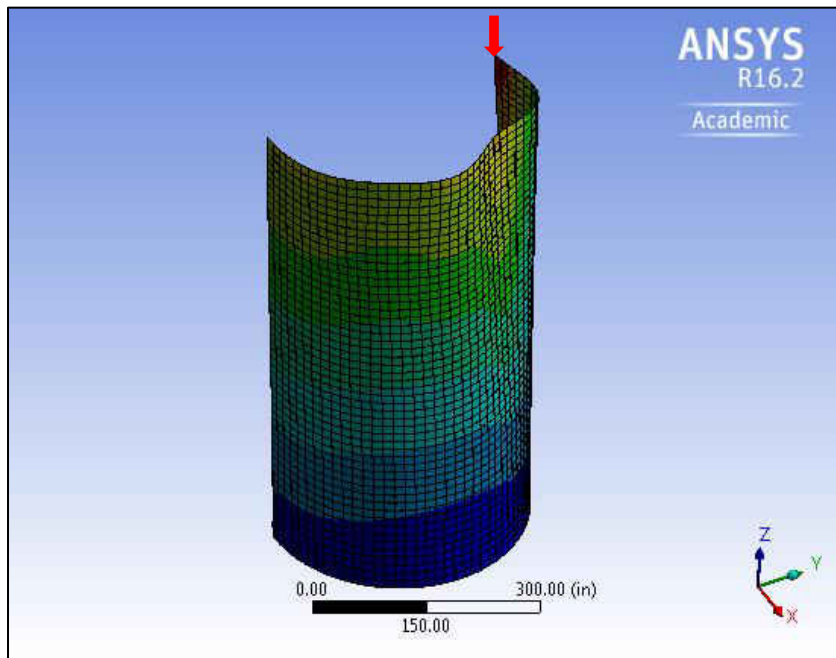


Figure 76. Deformation shape of Model 12 for PGA = 12g

6.4.2 Cylindrical Tanks Filled with Water up to 90% of Height Subjected to the El Centro Earthquake

The dynamic buckling loads of the cylindrical tanks were analyzed with the transient analysis when they were containing water up to 90% depth of their height. The El Centro earthquake accelerogram with the PGA of 0.319g was the applied load. The characteristic of El Centro earthquake is illustrated in Figure 50. The critical PGA values for the cylindrical tanks filled with water up to 90% of their height are significantly smaller than the empty cylindrical tanks. The buckling point of model 9 and model 12 are 0.30g and 0.25g respectively. These buckling points are less than 0.319g which is the PGA of El Centro earthquake; therefore, based on this study, the shell dynamic buckling occurs for model 9 and model 12 when they are subjected to the El Centro earthquake.

As stated in chapter 1, this study is interested in the failure of the shell buckling mode subjected to the horizontal earthquake accelerations. In addition, the imperfection was not included in this study. The critical PGA values are expected to reduce for all models if the imperfection is included.

For von-Mises stresses at the dynamic buckling loads, it was found that Von-Mises stresses for all models are less than the yield stress of the steel which is 50,000 psi (344.74 MPa). The highest von-Mises stress occurred with Model 12 at 37,100 psi (255.80 MPa).

Table 21. Dynamic buckling points of tanks filled with water to 90% of their height subjected to the El Centro earthquake, 1940

H/D	PGA (g)		
	D/t=1000	D/t=1500	D/t=2000
0.5	1.20	1.10	0.85
1.0	1.10	0.95	0.75
1.5	0.70	0.60	0.30
2.0	0.60	0.40	0.25

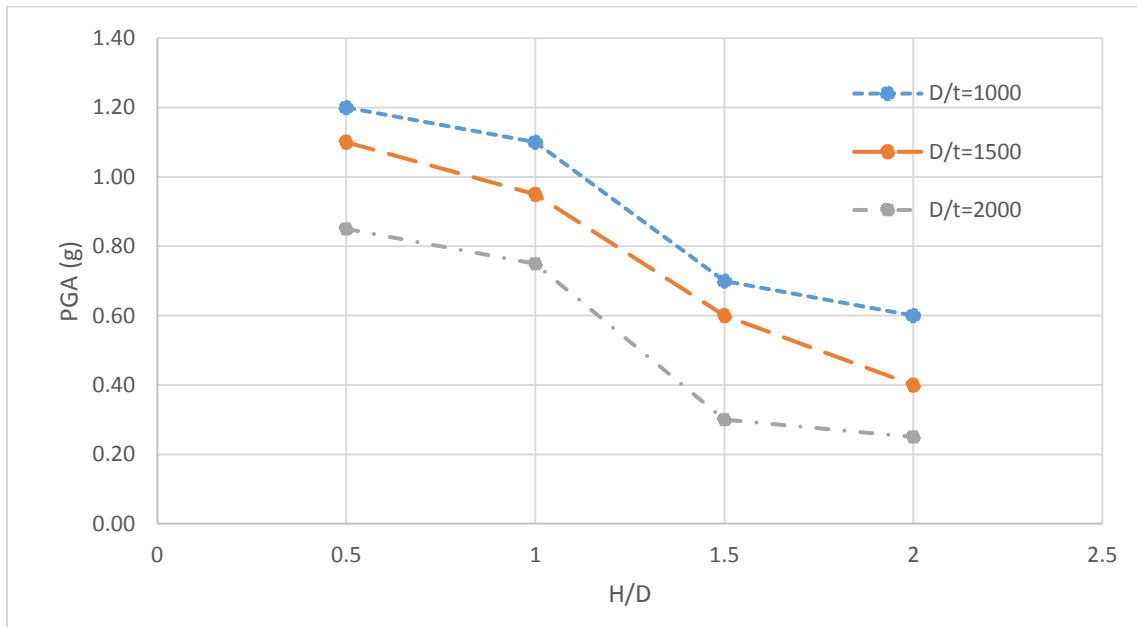


Figure 77. Plots of Nonlinear Transient Buckling Points of Tanks filled with water to 90% of their height subjected to the El Centro Earthquake, 1940

Model 1

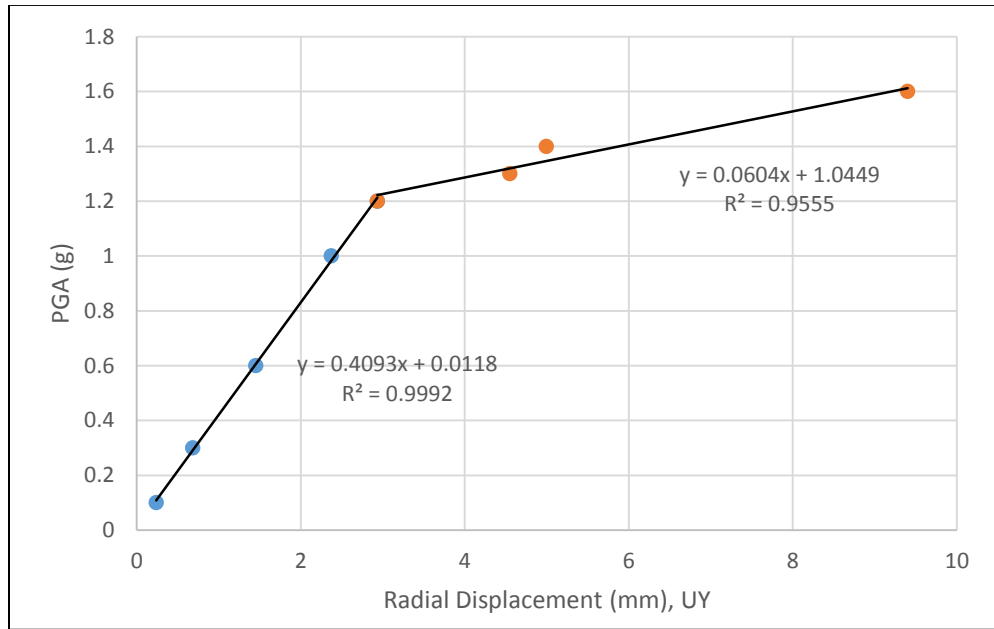
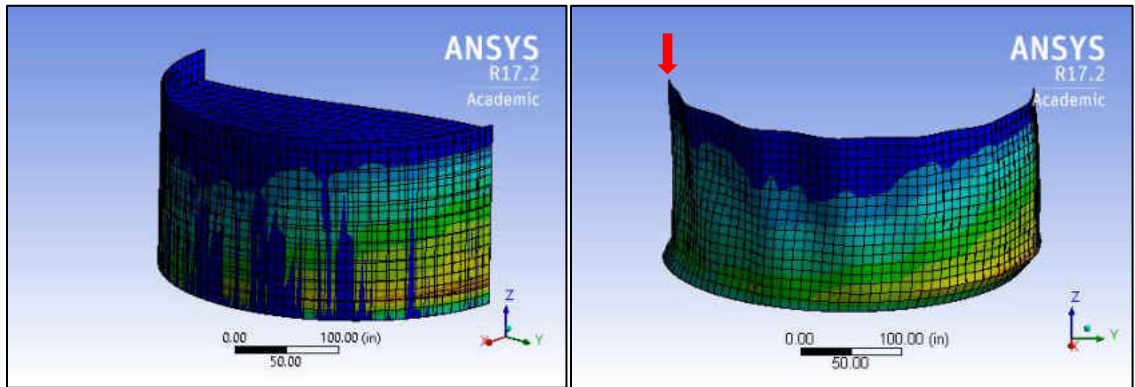


Figure 78. Pseudo equilibrium paths for the critical node of model 1 filled with water to 90% depth



(a) Undeformed shape

(b) Shell deformation

Figure 79. (a) Undeformed shape and (b) Shell deformation of Model 1 filled with water to 90% depth

Model 2

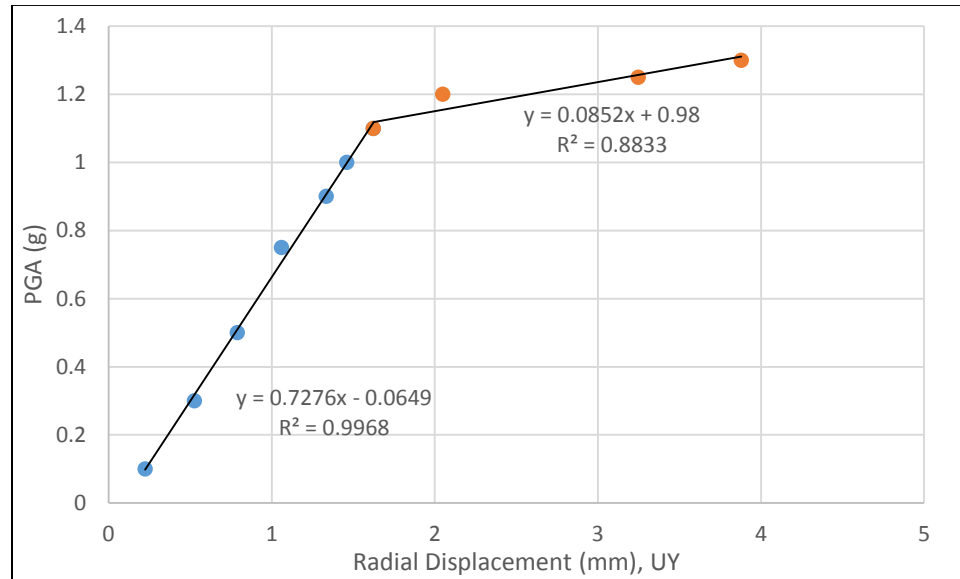


Figure 80. Pseudo equilibrium paths for the critical node of model 2 filled with water to 90% depth

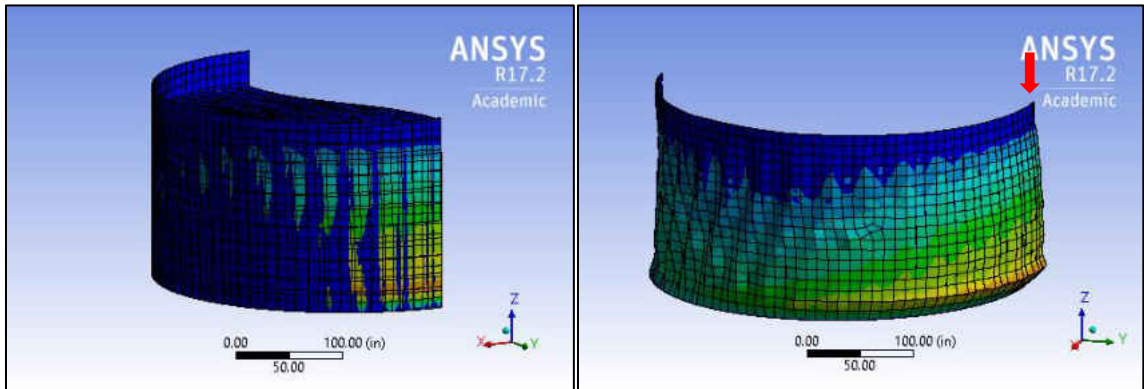


Figure 81. (a) Undeformed shape and (b) Shell deformation of Model 2 filled with water to 90% depth

Model 3

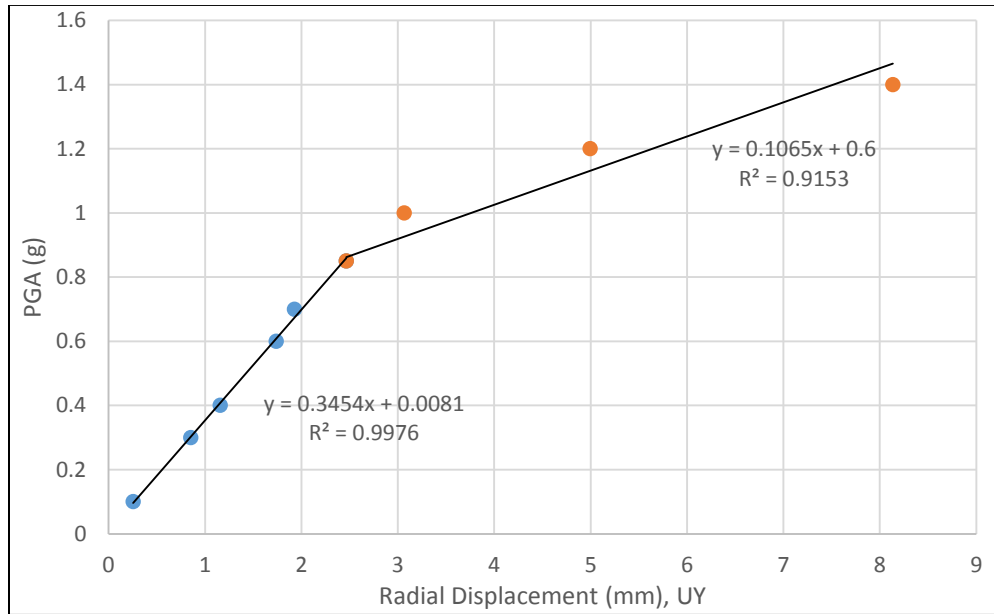
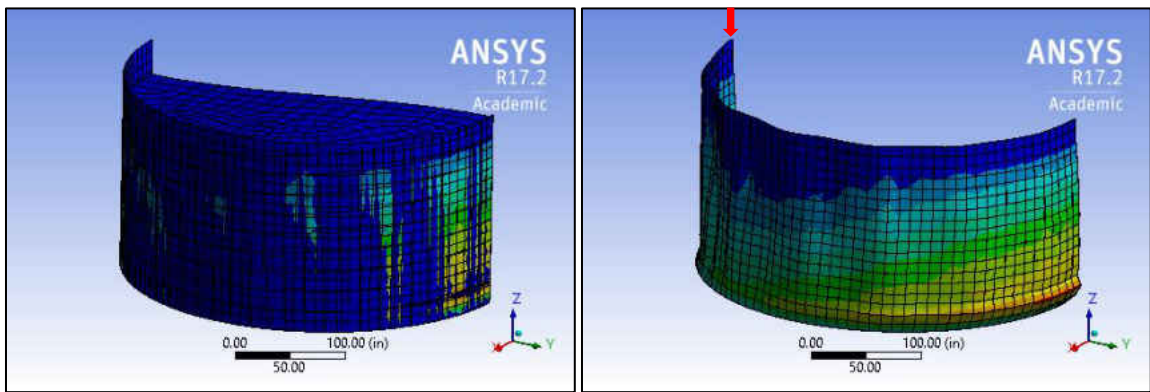


Figure 82. Pseudo equilibrium paths for the critical node of model 3 filled with water to 90% depth



(a) Undeformed shape

(b) Shell deformation

Figure 83. (a) Undeformed shape and (b) Shell deformation of Model 3 filled with water to 90% depth

Model 4

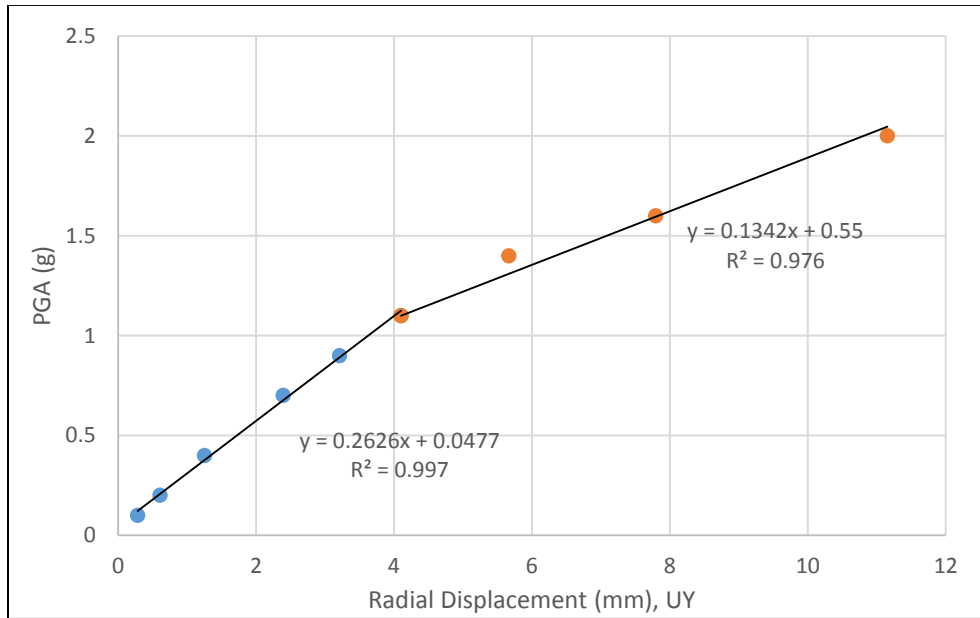
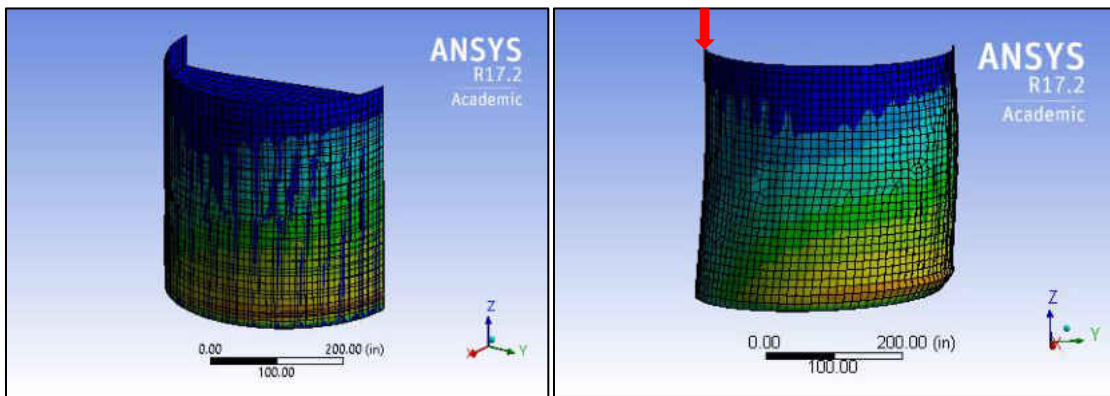


Figure 84. Pseudo equilibrium paths for the critical node of model 4 filled with water to 90% depth



(a) Undeformed shape

(b) Shell deformation

Figure 85. (a) Undeformed shape and (b) Shell deformation of Model 4 filled with water to 90% depth

Model 5

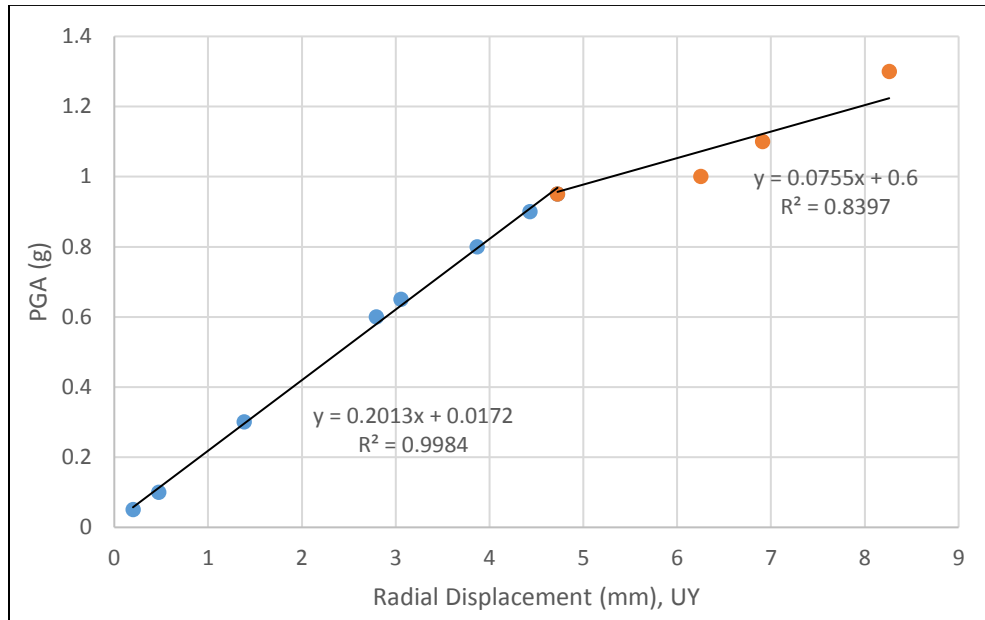
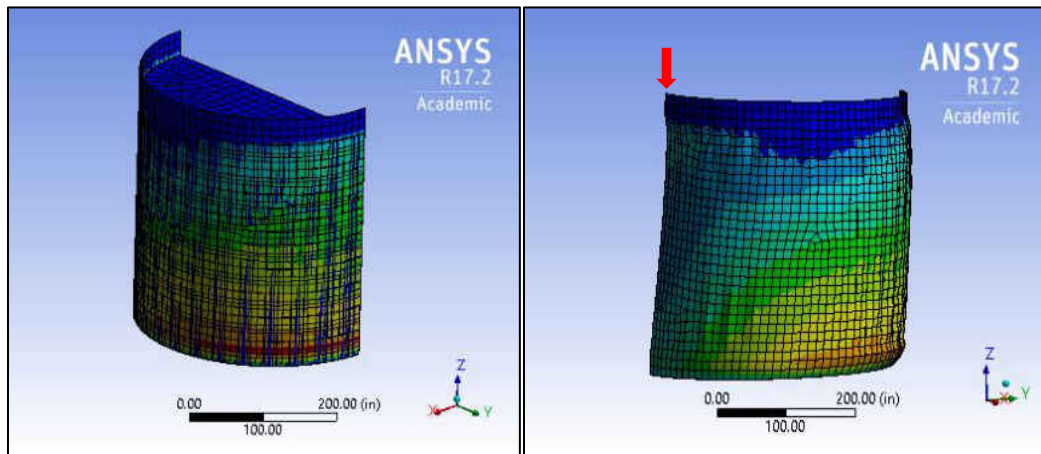


Figure 86. Pseudo equilibrium paths for the critical node of model 5 filled with water to 90% depth



(a) Undeformed shape

(b) Shell deformation

Figure 87. (a) Undeformed shape and (b) Shell deformation of Model 5 filled with water to 90% depth

Model 6

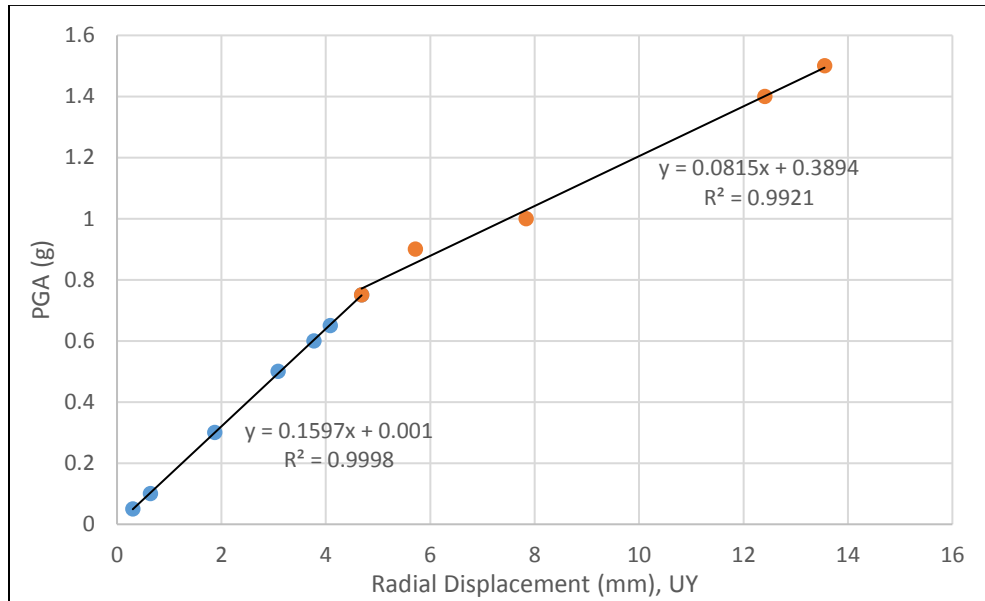
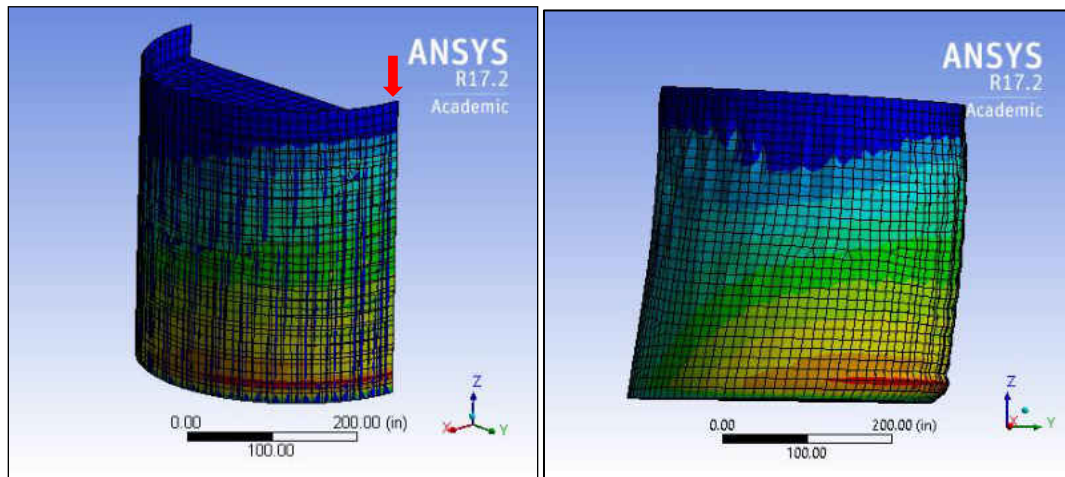


Figure 88. Pseudo equilibrium paths for the critical node of model 6 filled with water to 90% depth



(a) Undeformed shape

(b) Shell deformation

Figure 89. (a) Undeformed shape and (b) Shell deformation of Model 6 filled with water to 90% depth

Model 7

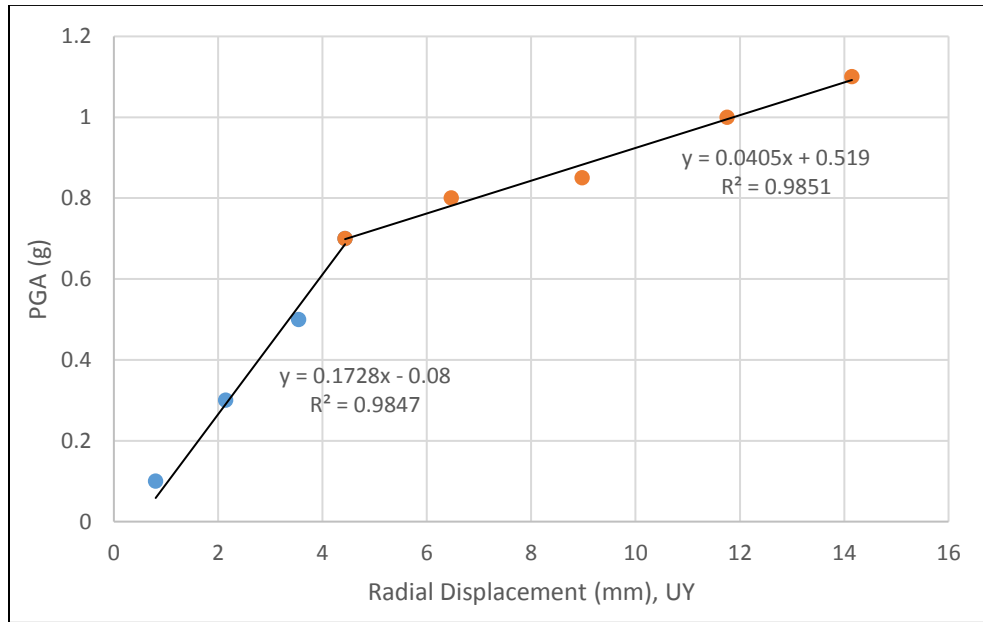


Figure 90. Pseudo equilibrium paths for the critical node of model 7 filled with water to 90% depth

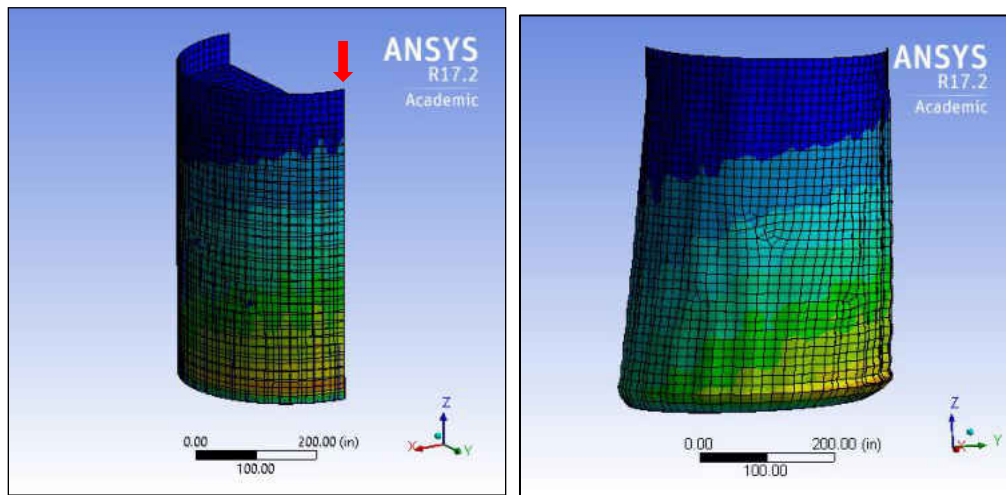


Figure 91. (a) Undeformed shape and (b) Shell deformation of Model 7 filled with water to 90% depth

Model 8

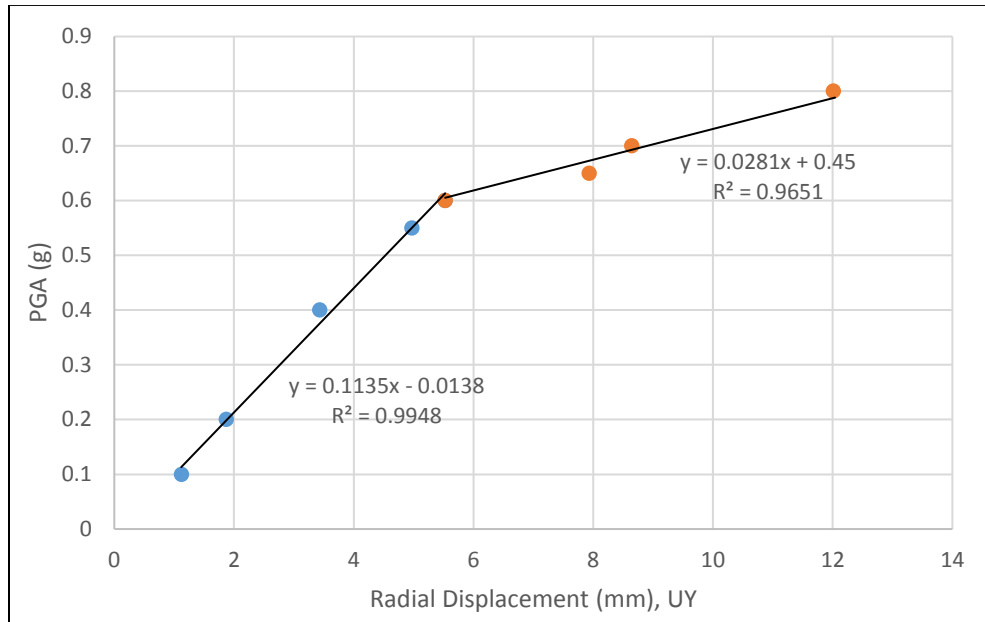


Figure 92. Pseudo equilibrium paths for the critical node of model 8 filled with water to 90% depth

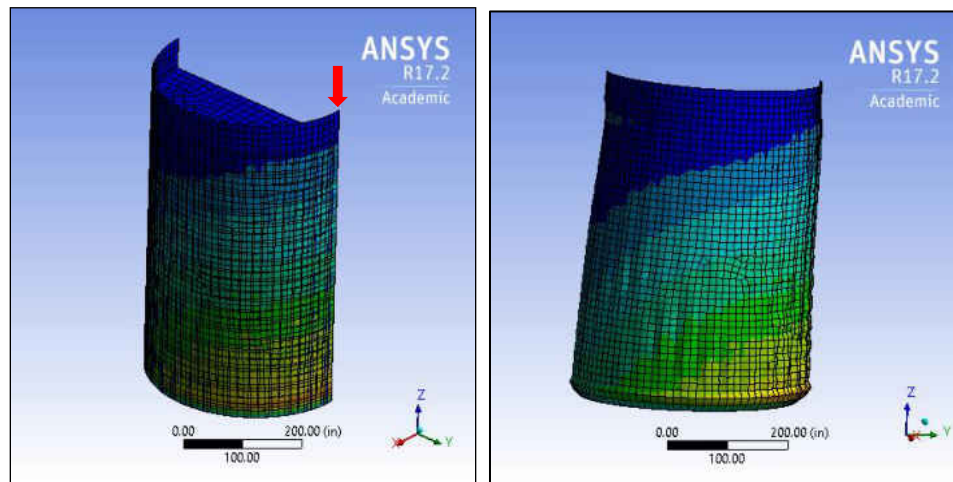


Figure 93. (a) Undeformed shape and (b) Shell deformation of Model 8 filled with water to 90% depth

Model 9

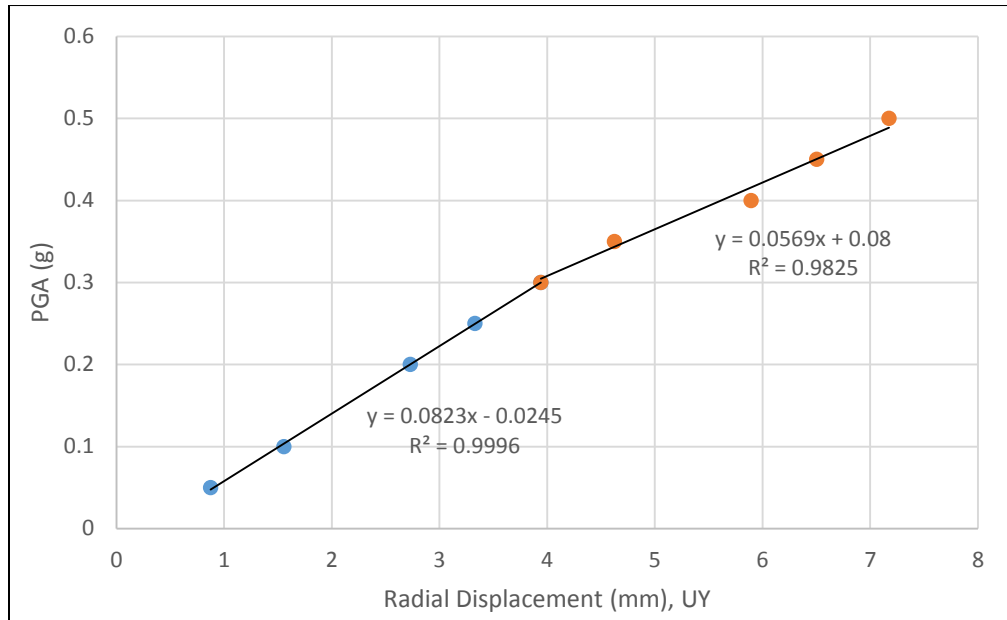
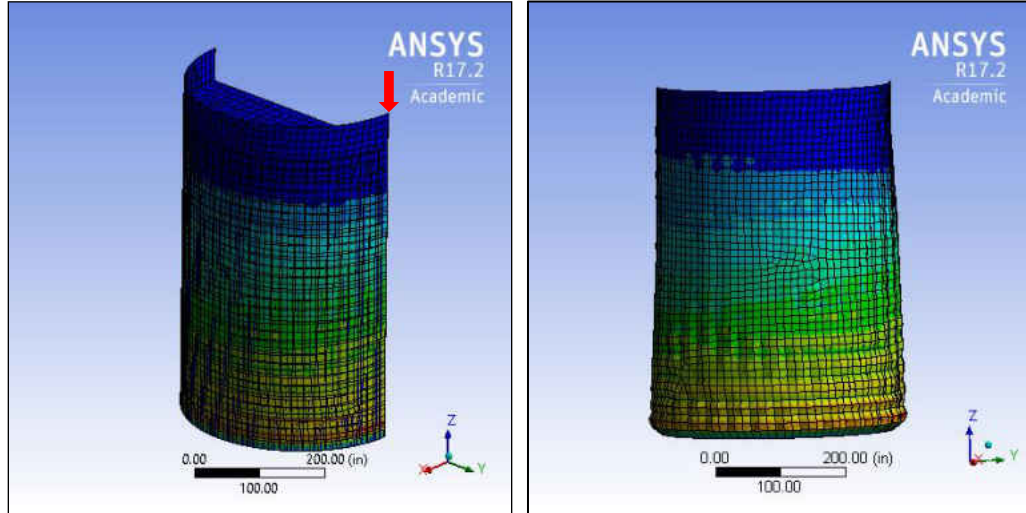


Figure 94. Pseudo equilibrium paths for the critical node of model 9 filled with water to 90% depth



(a) Undeformed shape

(b) Shell deformation

Figure 95. (a) Undeformed shape and (b) Shell deformation of Model 9 filled with water to 90% depth

Model 10

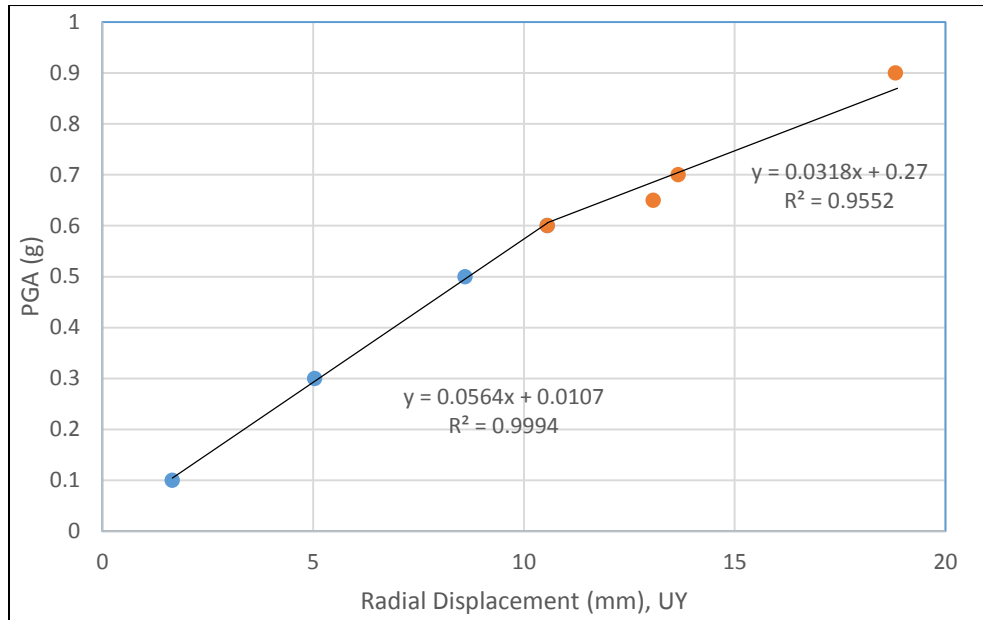


Figure 96. Pseudo equilibrium paths for the critical node of model 10 filled with water to 90% depth

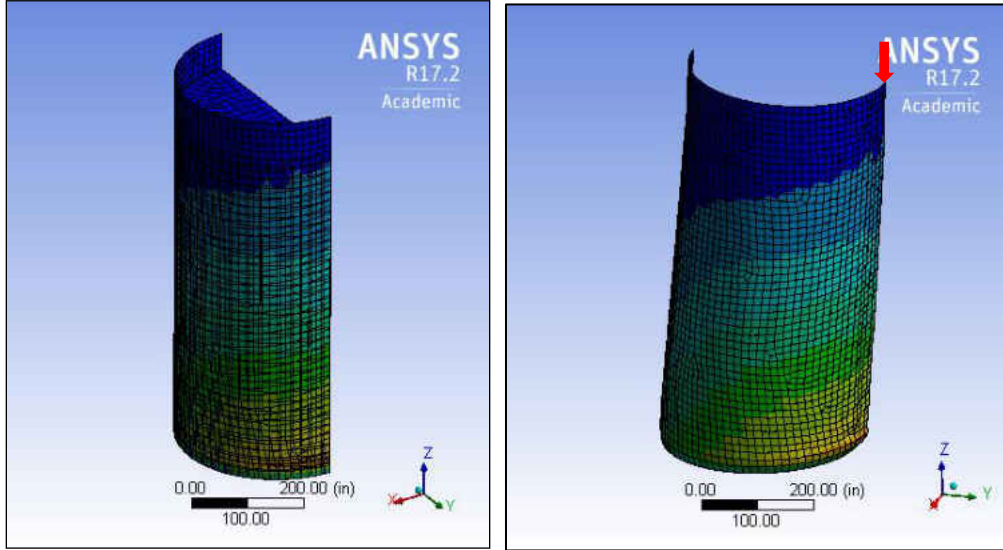


Figure 97. (a) Undeformed shape and (b) Shell deformation of Model 10 filled with water to 90% depth

Model 11

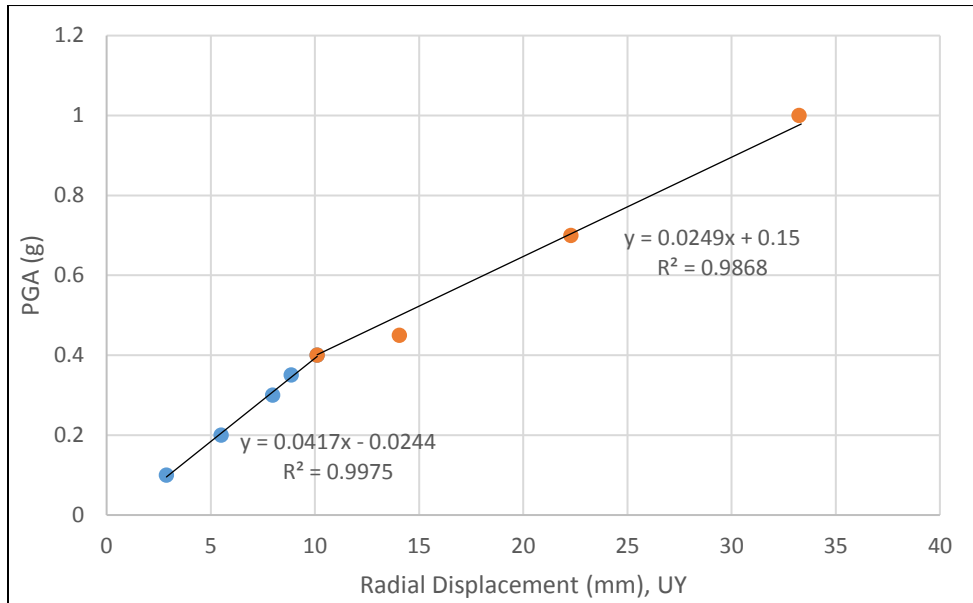
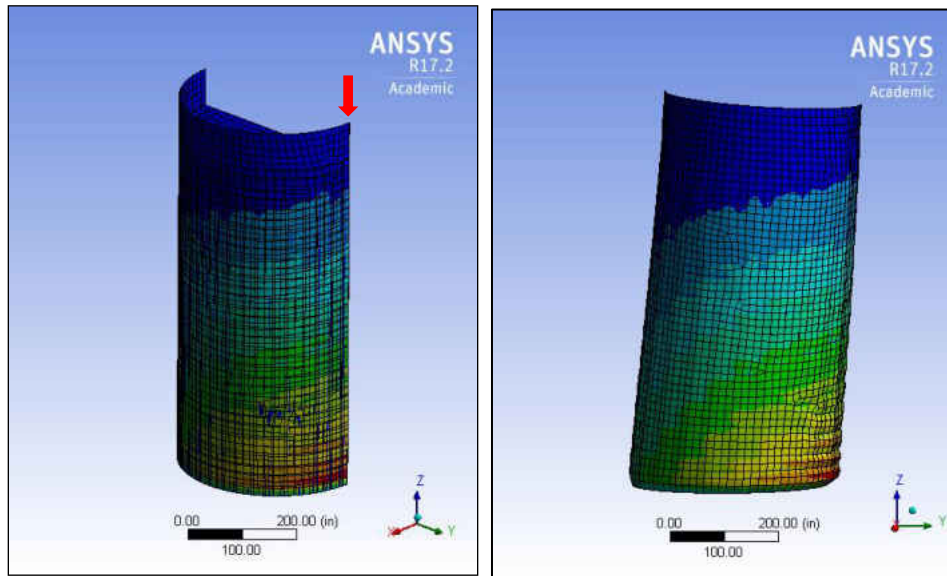


Figure 98. Pseudo equilibrium paths for the critical node of model 11 filled with water to 90% depth



(a) Undeformed shape

(b) Shell deformation

Figure 99. (a) Undeformed shape and (b) Shell deformation of Model 11 filled with water to 90% depth

Model 12

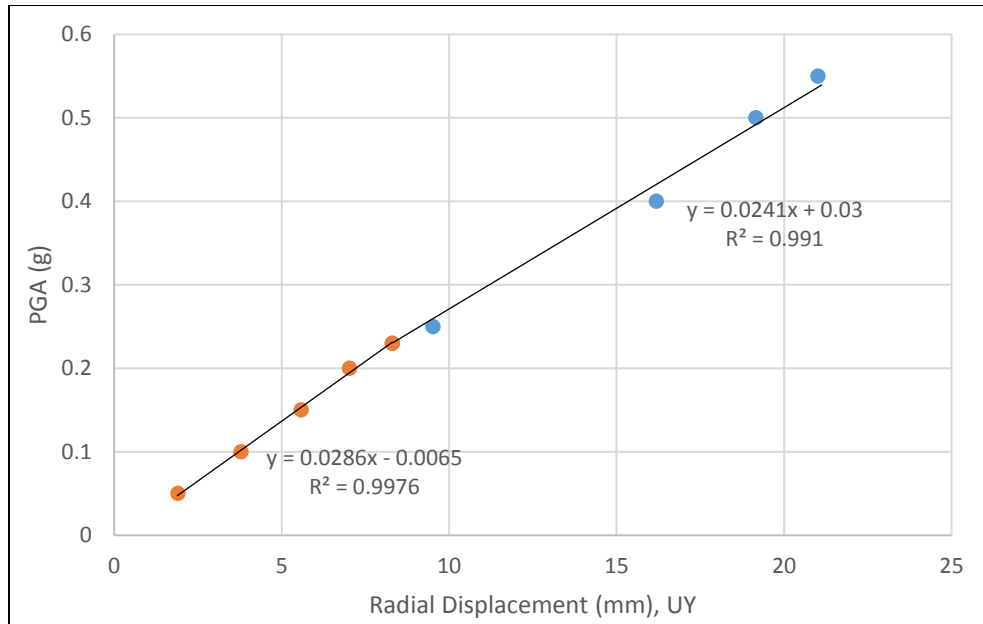
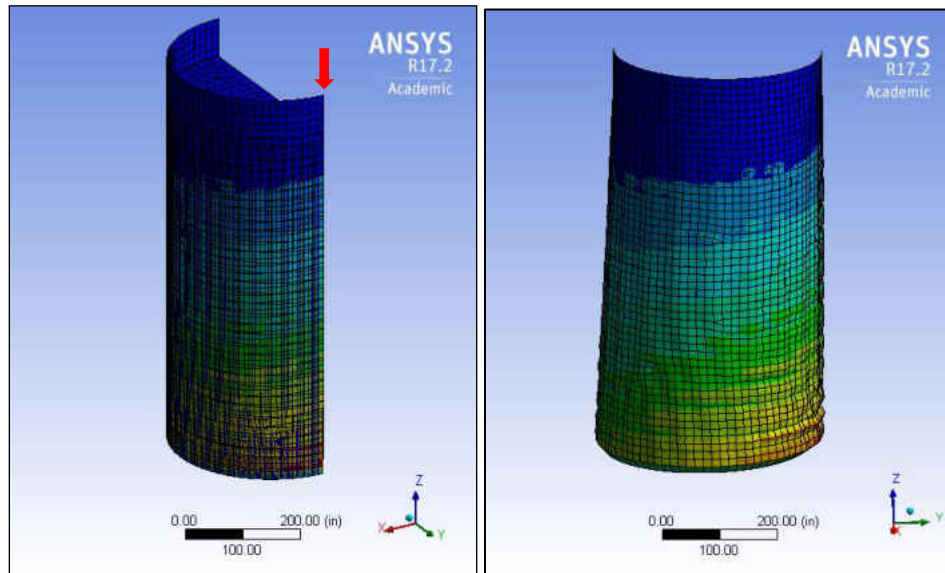


Figure 100. Pseudo equilibrium paths for the critical node of model 12 filled with water to 90% depth



(a) Undeformed shape

(b) Shell deformation

Figure 101. (a) Undeformed shape and (b) Shell deformation of Model 12 filled with water to 90% depth

6.4.3 Empty Cylindrical Tanks Subjected to the Parkfield Earthquake

The critical PGA values for the empty cylindrical tanks subjected to the Parkfield earthquake are very high. These high values of PGA also occurred when the empty cylindrical tanks subjected to El Centro earthquake as represented in the previous section. These PGA values are unrealistic for past real world earthquakes.

For von-Mises stresses at the dynamic buckling loads, different from the El Centro earthquake, the von-Mises stresses of four models out of twelve models are higher than the yield strength of 50,000 psi (344.74 MPa). Therefore, the buckling behaviors of the cylindrical tanks subjected to the Parkfield earthquake can be both elastic and plastic buckling. These buckling behaviors make the characteristic of the PGA values to the buckling mode shapes of the El Centro earthquake different from the Parkfield earthquake. The over-yield von-Mises stresses of model 7, model 8, model 9, and model 10 subjected to the Parkfield earthquake are 52,045 psi (358.84 MPa), 49,369 psi (340.39 MPa), 53,656 psi (369.95 MPa), and 51,137 psi (352.58 MPa), respectively. The buckling shapes of elastic buckling were different from the plastic buckling in this study. The buckling shapes of the elastic buckling occurred at the top of the cylindrical tanks, but the buckling shapes of the plastic buckling occurred just below the middle of the height of the tanks.

Table 22. Dynamic Buckling Points of Empty Tanks Subjected to the Parkfield Earthquake

H/D	PGA (g)		
	D/t=1000	D/t=1500	D/t=2000
0.5	72	55	28
1.0	50	42	23
1.5	45	40	22
2.0	42	32	20

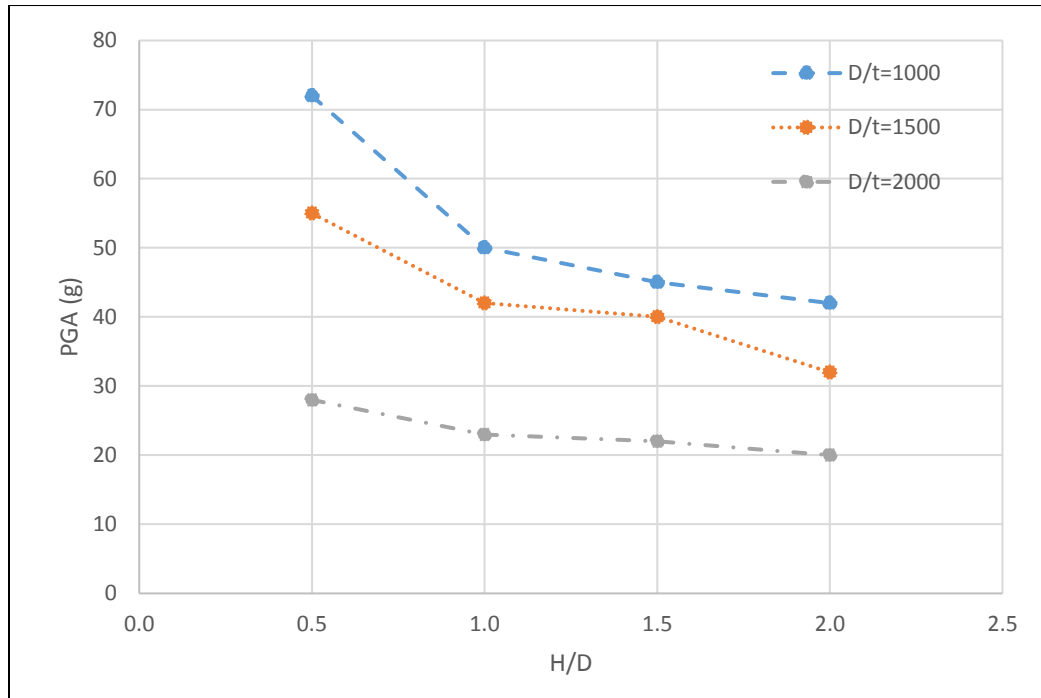


Figure 102. Plots of Dynamic Buckling Points of Empty Tanks Subjected to the Parkfield Earthquake, 2004

Model 1

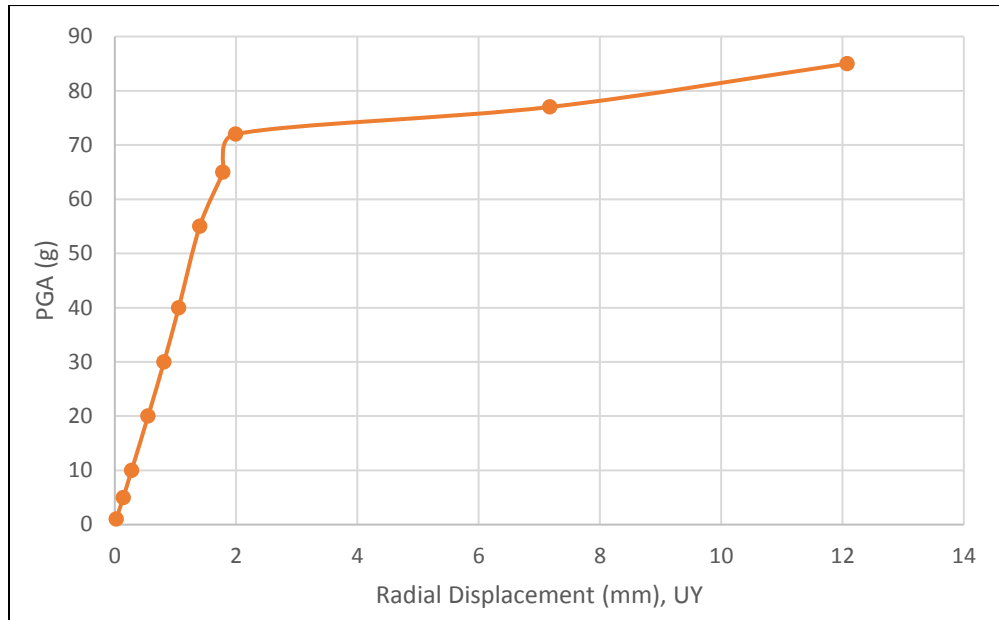


Figure 103. Pseudo equilibrium paths for the critical node of Model 1

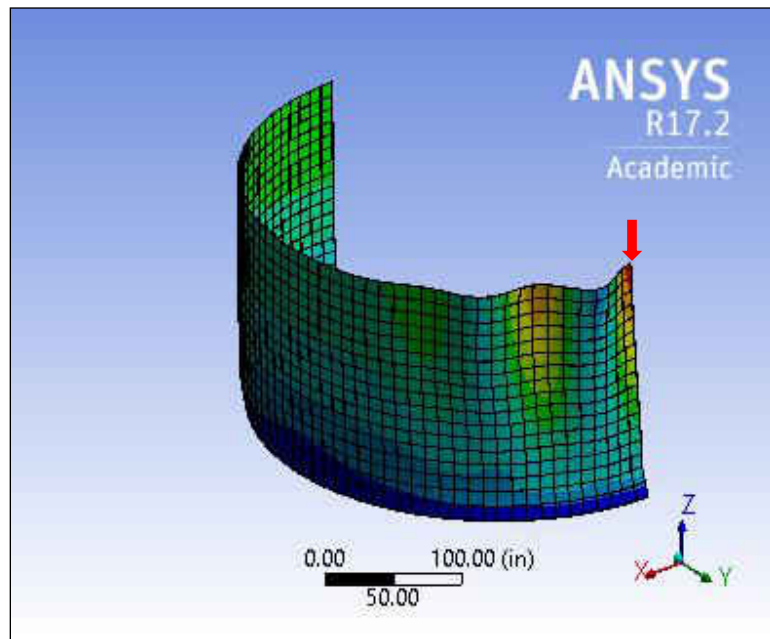


Figure 104. Deformation shape of Model 1 for PGA = 78g

Model 2

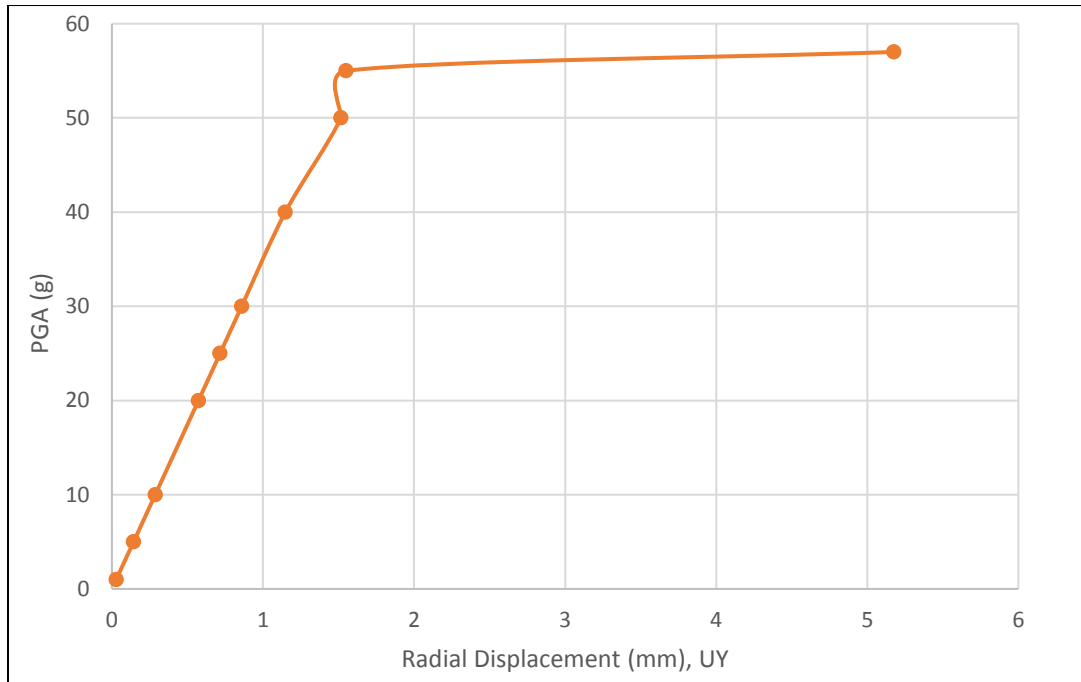


Figure 105. Pseudo equilibrium paths for the critical node of Model 2

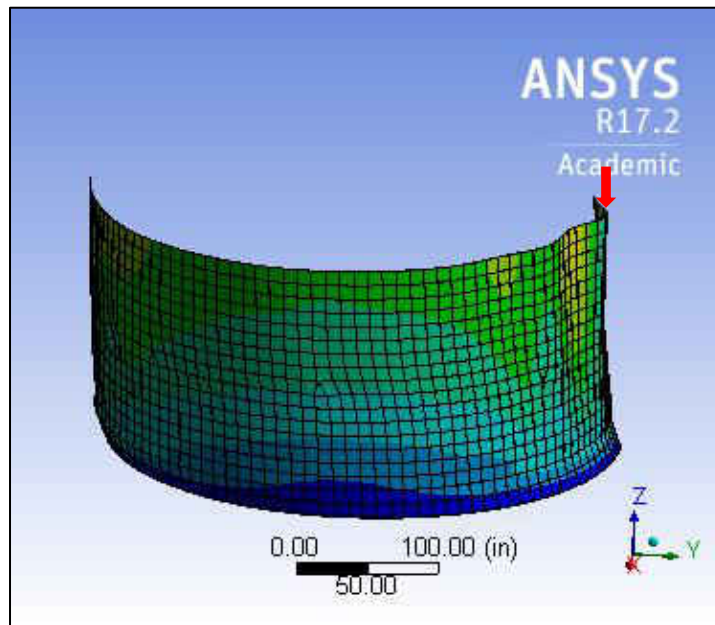


Figure 106. Deformation shape of Model 2 for PGA = 57g

Model 3

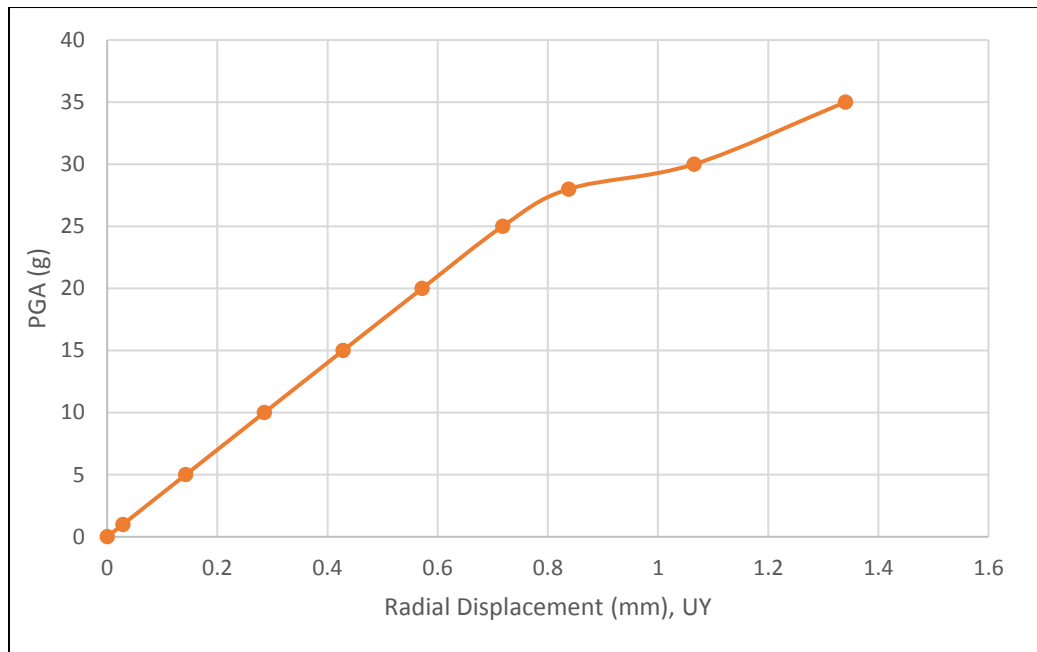


Figure 107. Pseudo equilibrium paths for the critical node of Model 3

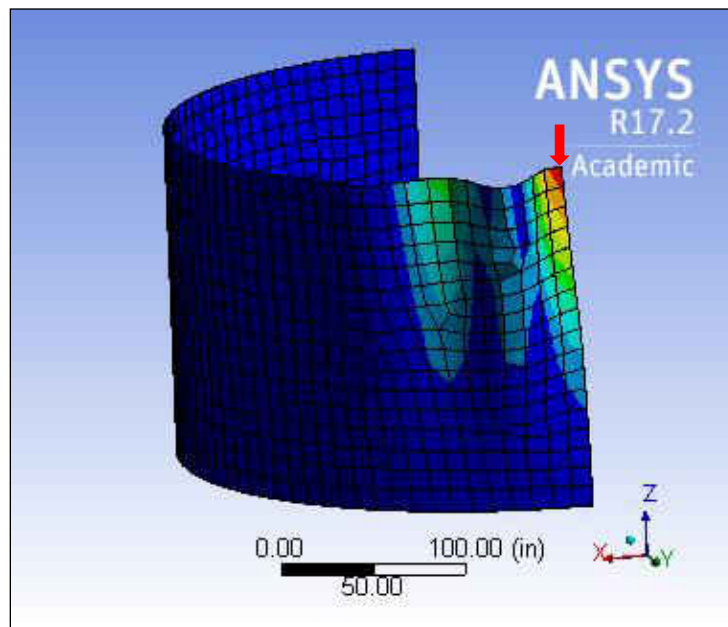


Figure 108. Deformation shape of Model 3 for PGA = 30g

Model 4

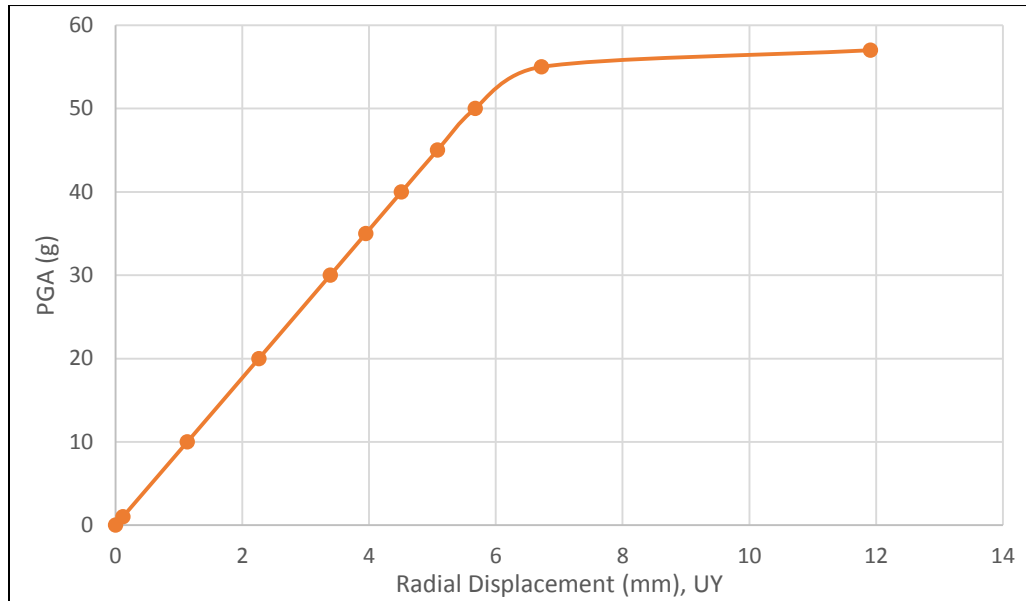


Figure 109. Pseudo equilibrium paths for the critical node of Model 4

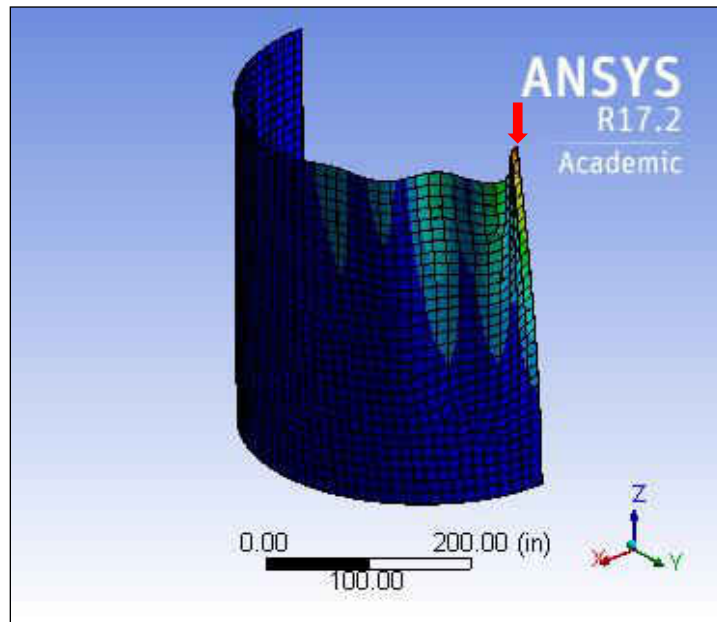


Figure 110. Deformation shape of Model 4 for PGA = 57g

Model 5

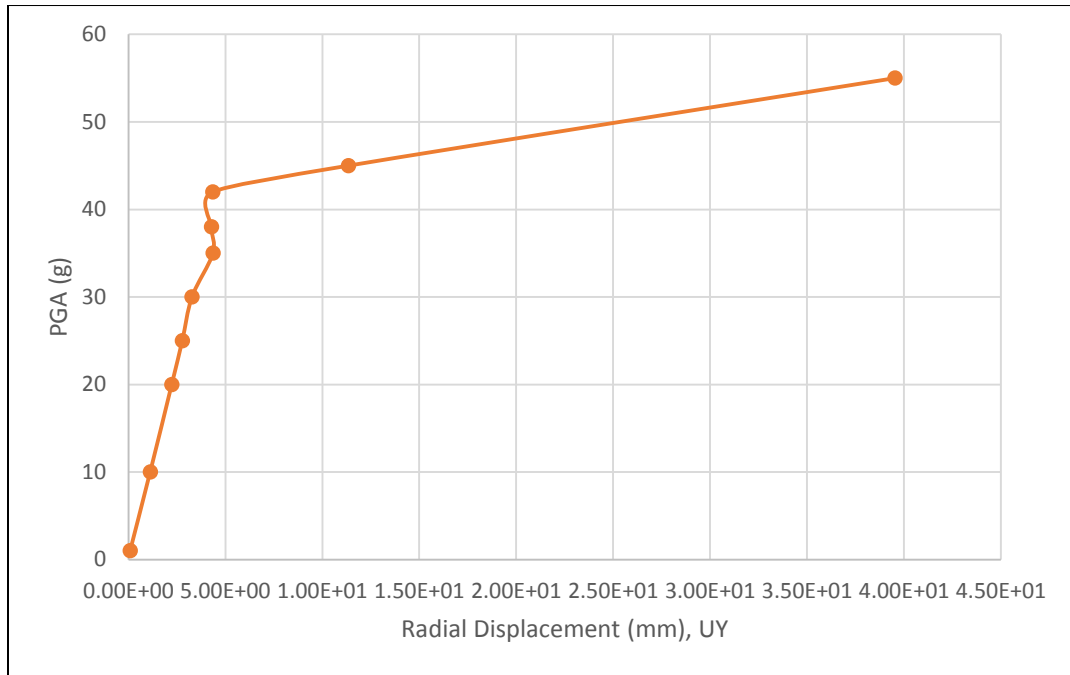


Figure 111. Pseudo equilibrium paths for the critical node of Model 5

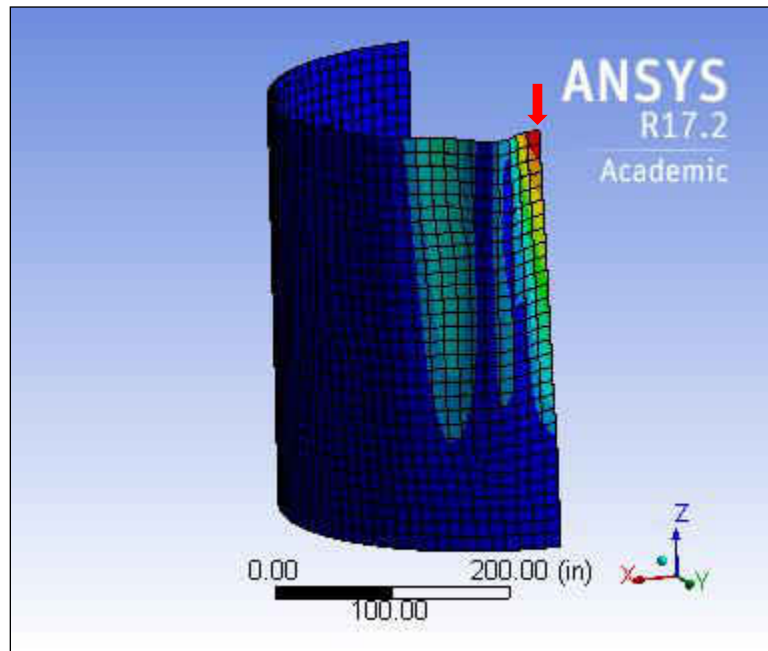


Figure 112. Deformation shape of Model 5 for PGA = 45g

Model 6

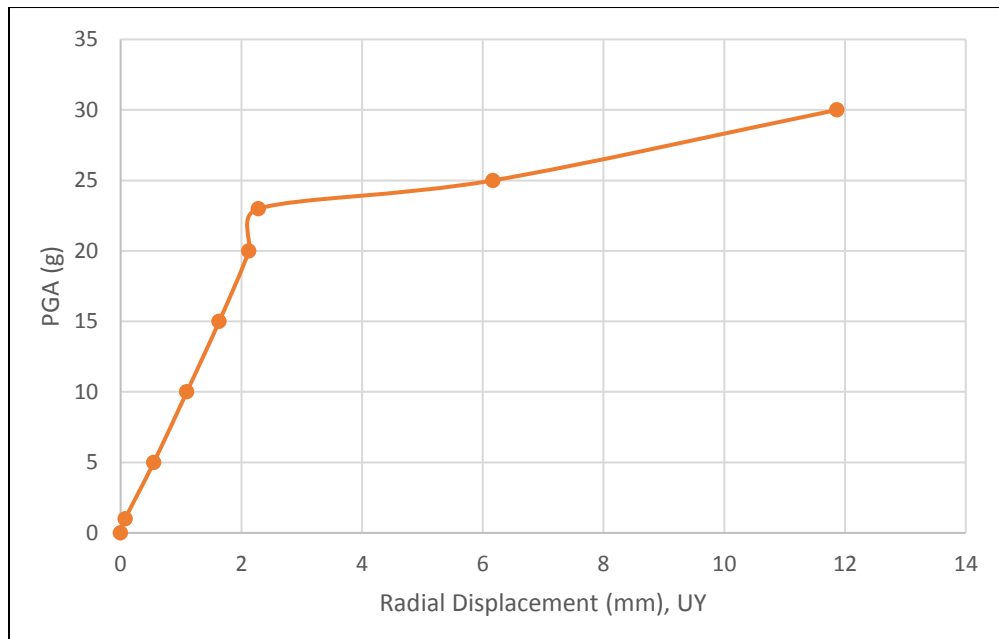


Figure 113. Pseudo equilibrium paths for the critical node of Model 6

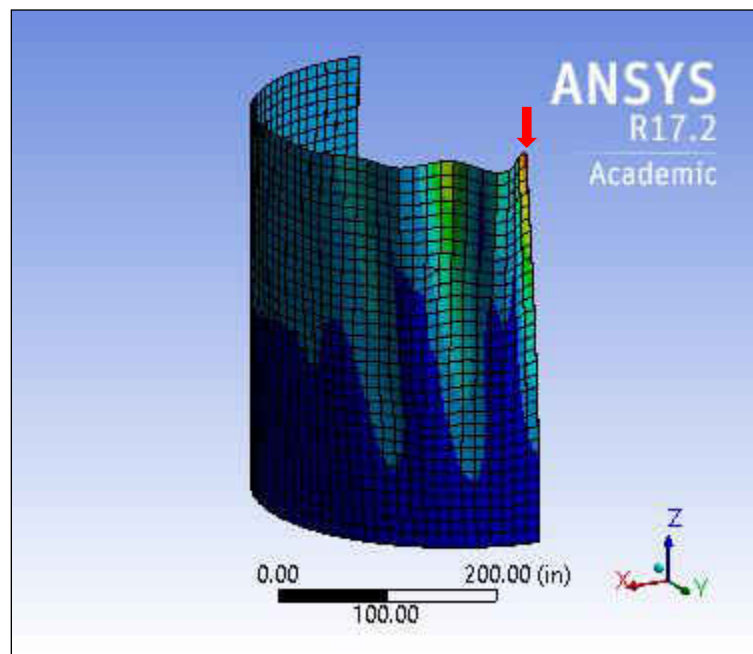


Figure 114. Deformation shape of Model 6 for PGA = 25g

Model 7

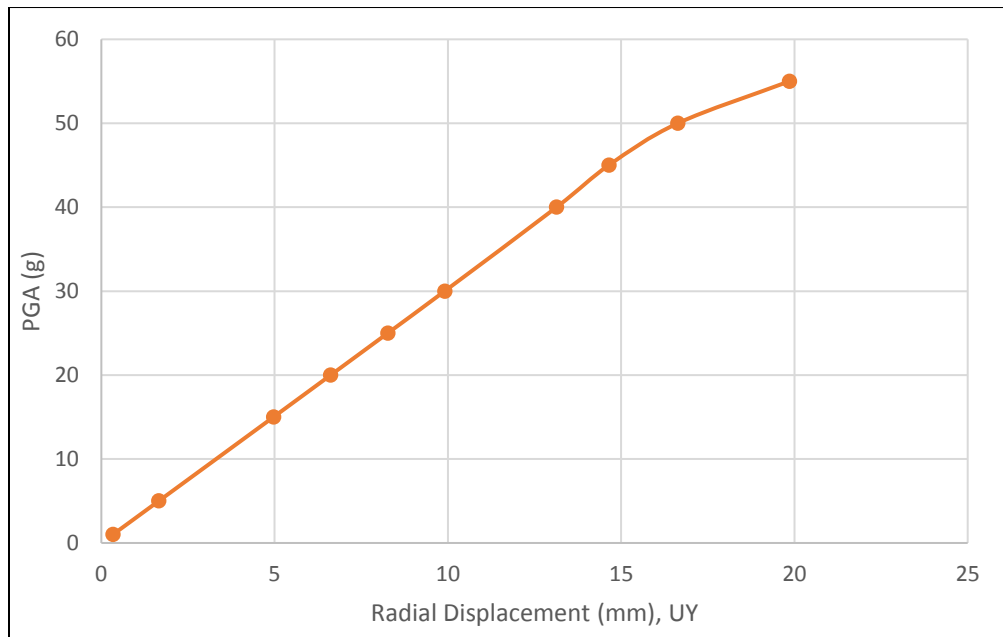


Figure 115. Pseudo equilibrium paths for the critical node of Model 7

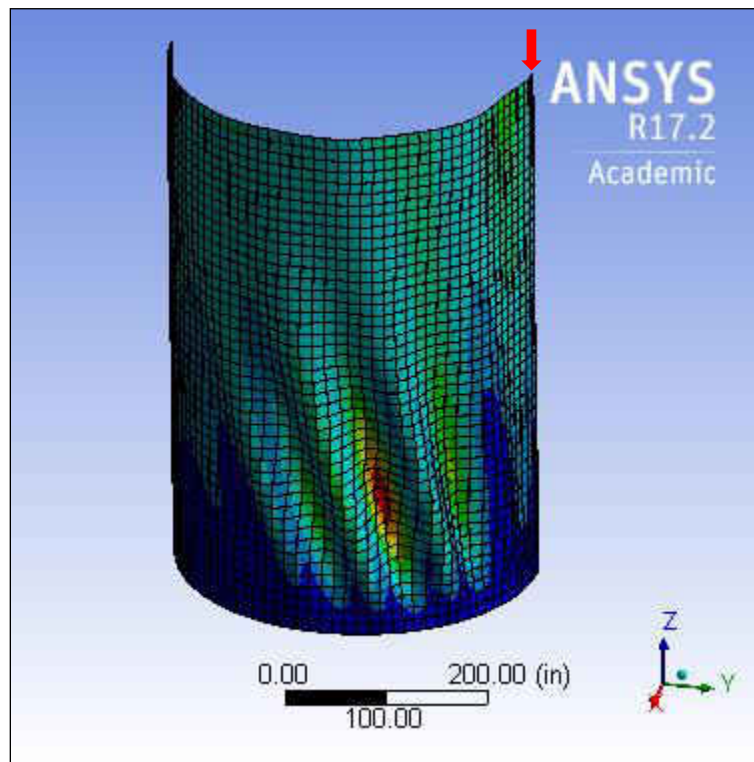


Figure 116. Deformation shape of Model 7 for PGA = 55g

Model 8

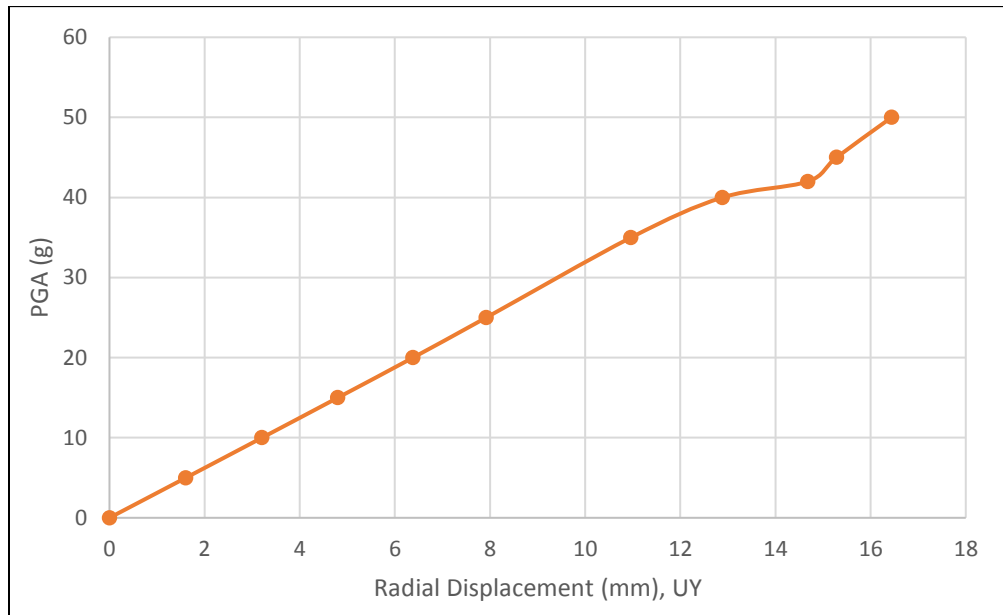


Figure 117. Pseudo equilibrium paths for the critical node of Model 8

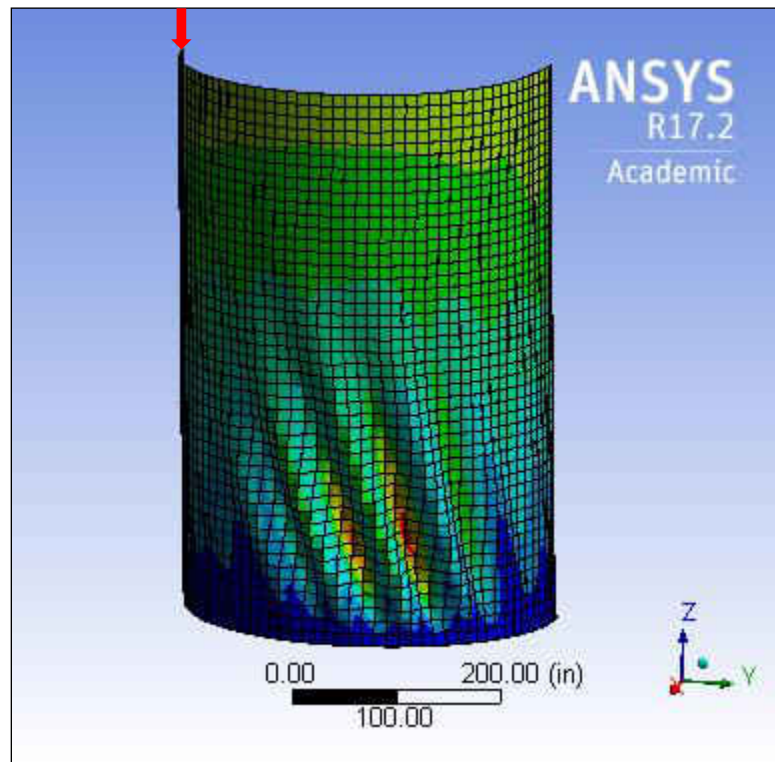


Figure 118. Deformation shape of Model 8 for PGA = 45g

Model 9

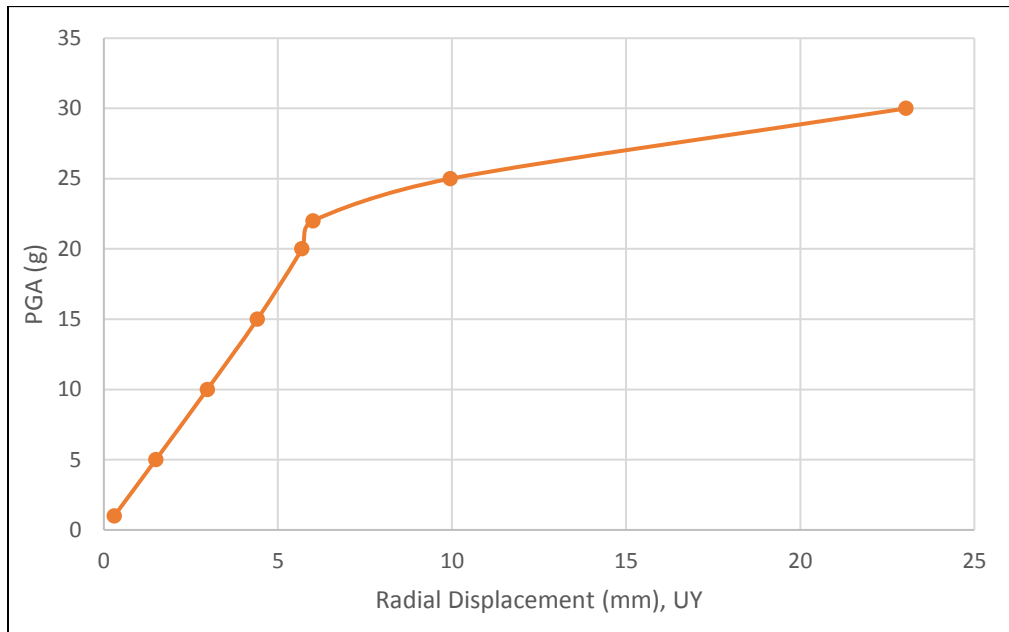


Figure 119. Pseudo equilibrium paths for the critical node of Model 9

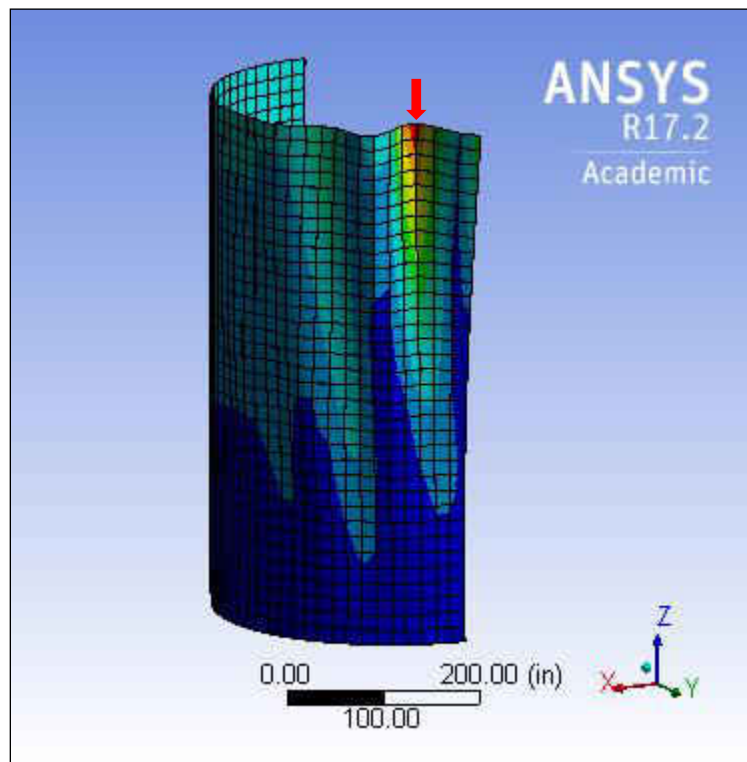


Figure 120. Deformation shape of Model 9 for PGA = 25g

Model 10

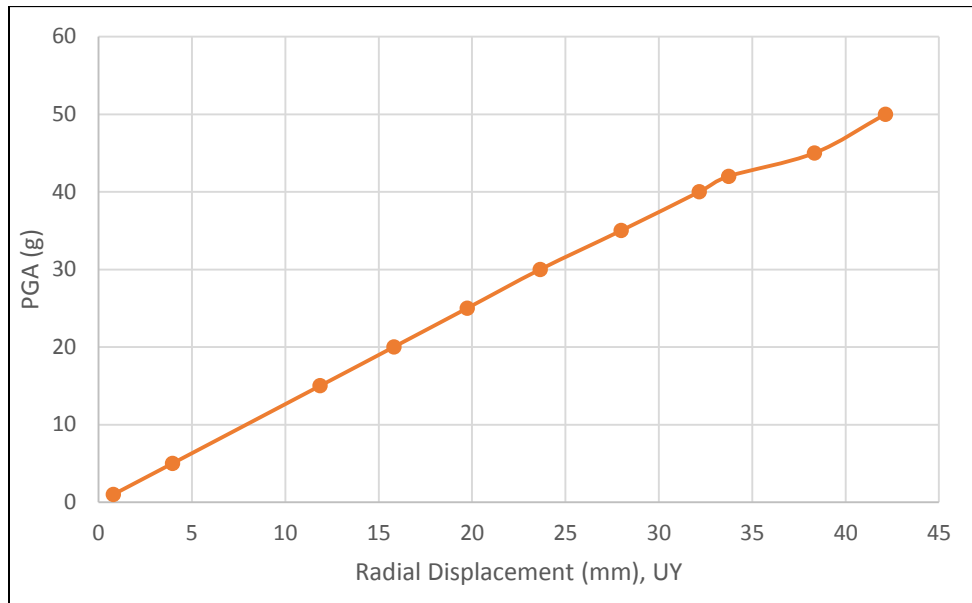


Figure 121. Pseudo equilibrium paths for the critical node of Model 10

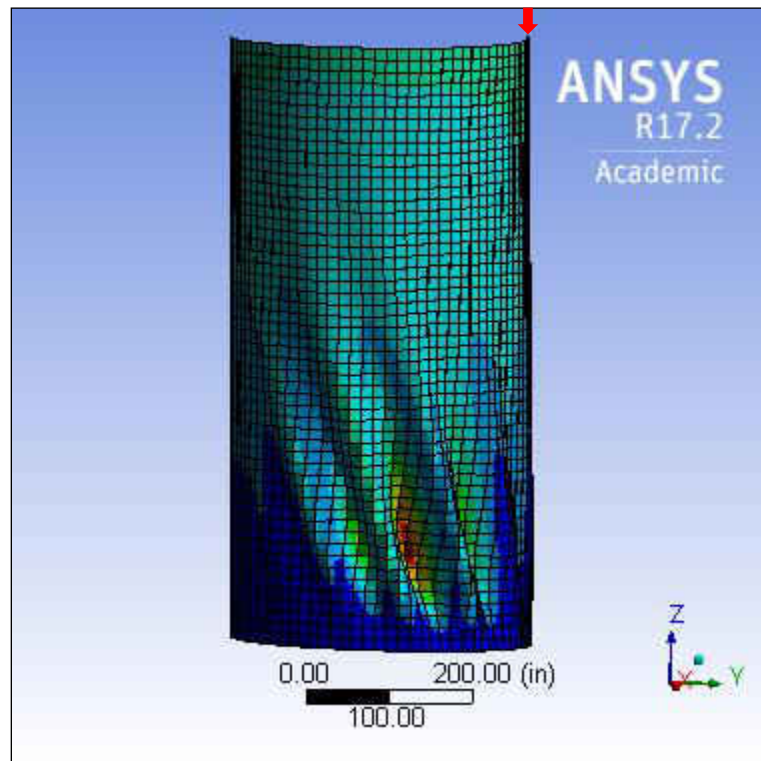


Figure 122. Deformation shape of Model 10 for PGA = 50g

Model 11

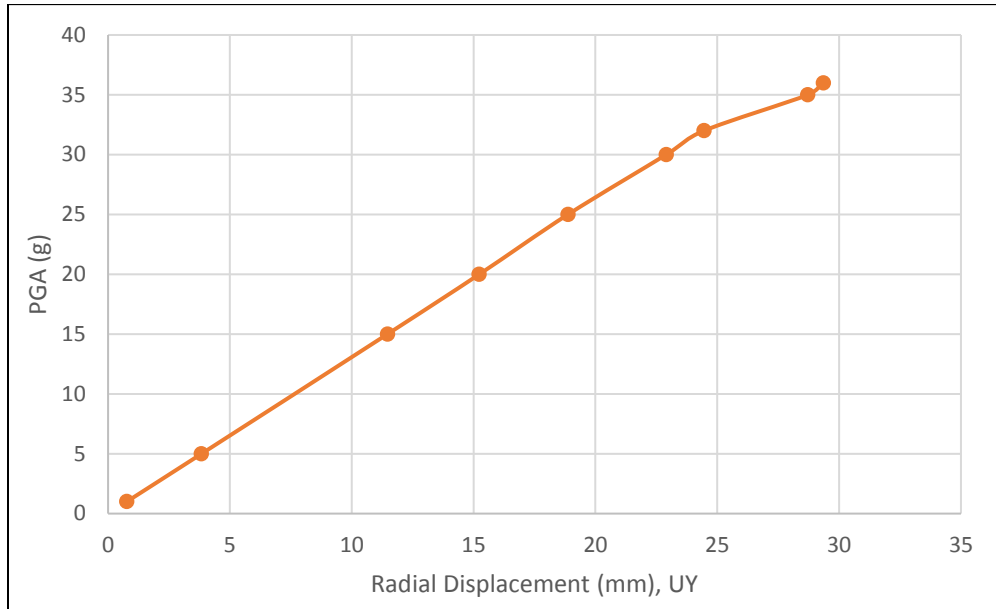


Figure 123. Pseudo equilibrium paths for the critical node of Model 11

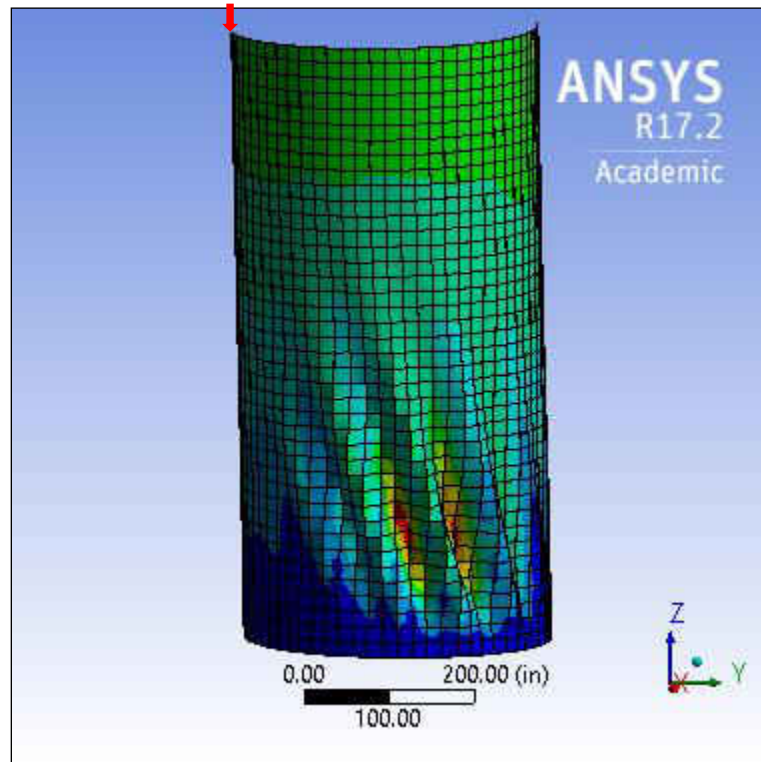


Figure 124. Deformation shape of Model 11 for PGA = 35g

Model 12

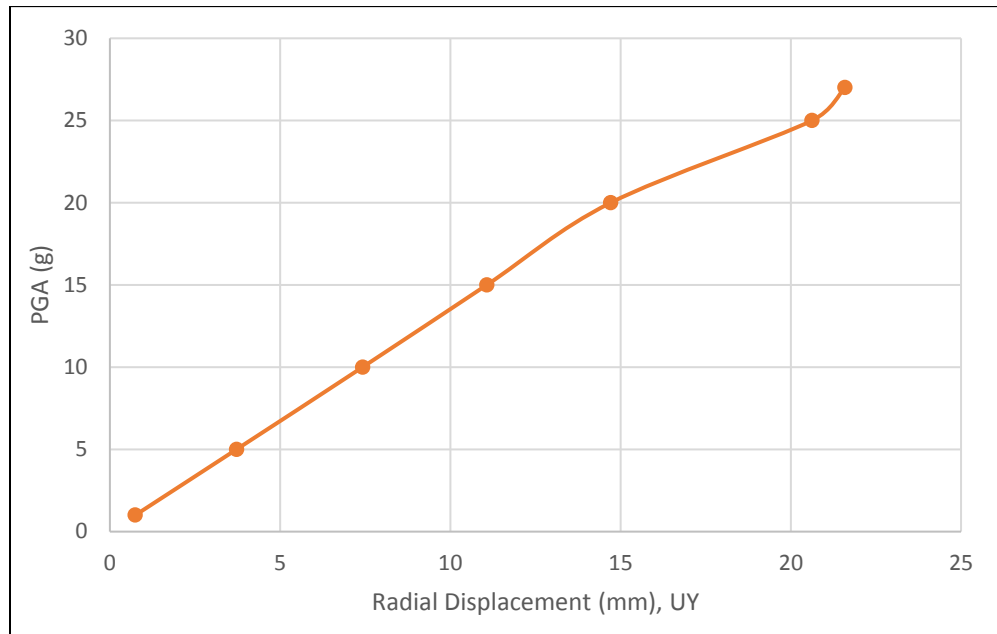


Figure 125. Pseudo equilibrium paths for the critical node of Model 12

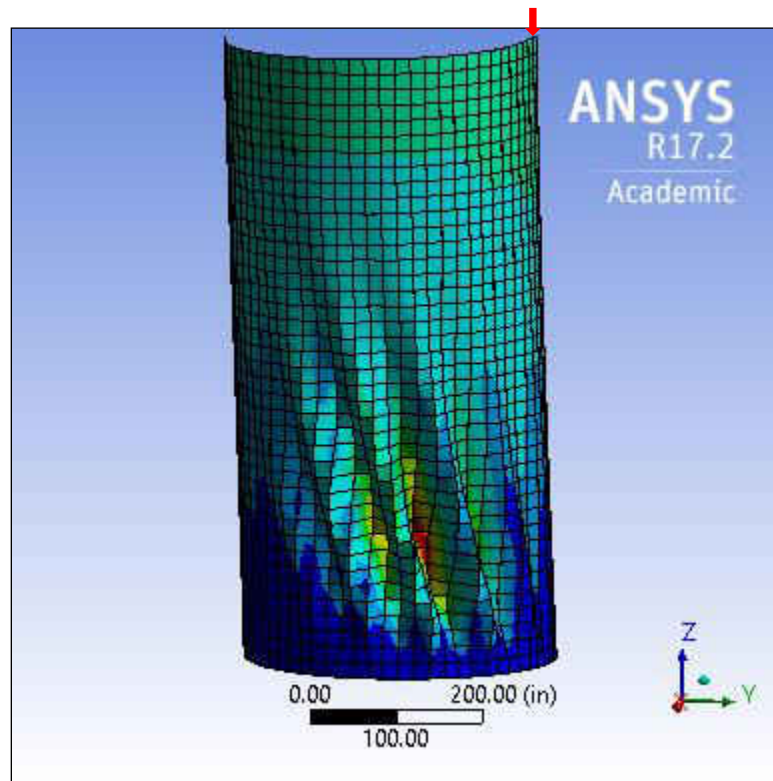


Figure 126. Deformation shape of Model 12 for PGA = 27g

6.4.4 Cylindrical Tanks Filled with Water up to 90% of Height Subjected to the Parkfield Earthquake

For the Parkfield earthquake, the critical PGA values for the cylindrical tanks filled with water up to 90% of their height, similarly to the El Centro earthquake, are significantly smaller than the empty cylindrical tanks. However, the results show that there are dramatic increases of displacement when the values of PGA increase for model 2 and model 6 when they were subjected to the Parkfield earthquake. The buckling points of model 6, model 9, model 10, model 11, and model 12 are 0.35g, 0.32g, 0.65g, 0.45g, and 0.20g, respectively. These buckling points are less than 0.678g which is the PGA of the Parkfield earthquake; therefore, based on this study, the shell buckling occurs for model 6, model 9, model 10, model 11, and model 12 when they are subjected to the Parkfield earthquake.

For von-Mises stresses at the dynamic buckling loads, it was found that von-Mises stresses for all models are less than the yield stress of the steel which is 50,000 psi (344.74 MPa). The highest von-Mises stress occurred with Model 12 at 38,524 psi (265.61 MPa).

Table 23. Dynamic Buckling Points of Tanks filled with water to 90% depth subjected to the Parkfield earthquake, 2004

H/D	PGA (g)		
	D/t=1000	D/t=1500	D/t=2000
0.5	1.50	1.20	0.72
1.0	1.30	0.90	0.35
1.5	1.05	0.85	0.32
2.0	0.65	0.45	0.20

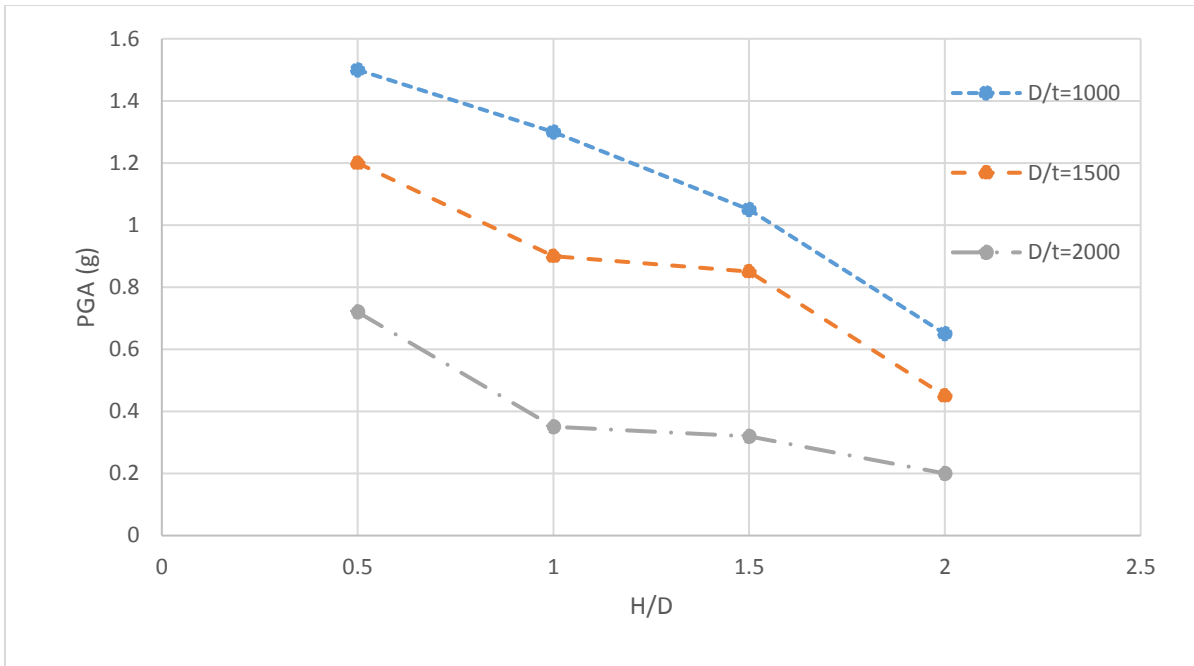


Figure 127. Plots of Dynamic Buckling Points of Tanks filled with water to 90% depth subjected to the Parkfield earthquake, 2004

Model 1

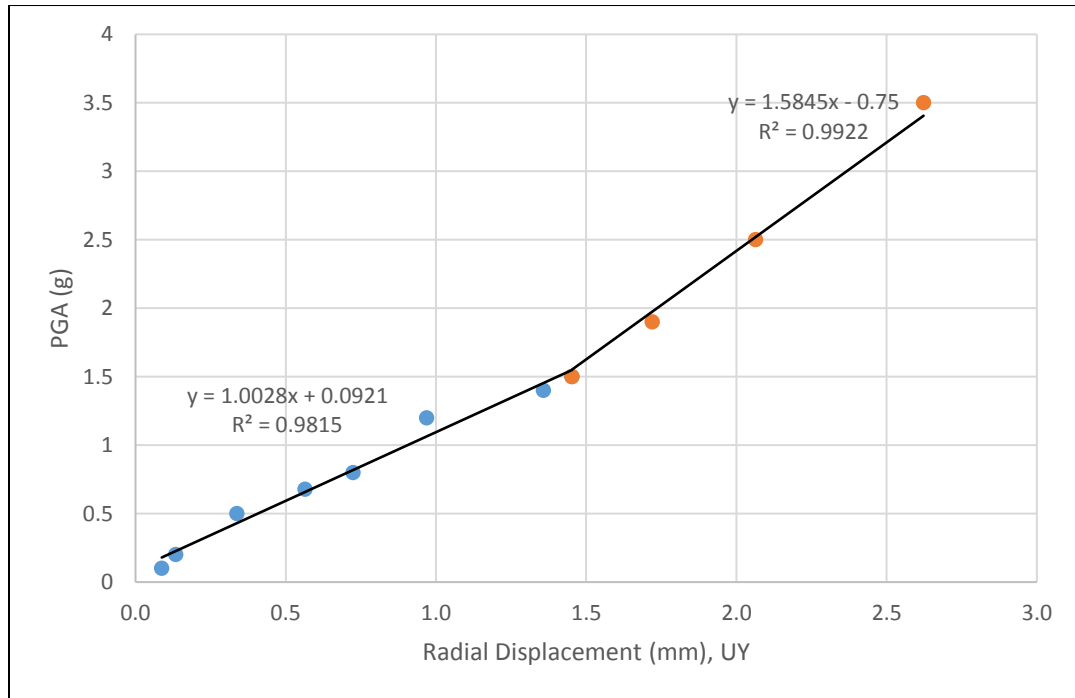
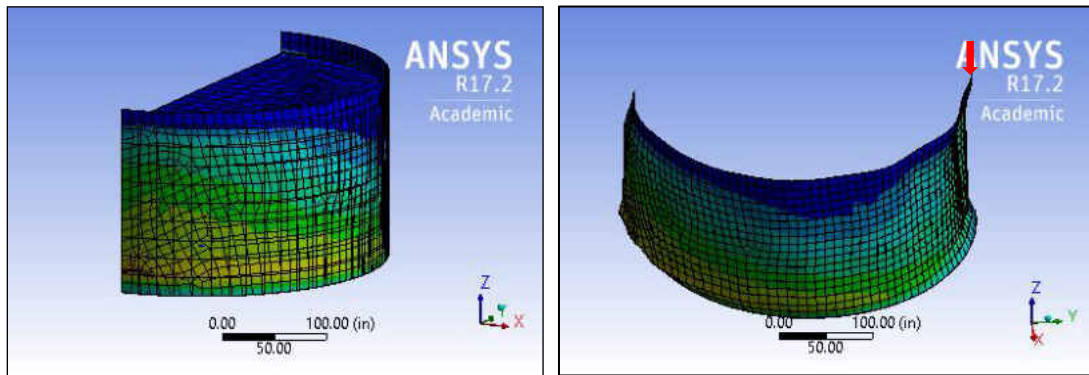


Figure 128. Pseudo equilibrium paths for the critical node of model 1 filled with water to 90% depth



(a) Undeformed shape

(b) Shell deformation

Figure 129. (a) Undeformed shape and (b) Shell deformation of Model 1 filled with water to 90% depth

Model 2

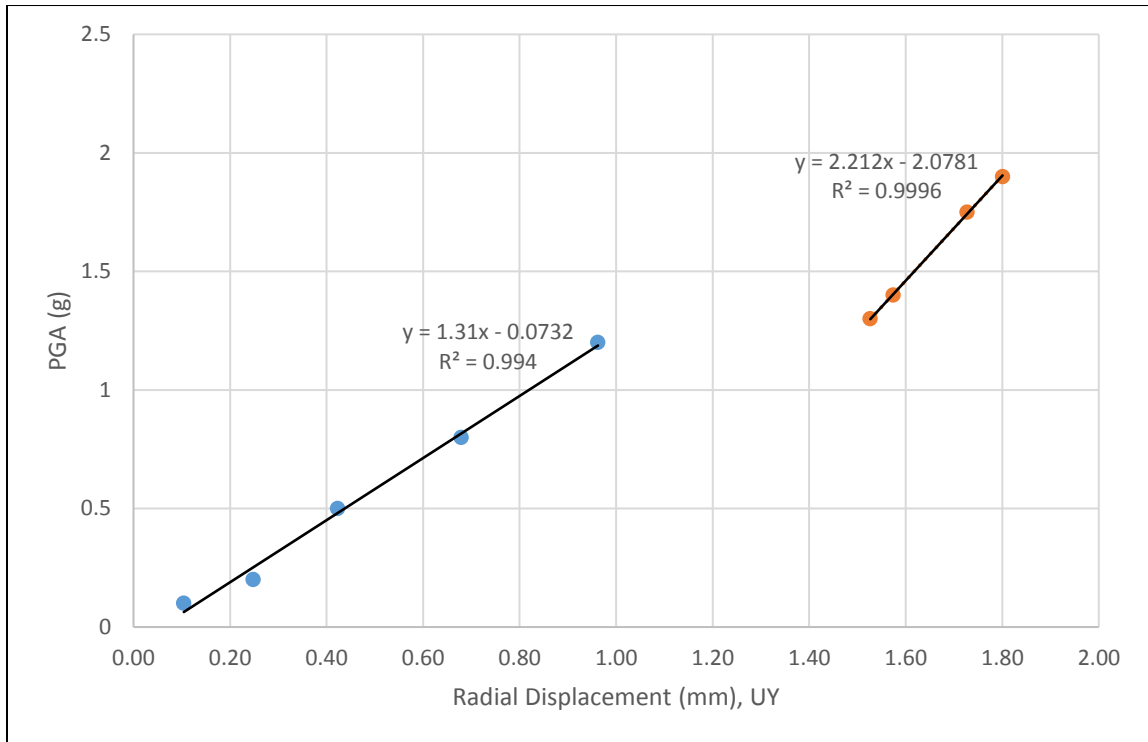
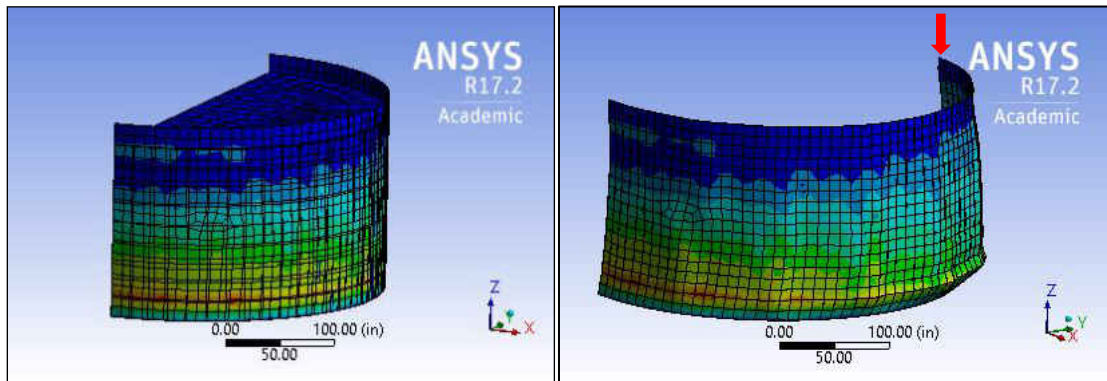


Figure 130. Pseudo equilibrium paths for the critical node of model 2 filled with water to 90% depth



(a) Undeformed shape

(b) Shell deformation

Figure 131. (a) Undeformed shape and (b) Shell deformation of Model 2 filled with water to 90% depth

Model 3

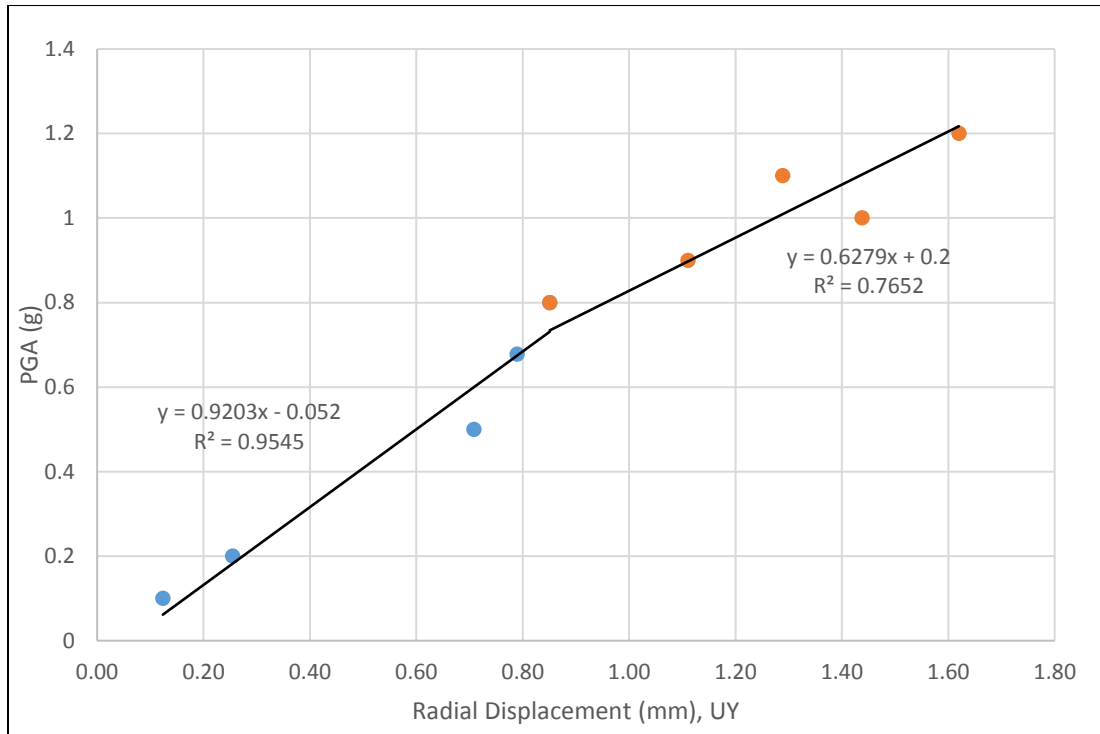
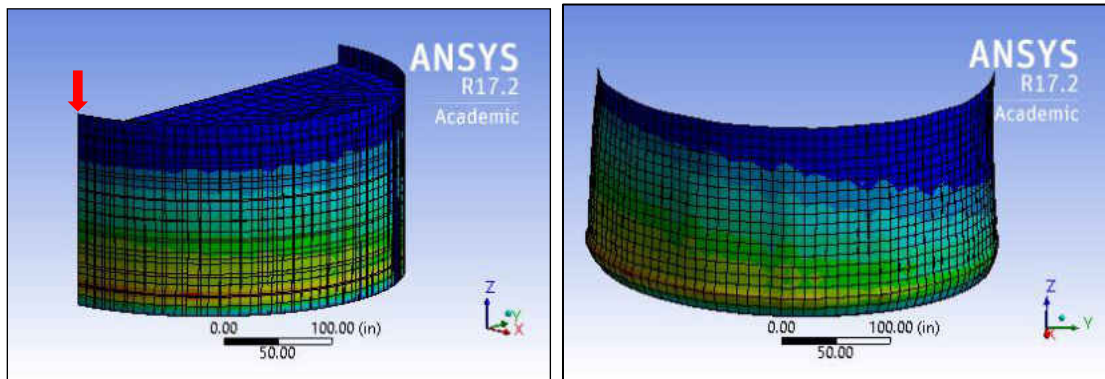


Figure 132. Pseudo equilibrium paths for the critical node of model 3 filled with water to 90% depth



(a) Undeformed shape

(b) Shell deformation

Figure 133. (a) Undeformed shape and (b) Shell deformation of Model 3 filled with water to 90% depth

Model 4

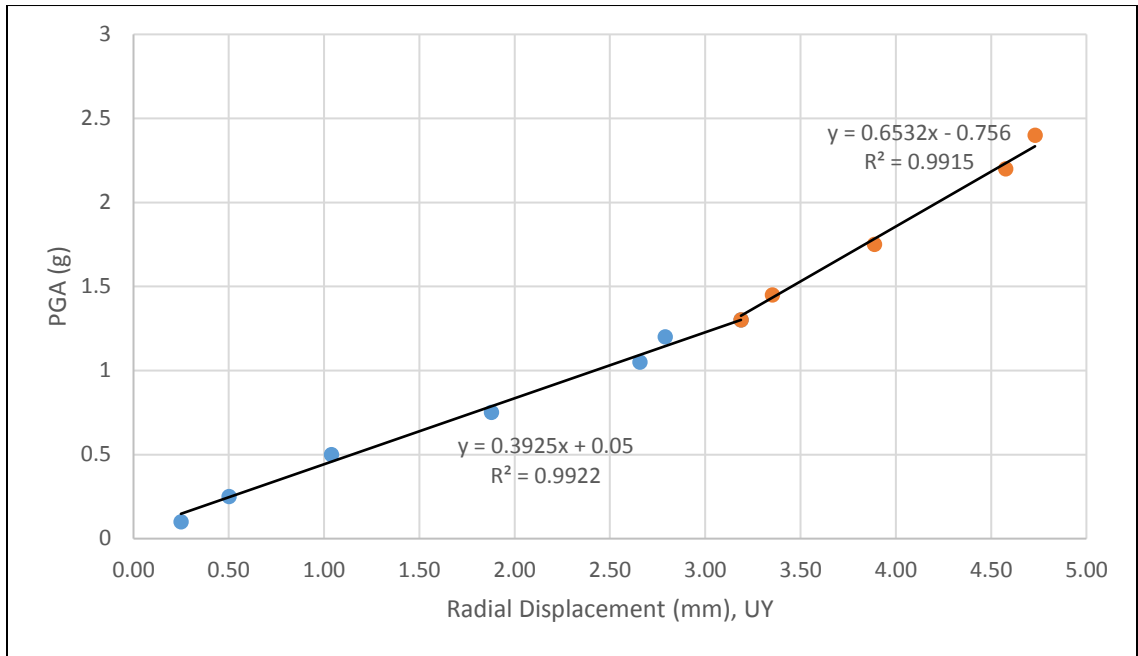
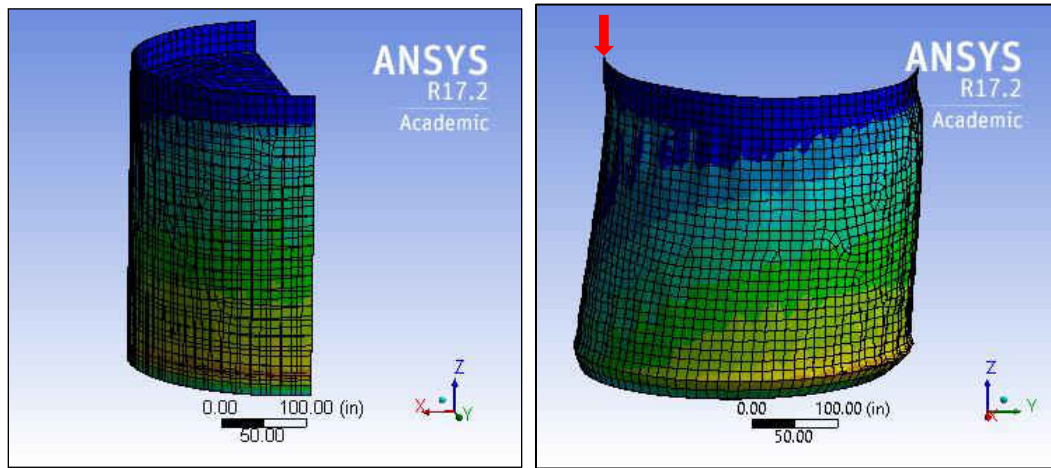


Figure 134. Pseudo equilibrium paths for the critical node of model 4 filled with water to 90% depth



(a) Undeformed shape

(b) Shell deformation

Figure 135. (a) Undeformed shape and (b) Shell deformation of Model 4 filled with water to 90% depth

Model 5

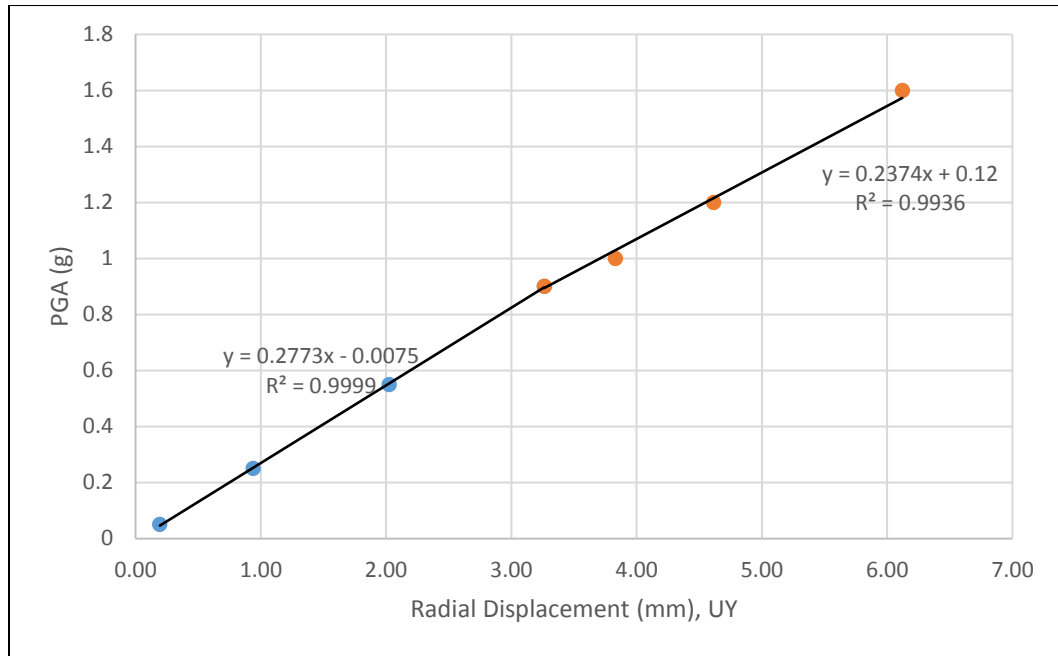
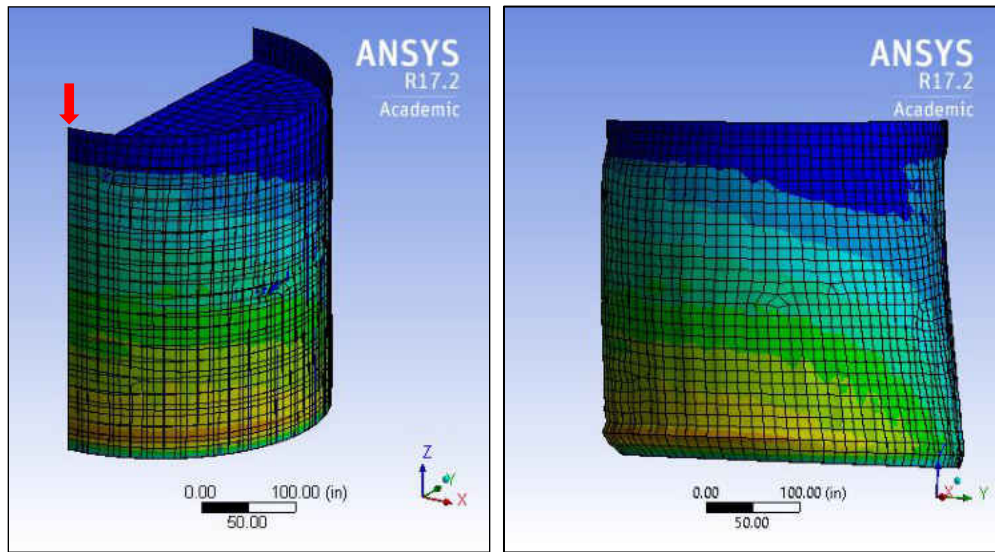


Figure 136. Pseudo equilibrium paths for the critical node of model 5 filled with water to 90% depth



(a) Undeformed shape

(b) Shell deformation

Figure 137. (a) Undeformed shape and (b) Shell deformation of Model 5 filled with water to 90% depth

Model 6

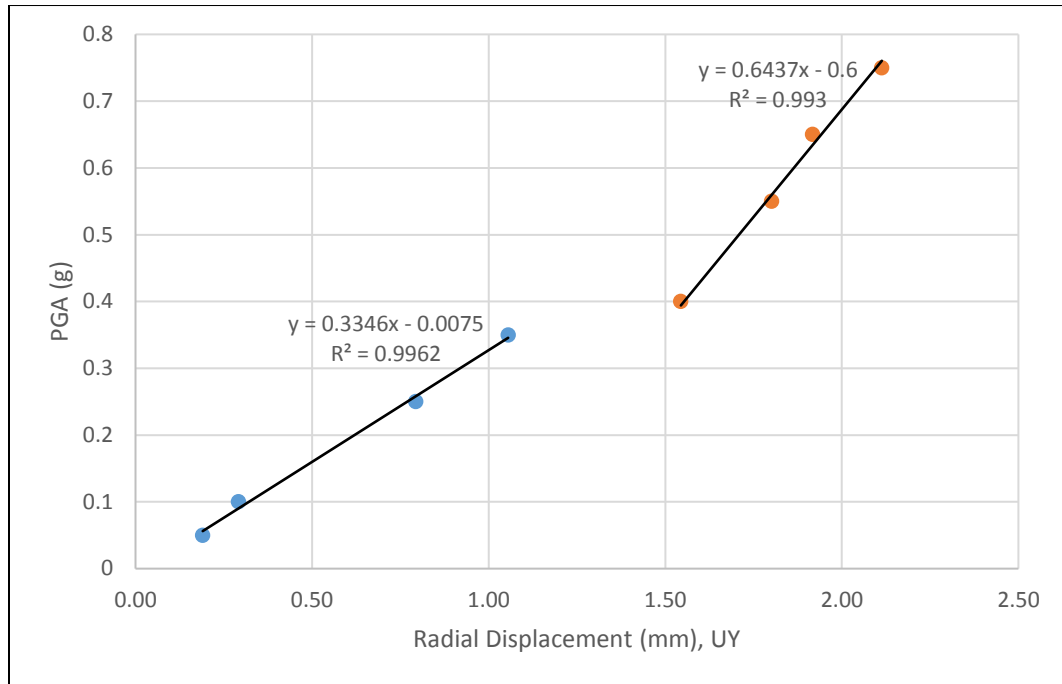
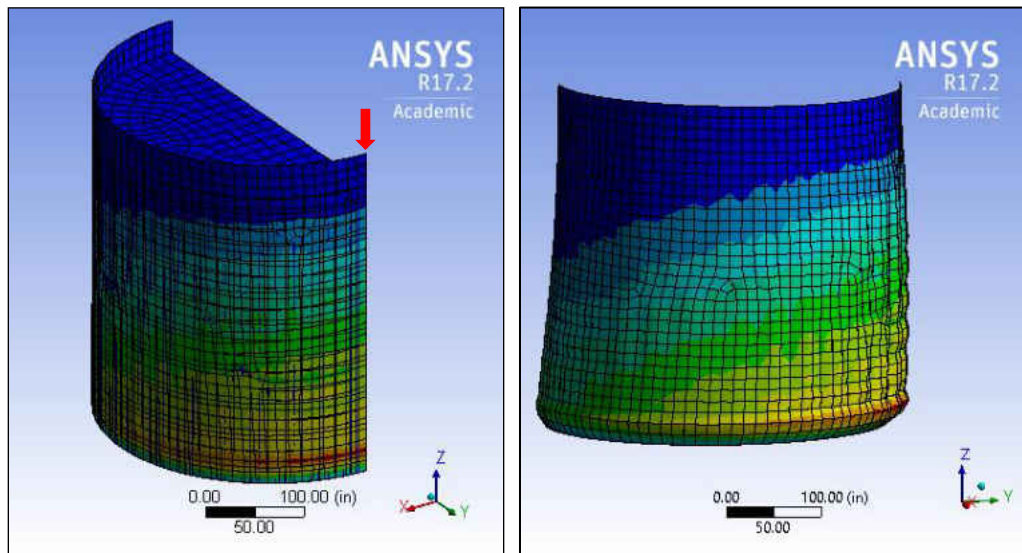


Figure 138. Pseudo equilibrium paths for the critical node of model 6 filled with water to 90% depth



(a) Undeformed shape

(b) Shell deformation

Figure 139. (a) Undeformed shape and (b) Shell deformation of Model 6 filled with water to 90% depth

Model 7

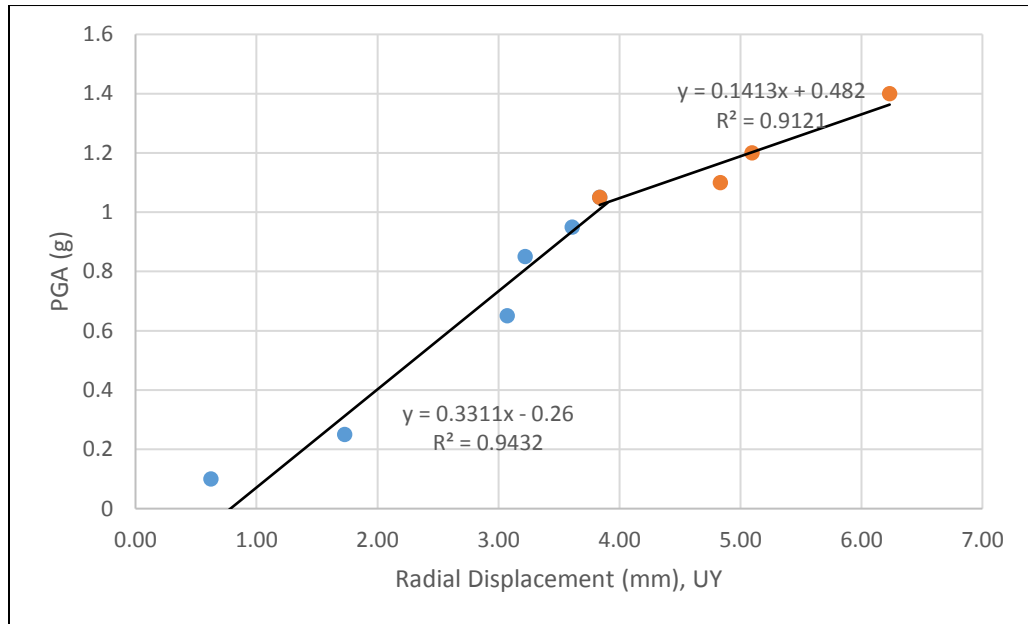
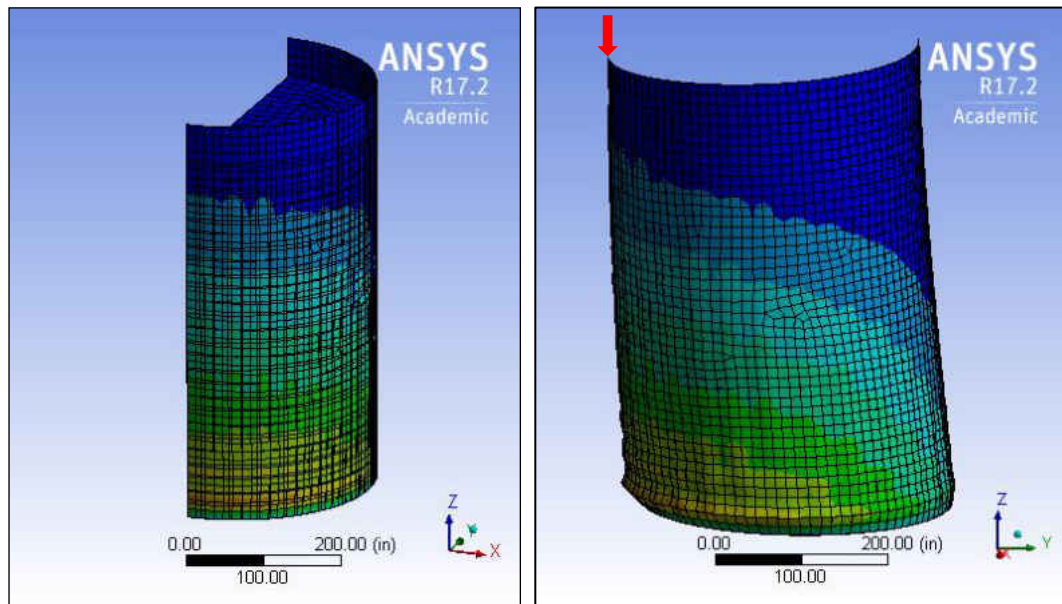


Figure 140. Pseudo equilibrium paths for the critical node of model 7 filled with water to 90% depth



(a) Undeformed shape

(b) Shell deformation

Figure 141. (a) Undeformed shape and (b) Shell deformation of Model 7 filled with water to 90% depth

Model 8

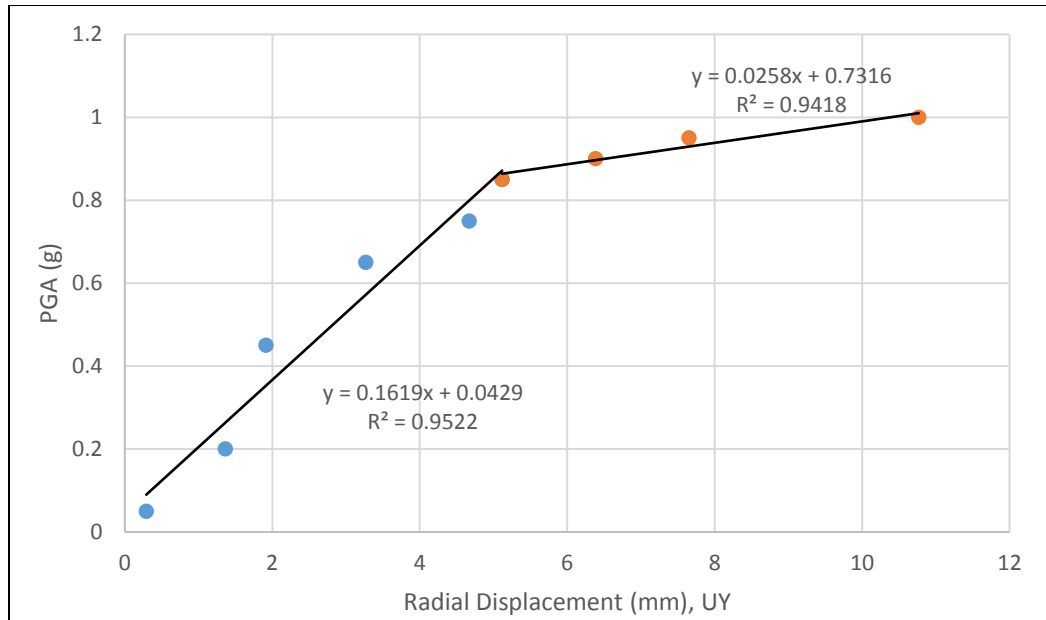
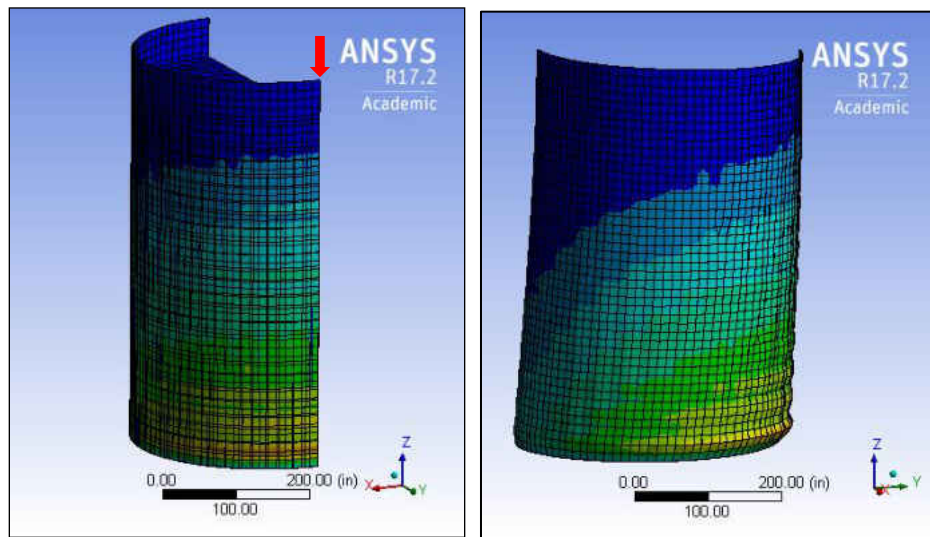


Figure 142. Pseudo equilibrium paths for the critical node of model 8 filled with water to 90% depth



(a) Undeformed shape

(b) Shell deformation

Figure 143. (a) Undeformed shape and (b) Shell deformation of Model 8 filled with water to 90% depth

Model 9

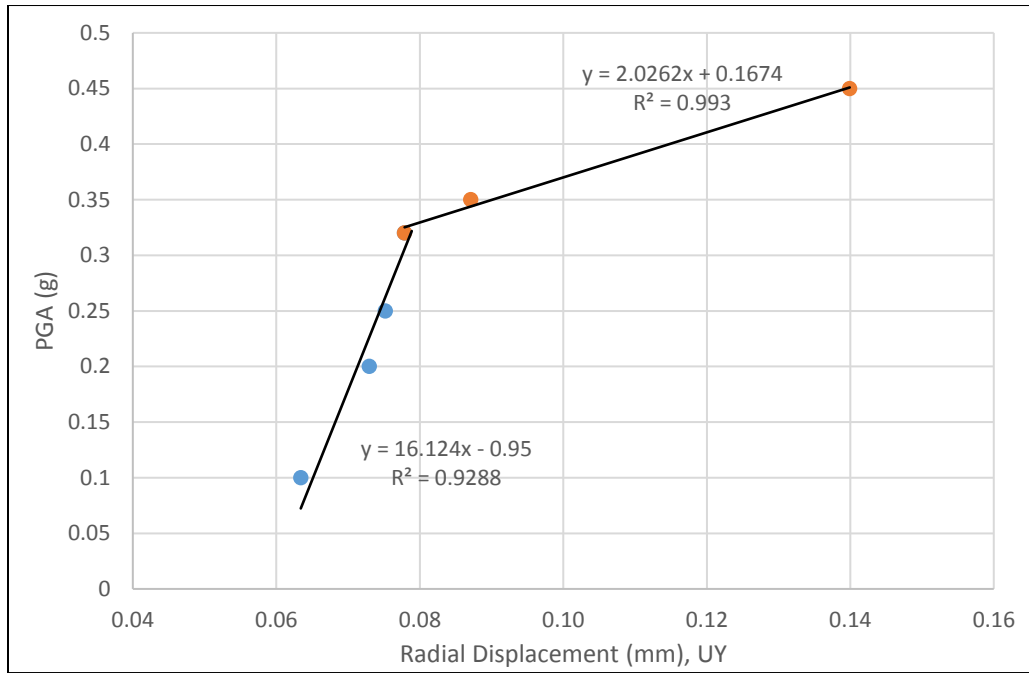
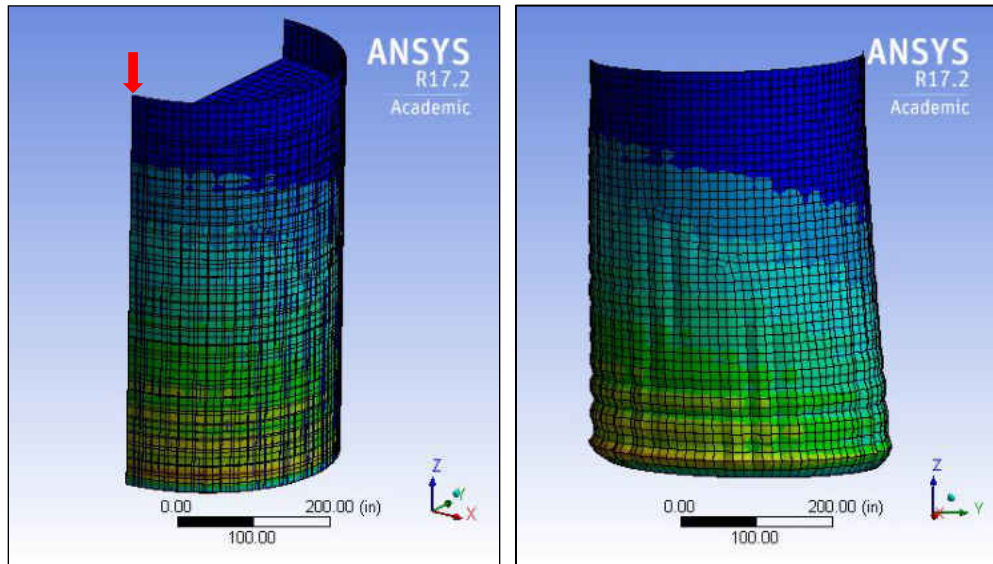


Figure 144. Pseudo equilibrium paths for the critical node of model 9 filled with water to 90% depth



(a) Undeformed shape

(b) Shell deformation

Figure 145. (a) Undeformed shape and (b) Shell deformation of Model 9 filled with water to 90% depth

Model 10

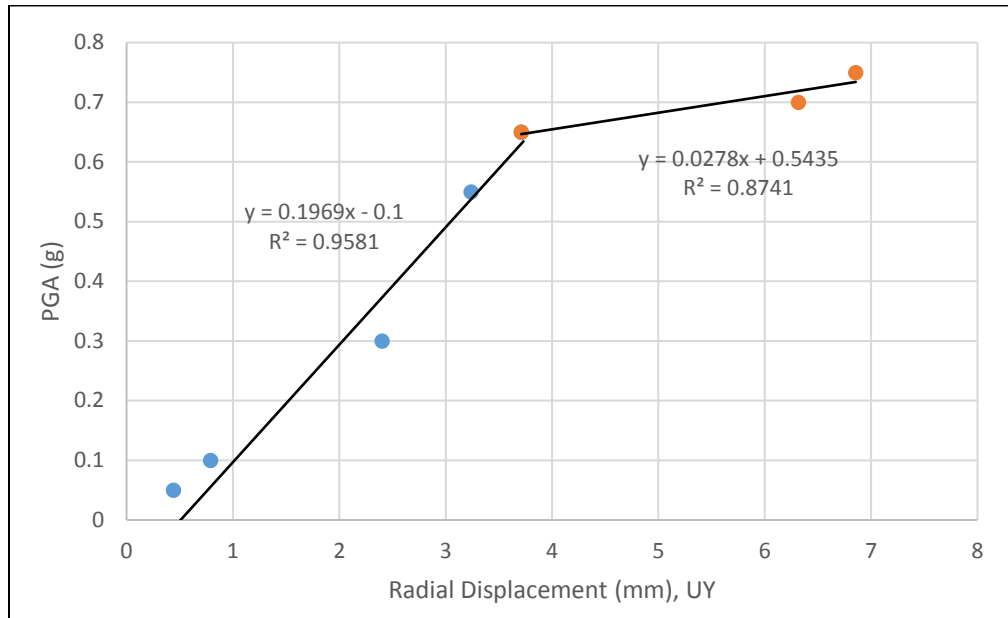
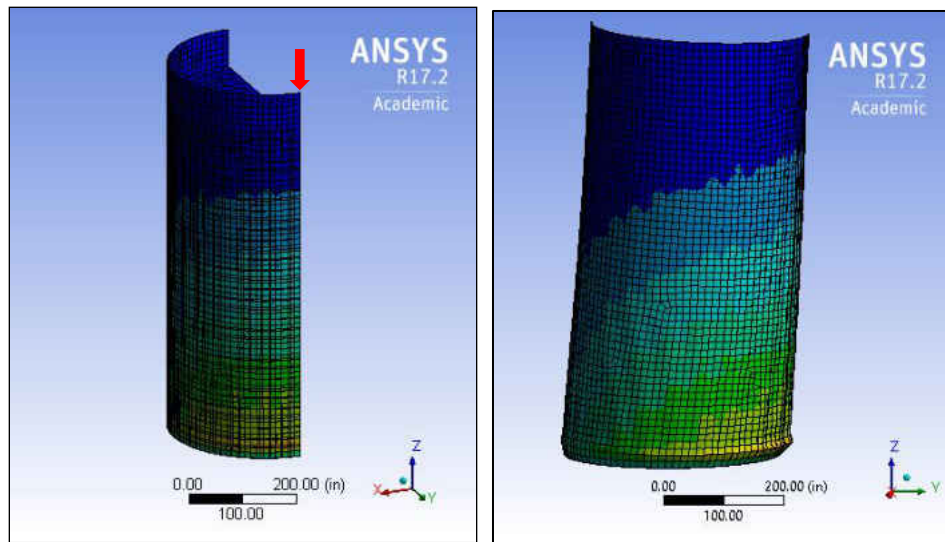


Figure 146. Pseudo equilibrium paths for the critical node of model 10 filled with water to 90% depth



(a) Undeformed shape

(b) Shell deformation

Figure 147. (a) Undeformed shape and (b) Shell deformation of Model 10 filled with water to 90% depth

Model 11

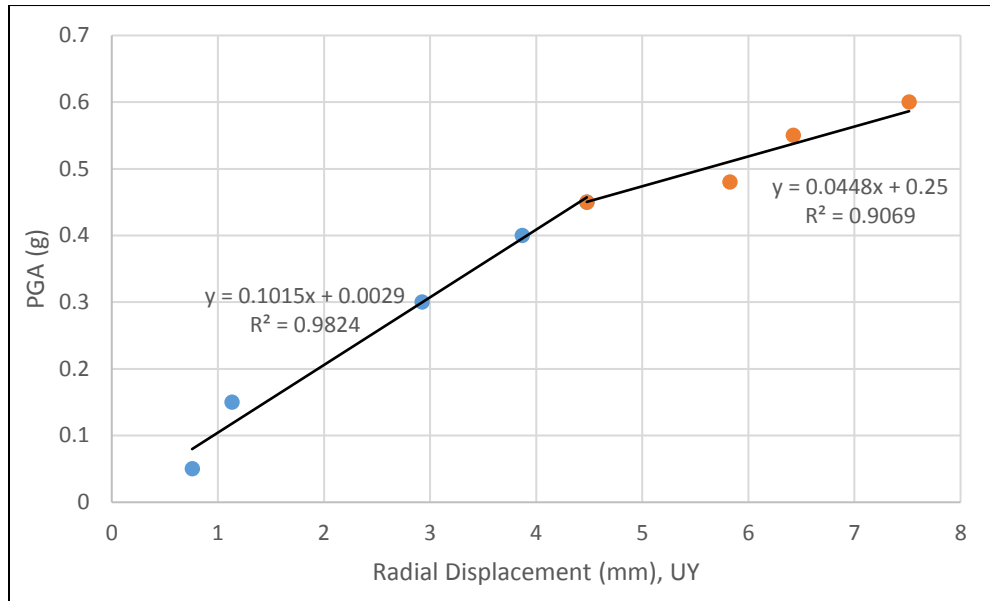
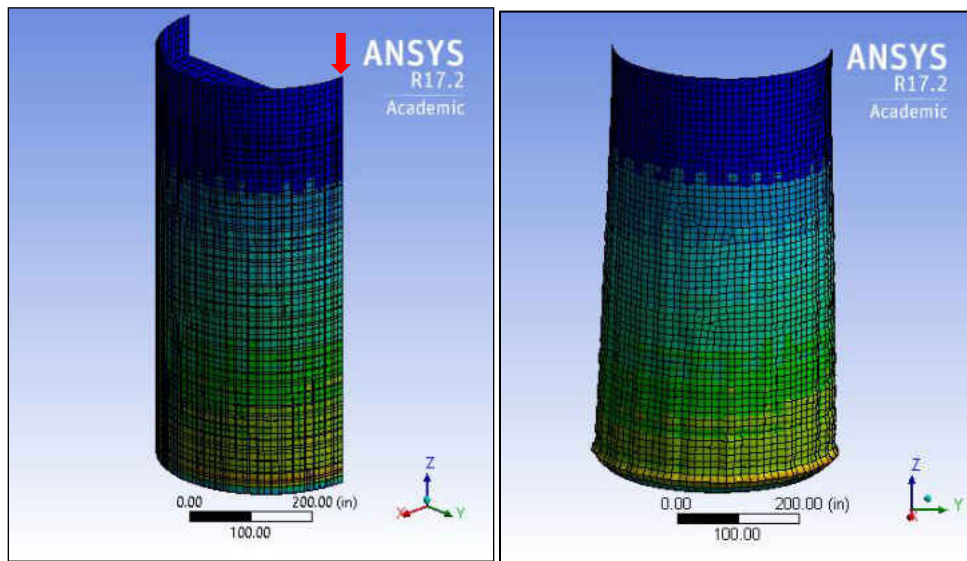


Figure 148. Pseudo equilibrium paths for the critical node of model 11 filled with water to 90% depth



(a) Undeformed shape

(b) Shell deformation

Figure 149. (a) Undeformed shape and (b) Shell deformation of Model 11 filled with water to 90% depth

Model 12

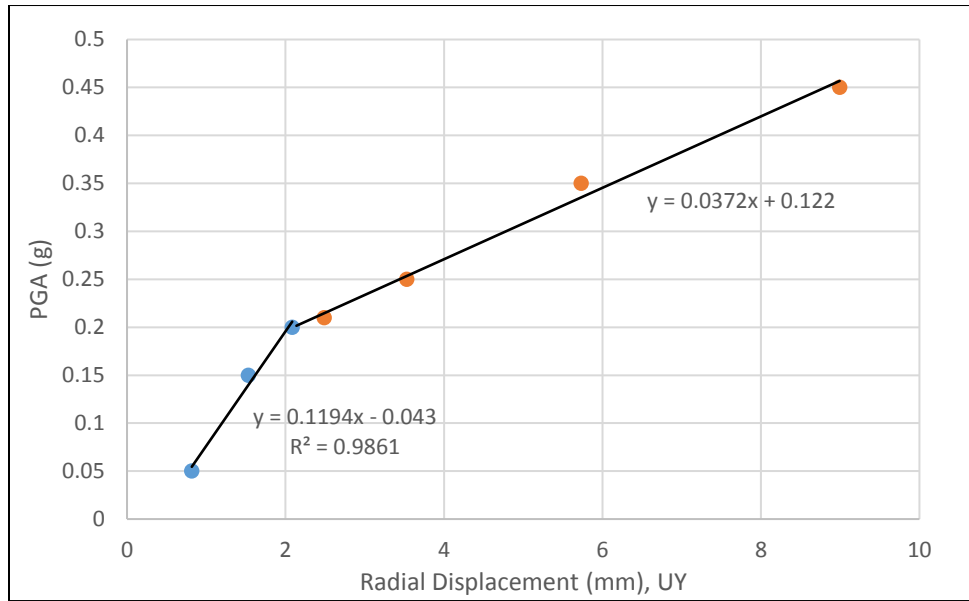
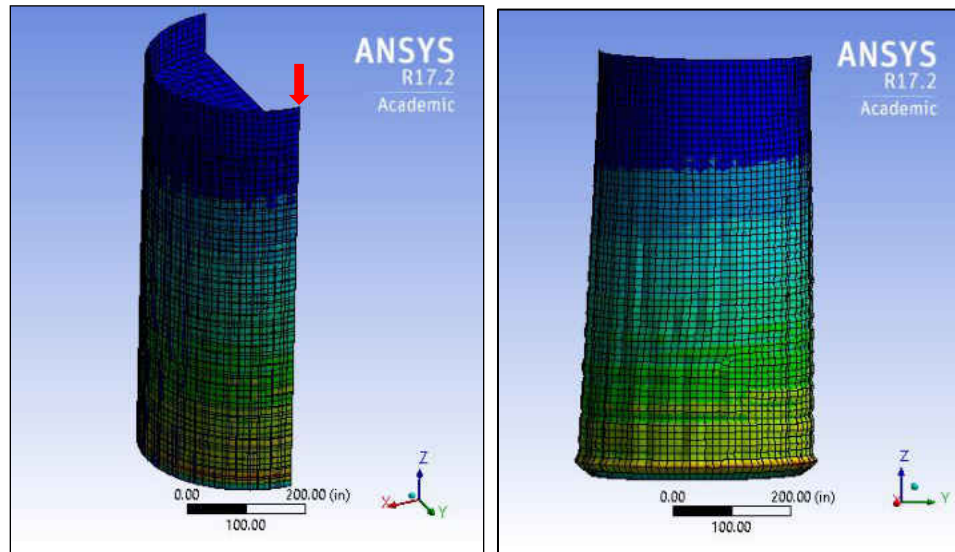


Figure 150. Pseudo equilibrium paths for the critical node of model 12 filled with water to 90% depth



(a) Undeformed shape

(b) Shell deformation

Figure 151. (a) Undeformed shape and (b) Shell deformation of Model 12 filled with water to 90% depth

6.4.5 Comparison of the Buckling Behaviors from El Centro and Parkfield Earthquakes for the Cylindrical Tanks Filled with Water up to 90% of the Heights

The buckling loads in the form of PGA of in terms of gravity acceleration are given in Table 24. These results show that the buckling loads in terms of PGA for the cylindrical tanks are different because of the different characteristics of ground acceleration. The buckling loads for the cylindrical tanks filled with water up to 90% of the heights with $D/t = 1000$ and $D/t = 1500$ subjected to the Parkfield earthquake are higher than the buckling loads when these models are subjected to the El Centro earthquake. However, the buckling loads for the cylindrical tanks with $D/t = 2000$ subjected to the Parkfield earthquake are less than the buckling loads when they are subjected to the El Centro earthquake. Therefore, these results show that, besides the geometries of the cylindrical tanks, the characteristic of the earthquake has a significant influence on the dynamic buckling load.

Table 24. Dynamic buckling loads for the cylindrical tanks filled with water up to 90% of the heights in PGA (g)

H/D	D/t = 1000		D/t = 1500		D/t = 2000	
	El Centro	Parkfield	El Centro	Parkfield	El Centro	Parkfield
0.5	1.20	1.50	1.10	1.20	0.85	0.72
1.0	1.10	1.30	0.95	0.90	0.75	0.35
1.5	0.70	1.05	0.60	0.85	0.30	0.32
2.0	0.60	0.65	0.40	0.45	0.25	0.20

CHAPTER VII

CONCLUSIONS

The purpose of this thesis is to study the static and dynamic buckling of the cylindrical liquid storage tanks using the finite element analysis (FEA). The ANSYS computer program was used to analyze all finite element models in this study. To satisfy the accuracy of FEA models, the theoretical buckling stresses for the pin-pin ended cylindrical shells were verified with the eigenvalue buckling loads from ANSYS computer program. The errors of FEA models to the theoretical buckling stresses range between 2.59% and 9.75%. These errors show that the FEA models are reasonably accurate.

For the static buckling analysis, the lateral loads were applied to the cylindrical tanks to find the eigenvalue buckling loads. These eigenvalue buckling loads were used to approximate the upper limits for the nonlinear buckling analysis. The nonlinear buckling loads, as expected, are less than the eigenvalues buckling loads for all models, and the nonlinear buckling loads range between 86% and 90% of the eigenvalue buckling loads.

For the dynamic buckling analysis, the modal analysis was first performed to find the natural frequencies and mode shapes of the cylindrical tank models. The natural frequencies are important for the dynamic buckling analysis because the natural frequencies are used to find the mass and stiffness coefficients which are the parameters

for determining the damping ratios used in the ANSYS computer program for transient dynamic analysis. In addition, the natural frequencies are used to calculate the stiffness of the structures. The transient analysis was performed to find the buckling loads when the cylindrical tanks are subjected to the earthquake ground accelerations. The models of the cylindrical tanks in this study were subjected to the El Centro and Parkfield earthquakes.

In the cases of empty cylindrical tanks subjected to the horizontal earthquake accelerations, the buckling loads occurred at very high PGA which are unrealistic. The dynamic buckling loads for the empty cylindrical tanks subjected to the El Centro earthquake range between 11g and 42g. The dynamic buckling loads for the empty tanks subjected to the Parkfield earthquake range between 20g and 72g which are higher than the dynamic buckling loads from the El Centro earthquake.

For the cylindrical tanks filled with water up to 90% of their height subjected to the earthquake accelerations, the dynamic buckling loads are significantly smaller than the dynamic buckling loads of the empty cylindrical tanks. The buckling loads of the cylindrical tanks filled with water up to 90% of their height subjected to the El Centro earthquake range between 0.25g and 1.20g, and the buckling loads range between 0.20g and 1.50g when there are subjected to the Parkfield earthquake. The results from the transient analysis show that, for the cylindrical tanks filled with water up to 90% of their height, the dynamic buckling loads decrease when the H/D ratios increase, and the dynamic buckling loads decrease when the D/t ratios increase.

The characteristic of the earthquake has a significant influence on the dynamic buckling load. The dynamic buckling loads for the cylindrical tanks filled with water up to 90% of their height with $D/t = 1000$ and $D/t = 1500$ subjected to the Parkfield

earthquake are higher than the dynamic buckling loads when these cylindrical tanks are subjected to the El Centro earthquake. Nevertheless, the dynamic buckling loads for the cylindrical tanks with $D/t = 2000$ subjected to the Parkfield earthquake are smaller than the buckling loads when they are subjected to the El Centro earthquake.

REFERENCES

- [1] Priestley, M. J. N., Davidson, B. J., Honey, G. D., Hopkins, D. C., Martin, R. J., Ramsey, G., & Wood, J. H. (1986). Seismic design of storage tanks. *Recommendations of a study group of the New Zealand National Society for Earthquake Engineering*, 3.
- [2] Cooper, T. W., & Wachholz, T. P. (1999). Optimizing post-earthquake lifeline system reliability. In *Proceedings of the 5th US conference on lifeline earthquake engineering*. ASCE (Vol. 16, pp. 878-86).
- [3] Eiding, J. (2001). Seismic fragility formulations for water systems. *sponsored by the American Lifelines Alliance, G&E Engineering Systems Inc., web site.* < <http://homepage.mac.com/eiding>.
- [4] Timoshenko, S. (1970). *Theory of Elastic Stability 2e*. Tata McGraw-Hill Education.
- [5] Brazier, L. G. (1927). On the flexure of thin cylindrical shells and other "thin" sections. *Proceedings of the Royal Society of London. Series A, containing papers of a mathematical and physical character*, 116(773), 104-114.
- [6] Housner, G. W. (1963). The dynamic behavior of water tanks. *Bulletin of the seismological society of America*, 53(2), 381-387.
- [7] Veletsos, A. S., & Auyang, J. (1977). Earthquake response of liquid storage tanks. In *Advances in Civil Engineering Through Engineering Mechanics*: (p. 24). ASCE.
- [8] Malhotra, P. K., Wenk, T., & Wieland, M. (2000). Simple procedure for seismic analysis of liquid-storage tanks. *Structural Engineering International*, 10(3), 197-201.
- [9] Sezen, H., Livaoglu, R., & Dogangun, A. (2008). Dynamic analysis and seismic performance evaluation of above-ground liquid-containing tanks. *Engineering Structures*, 30(3), 794-803.
- [10] Eurocode 8. (2000). Earthquake resistant design of structures, part 4: tanks, silos and pipelines, 2nd draft, December.
- [11] Hamdan, F. H. (2000). Seismic behaviour of cylindrical steel liquid storage tanks. *Journal of Constructional steel research*, 53(3), 307-333.
- [12] Nyman, D. J. (1984). Guidelines for the seismic design of oil and gas pipeline systems. *Committee on Gas and Liquid Fuel Lifelines. American Society of Civil Engineers, New York*, 473p.

- [13] Virella, J. C., Godoy, L. A., & Suárez, L. E. (2006). Dynamic buckling of anchored steel tanks subjected to horizontal earthquake excitation. *Journal of Constructional Steel Research*, 62(6), 521-531.
- [14] Jerath, S., and Qiao, W. (2009). “Dynamic Stability of Water Tanks.” Presented at the 2009 Joint ASCE-ASME-SES (American Society of Civil Engineers- American Society of Mechanical Engineers-Society of Engineering Science) Conference on Mechanics and Materials, Blacksburg, USA.
- [15] Jerath, S., & Lee, M. (2015) Stability Analysis of Cylindrical Tanks under Static and Earthquake Loading.
- [16] W. F. Chen and E.M. Lui (1987). Structural Stability theory and implementation. Prentice-Hall, Inc. Upper Saddle River, N.J.
- [17] ANSYS, Inc. (2011). ANSYS Mechanical APDL Element Reference.
- [18] ANSYS, Inc. (2013). ANSYS Mechanical APDL Feature Archive.
- [19] ANSYS, Inc. (2013). ANSYS Mechanical APDL Theory Reference.
- [20] Budiansky B, Roth S. (1962). Axisymmetric dynamic buckling of clamped shallow spherical shells. NASA collected papers on stability of shell structures, TN-1510.p. 597–606.
- [21] Chopra, A. K. (2012). *Dynamics of Structures—Theory and Applications to Earthquake Engineering*. New York: Prentice hall.
- [22] Stevenson, J. D. (1980). Structural damping values as a function of dynamic response stress and deformation levels. *Nuclear engineering and design*, 60(2), 211-237.